Department of Physics and Astronomy

University of Heidelberg

Master thesis

in Physics

submitted by

Elias Bernreuther

born in Bayreuth

2018

Mono-X Signals

from

Final States

This Master thesis has been carried out by Elias Bernreuther

at the

Institute for Theoretical Physics

under the supervision of

Prof. Dr. Tilman Plehn

Mono-X-Signale aus Endzuständen:

Mono-X-Prozesse bieten vielversprechende Signale für Suchen nach dunkler Materie am LHC. In dieser Arbeit untersuchen wir systematisch Mono-X-Signale aus Zerfällen in Endzuständen. Zu diesem Zweck betrachten wir das MSSM und das NMSSM als Modelle für erweiterte Dunkle-Materie-Sektoren. Wir untersuchen Mono-Z-, Mono-W- und Mono-Higgs-Signale mit Fokus darauf, wie die zu erwartenden LHC-Raten durch Produktion und Zerfall schwererer Zustände im dunklen Sektor gesteigert werden können. Im MSSM schränkt die Kombination aus Relic-Density und Limits aus direkter Detektion unsere Erwartungen für Mono-Z-, Mono-W- und Mono-Higgs-Signale am LHC stark ein. Diese Limits werden jedoch größtenteils irrelevant, sobald wir zusätzliche, leichte NMSSM-Mediatoren miteinbeziehen. Darüber hinaus motivieren die Limits aus direkter Detektion Suchen nach Mono-W-Paaren und Mono-Higgs-Paaren, um deren gewöhnliche Mono-X-Gegenstücke zu komplementieren.

Mono-X Signals from Final States:

Mono-X processes provide promising signals for dark matter searches at the LHC. In this thesis, we systematically study mono-X signals from final state decays. To this end, we use the MSSM and NMSSM as models for extended dark matter sectors. We study mono-Z, mono-W, and mono-Higgs signals, focusing on how expected LHC rates are enhanced by the production and decay of heavier states in the dark sector. In the MSSM, the combination of relic density and direct detection constraints strongly limits our LHC expectations for mono-Z, mono-W, and mono-Higgs signals. However, these constraints become largely irrelevant once we include additional, light NMSSM mediators. Furthermore, direct detection limits motivate searches for mono-W pairs and mono-Higgs pairs to complement their usual mono-X counterparts.

Contents

1 Introduction

The search for dark matter is one of the central challenges in fundamental physics today. Since Fritz Zwicky's observations of the Coma Cluster in the 1930s [1], evidence has been accumulating that luminous matter can only account for a small part of the gravitation holding galaxies and galaxy clusters together [2]. The evidence today favors particle dark matter as the solution to this problem [3]. Furthermore, no particle in the Standard Model has the required properties [4]. Hence, dark matter is considered observational evidence for particle physics beyond the Standard Model. However, the exact nature of these particles and the new physics they are embedded in remain elusive. Therefore, the field is driven by a broad program of complementary experiments, covering direct, indirect, and collider searches. At the center of the latter is the LHC, where dark matter could manifest itself as missing transverse energy.

A promising class of dark matter searches at the LHC study mono-X signals [5]. These result from the production of dark matter together with visible particles, which can be jets [6–9], photons [10, 11], W [12–14], Z [15–21], or Higgs bosons [22–25]. These signals are usually motivated by effective field theory arguments. Alternatively, one can classify mono-X processes by topology and, thus, divide them into initial state radiation and final state decays. In the former, dark matter recoils against a visible X that is radiated from initial state quarks or gluons. In the latter, the mono-X signal stems from the decay of heavier states that are produced on-shell.

In this thesis, we study mono-X signals from final state decays using the MSSM and NMSSM as frameworks for WIMP dark matter [26–30]. Supersymmetry is still one of the best-motivated directions for physics beyond the Standard Model and provides a good dark matter candidate in the form of the lightest neutralino [31, 32]. Moreover, the electroweakino sector of the (N)MSSM encompasses singlets, doublets, and triplets under $SU(2)_L$. The mixing between these different representations gives rise to a rich dark matter phenomenology, embedded in a UV-complete model.

This thesis is structured as follows. In Chapter 2, we briefly review the evidence for dark matter, the thermal freeze-out of WIMPs, and the different types of searches for WIMP dark matter. Chapter 3 introduces the MSSM and NMSSM as dark matter frameworks. In Chapter 4, we study mono-Z, mono-W, and mono-Higgs processes from the decay of neutralinos and charginos. We examine how the combination of relic density and direct detection constraints cut into our expectations for these processes at the LHC. Moreover, these limits lead us to consider mono-W-pair and mono-Higgs-pair processes, which rely on the production of pairs of heavier neutralino and chargino states. In Chapter 5, we reconsider mono-Z and mono-Higgs pairs in the NMSSM, making use of the additional scalar and pseudoscalar mediators, which allow us to largely decouple LHC expectations from relic density and direct detection constraints. Finally, in Chapter 6, we present a summary and conclusions.

2 Dark matter

In this chapter, we will begin by briefly summarizing the evidence for dark matter. We will then focus on weakly interacting massive particles (WIMPs) and their freeze-out in the early universe. Finally, we will present an overview of the different ways of searching for WIMP dark matter.

2.1 Evidence for dark matter

Since the first observations pointing towards the existence of dark matter in the 1930s, a great amount of evidence has accumulated across a large range of scales. The aim of the following list is not completeness, but to highlight some of the most important pieces of evidence. A comprehensive overview can be found in Ref. [3, 33].

Rotation curves

Stars in spiral galaxies rotate around the galactic center in approximately circular orbits, where the gravitational attraction is balanced against the centrifugal force, i.e.

$$\frac{v^2}{r} = \frac{GM(r)}{r^2} \Leftrightarrow v = \sqrt{\frac{GM(r)}{r}} \,, \tag{2.1}$$

where $M(r)$ is the total mass within radius r, assuming a spherical system. v denotes the circular velocity. Taking only the luminous matter composed of gas and stars into account, one would therefore expect the velocity to decrease as $v \sim 1/\sqrt{r}$ in the outer region of the galaxy. However, Doppler shift measurements using the 21-cm line of hydrogen instead show rotation velocities that are approximately constant with respect to r far away from the galactic core [34]. This observation can be explained by the existence of a large spherical halo of dark matter around the disk of luminous matter [4].

Galaxy clusters and virial theorem

Similarly, it is possible to infer the existence of dark matter from the dynamics of galaxies within a cluster. In such a system of gravitationally interacting objects the virial theorem takes the form [33]

$$\langle T \rangle = -\frac{\langle U \rangle}{2} \tag{2.2}$$

with $\langle T \rangle$ denoting the average kinetic energy and $\langle U \rangle$ the average potential energy. Using the above relation, it is possible to deduce the mass of a galaxy cluster by measuring the radial velocities of the constituent galaxies. The first measurement of this kind, which was, historically, the first valid measurement pointing towards dark matter, was carried out by Fritz Zwicky in 1933 [1]. By applying the virial theorem to the Coma Cluster he found the total mass to be 160 times larger than what could be accounted for by luminous matter. This value has been revised later, but his conclusion that the majority of the mass in galaxy clusters is provided by non-luminous matter remains valid [35–37].

Merging galaxy clusters

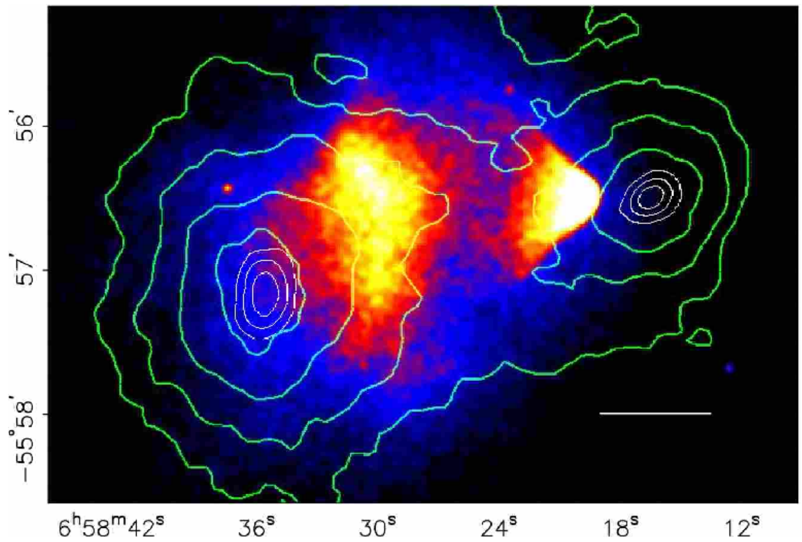

Figure 2.1: Image of the "bullet" cluster 1E0657-558. The colored map is an X-ray image of the merging galaxy clusters. The green contours indicate the mass distribution reconstructed from weak lensing data. Figure from Ref. [38].

Further evidence for dark matter stems from observations of collisions of particular galaxy clusters, with the cluster merger 1E0657-558 involving the so-called bullet cluster as the most prominent example [38]. A central tool that is needed for these and other dark matter related observations is gravitational lensing [39]. Since light moves along geodesics of spacetime, its path is bent by massive objects acting as lenses between source and observer. Hence, it is possible to study the distribution of matter through lensing effects, which are commonly divided into three categories: Microlensing changes only the apparent brightness of an observed object. Weak lensing deflects light by a small angle and, like microlensing, relies on statistical analyses [40]. Finally, strong lensing [41] involves large deflections, which can also lead to multiple images if there is more than one geodesic connecting source and observer. Weak lensing studies in particular have become an important tool to map non-luminous matter [40, 42]. For the bullet cluster, comparing X-ray mappings to gravitational lensing data, as illustrated in Fig. 2.1, shows that the centers of total mass are displaced with respect to the luminous matter distribution. This observation is readily explained assuming dark matter with relatively weak self-interaction [43]. While the gas, which provides most of the luminous matter, is decelerated through electromagnetic interactions, the dark matter moves ballistically. The resulting separation between luminous matter and the centers of gravitation is particularly difficult to reconcile with alternatives to dark matter, like modified-gravity theories [44].

Cosmic microwave background

The cosmic microwave background (CMB) [45, 46] consists of photons emitted at the end of recombination at $T \approx 0.1$ eV, when almost all free electrons had combined with nuclei, making the universe transparent to light. Red-shifted by the expansion of the universe, the CMB photons today form an almost perfect black body spectrum of temperature $T = 2.7$ K, with small anisotropies of order $\frac{\delta T}{T} \sim 10^{-5}$, which have been measured by COBE [47], WMAP [48] and PLANCK [49]. Before recombination, overdensities of dark matter formed gravitational wells pulling in the tightly coupled baryon-photon fluid. The radiation pressure acted against the gravitational pull, causing the baryon-photon fluid to oscillate in the wells. The resulting tower of acoustic oscillation modes appears as peaks in the CMB power spectrum. Dark matter and baryon density affect both the height and the position of these peaks [49]. Fitting the parameters of the ΛCDM model to the power spectrum, one can obtain a measurement of the dark matter relic density. The currently best result is $\Omega_\chi h^2 = 0.1186 \pm 0.002$ [49], where Ω_χ denotes the ratio of the DM density to the critical density [50], and $h = H_0/(100 \text{ km s}^{-1} \text{ Mpc}^{-1})$, with the Hubble parameter H_0.

Structure formation

Collaborations like the Virgo Consortium simulate the formation of structures within the ΛCDM model of cosmology [51]. The large-scale structures predicted by such simulations assuming cold dark matter agree well with observations. In contrast, the observed structures could not have formed in a medium of purely baryonic matter. In particular, density perturbations could only grow in the matter-dominated epoch, which sets on earlier in the presence of dark matter [52]. Hence, the existence of old galaxies provides evidence for dark matter [4].

2.2 Candidates

The observations summarized above provide strong evidence for the existence of dark matter. An alternative consists in modifying the theory of gravity. A classic example for such an approach is Modified Newtonian Dynamics (MOND) [53]. However, it is difficult to embed MOND in a complete, relativistic theory [53]. Furthermore, while modified-gravity explanations can accommodate parts of the evidence for DM, in particular rotation curves, they so far fail to explain the whole range of evidence including, for example, the CMB and structure formation, without introducing any dark matter [54]. Hence, the set of observations as a whole points towards the existence of particle dark matter. Such dark matter particles are required to be electrically neutral, or at least to interact only very weakly with photons. Furthermore, they need to be stable on cosmological time scales. The only Standard Model particles fulfilling these requirements are neutrinos. However, studies of structure formation indicate that most of the dark matter is "cold", i.e. non-relativistic by the time of galaxy formation. The upper bound on the contribution of neutrinos to the relic dark matter abundance is given by [55]

$$\Omega_\nu h^2 \leq 0.0062 \quad 95\% \text{ CL.} \tag{2.3}$$

Therefore, physics beyond the Standard Model (BSM) is necessary to provide a candidate for particle dark matter. An attractive type of candidate are weakly interacting massive particles (WIMPs). Such particles with masses not too far above the weak scale naturally arise e.g. in supersymmetric theories if they attempt to solve the hierarchy problem. We will focus on WIMP dark matter throughout this work. Alternative DM candidates are, among others, axions [56], which were originally proposed to solve the strong CP problem of QCD [57, 58], sterile neutrinos [59], and primordial black holes that formed before nucleosynthesis [60]. However, among these candidates, WIMPs are particularly attractive because they can naturally give rise to the correct dark matter abundance without fine-tuning. This so called "WIMP miracle" will be the subject of the next section.

2.3 Thermal freeze-out

The central measurement with respect to dark matter is its relic abundance $\Omega_\chi h^2$ in the universe today, cf. Sec. 2.1. According to the usual freeze-out paradigm for WIMP dark matter, the value of the relic abundance is determined by DM annihilations in the early universe that freeze out at a certain point in the thermal evolution of the universe.

2.3.1 WIMP miracle

One of the most compelling arguments for WIMP dark matter is the theoretical observation that thermal freeze-out of WIMPs predicts a relic abundance of dark matter close to the observed value. This fact is commonly referred to as the "WIMP miracle". The aim of this section is to highlight the main steps of the WIMP freeze-out calculation and the physics underlying it. Further details can be found in Ref. [52, 61, 50]. The derivation presented here follows Ref. [61, 50].

At early time and high temperature $T \gg m_\chi$, the WIMP is in close contact with the thermal plasma and thus in thermal equilibrium. In the following we assume that equilibrium is maintained through a 2-to-2 process

$$\chi\bar{\chi} \leftrightarrow f\bar{f} \tag{2.4}$$

through which dark matter can annihilate into a pair of SM particles $f\bar{f}$ or be created from them. These SM states are assumed to remain in thermal equilibrium throughout the DM freeze-out. Furthermore, we assume no initial asymmetry between χ and $\bar{\chi}$, i.e. $n_\chi = n_{\bar{\chi}}$. Note that χ and $\bar{\chi}$ may also be the same particle, as is the case for neutralinos, cf. Sec. 3.2. Hence, we will in the following refer to the annihilating DM pair as $\chi\chi$ rather than $\chi\bar{\chi}$.

As the temperature decreases to $T \sim m_\chi$, DM production becomes suppressed, while DM annihilation is reducing the DM number density, which, thus, becomes exponentially Boltzmann-suppressed. Finally, at temperature T_f the reaction rate Γ for the process Eq. (2.4) drops below the Hubble scale, i.e.

$$\Gamma = \sigma_{\chi\chi} v n_\chi \lesssim H, \tag{2.5}$$

and the dark matter freezes out. Here, $\sigma_{\chi\chi}$ denotes the cross section for the annihilation process, Eq. (2.4), and v the DM velocity.

The non-equilibrium evolution of the number density follows the Boltzmann equation

$$\frac{1}{a(t)^3}\,\frac{d}{dt}\left(n(t)a(t)^3\right) = -\langle\sigma_{\chi\chi}\,v\rangle\,\left(n(t)^2 - n_{\text{eq}}(t)^2\right), \tag{2.6}$$

where n_{eq} denotes the equilibrium number density, which for non-relativistic particles reads

$$n_{\text{eq}} = g\left(\frac{mT}{2\pi}\right)^{3/2} e^{-m/T}, \tag{2.7}$$

with g denoting the number of degrees of freedom (d.o.f.) per particle, e.g. $g = 2$ for Majorana fermions. Note that $a^3 n$ is proportional to the number of particles in a comoving volume. The interaction term on the r.h.s. of the Boltzmann equation features the thermally averaged cross section

$$\langle\sigma_{\chi\chi\to ff}\;v\rangle := \frac{\int d^3p_{\chi,1}d^3p_{\chi,2}\;e^{-(E_{\chi,1}+E_{\chi,2})/T}\;\sigma_{\chi\chi\to ff}\;v}{\int d^3p_{\chi,1}d^3p_{\chi,2}\;e^{-(E_{\chi,1}+E_{\chi,2})/T}}\;. \tag{2.8}$$

In the following we need to use the thermodynamic result that

$$g_{\text{eff}}(T)T^3a^3 = const., \tag{2.9}$$

which follows from the conservation of entropy in equilibrium. The effective number of degrees of freedom $g_{\text{eff}}(T)$ is equal to 106.75 if all SM states contribute, and decreases as the heavier SM particles decouple. For the following we will assume that $g_{\text{eff}}(T_f) \approx 100$ and remains constant during DM freeze-out. According to Eq. (2.9) we then have $a \sim T^{-1}$, which we can use in the Boltzmann equation, Eq. (2.6), to obtain

$$T^3 \frac{d}{dt}\left(\frac{n(t)}{T^3}\right) = -\langle \sigma_{\chi\chi}\, v\rangle \; \left(n(t)^2 - n_{\text{eq}}(t)^2\right) . \tag{2.10}$$

Defining $Y \equiv n/T^3$, this takes the form

$$\frac{dY}{dt} = -\langle \sigma_{\chi\chi}\, v\rangle \; T^3 \; \left(Y(t)^2 - Y_{\text{eq}}(t)^2\right) . \tag{2.11}$$

It will be convenient to switch variables to $x = m_\chi/T$, with

$$\frac{dx}{dt} = -\frac{1}{T}\frac{dT}{dt}x = Hx, \tag{2.12}$$

using again $aT = const.$ from Eq. (2.9). Furthermore, in the radiation dominated era,

$$H^2 = \frac{\rho_r}{3M_{\text{Pl}}^2} = \left(\frac{\pi\sqrt{g_{\text{eff}}}}{\sqrt{90}}\frac{T^2}{M_{\text{Pl}}}\right)^2 . \tag{2.13}$$

In particular, this means that $H \sim x^{-2}$, and hence

$$H(x) = \frac{H(x=1)}{x^2}. \tag{2.14}$$

Plugging the above expression into Eq. (2.12) yields

$$\frac{dx}{dt} = \frac{H(x=1)}{x}. \tag{2.15}$$

Combining Eq. (2.15) and Eq. (2.11) gives

$$\frac{dY}{dx} = -\frac{\lambda}{x^2} \; \left(Y(x)^2 - Y_{\text{eq}}(x)^2\right) , \tag{2.16}$$

with the parameter

$$\lambda := \frac{m_\chi^3 \langle \sigma v\rangle(x)}{H(x=1)} = \frac{\sqrt{90}M_{\text{Pl}} m_\chi}{\pi\sqrt{g_{\text{eff}}}} \; \langle \sigma v\rangle(x). \tag{2.17}$$

Here, we will focus on s-wave annihilation, for which the leading term contributing to $\langle \sigma v\rangle(x)$ is independent of v, i.e.

$$\langle \sigma v\rangle(x) \approx \langle \sigma v\rangle_0 \; . \tag{2.18}$$

In this case we can treat λ as constant during the freeze-out process as long as g_{eff} does not change much.

Still, the Boltzmann equation as given in Eq. (2.16) is not analytically solvable. However, we can use the fact that $Y_{\text{eq}}(x) \sim e^{-x}$ and, therefore, $Y_{\text{eq}}(x) \ll Y(x)$ during the freeze-out process, where $x \ll 1$. Then Eq. (2.16) can be approximated as

$$\frac{dY}{dx} = -\frac{\lambda}{x^2}\, Y(x)^2. \tag{2.19}$$

Now, Eq. (2.19 can be solved analytically as long as λ can be treated as constant. To this end, we assume that one can find a reference point $x_\infty > x_f$, where DM has already decoupled, but the number of d.o.f. is still approximately the same, i.e. $g_{\text{eff}}(x_\infty) = g_{\text{eff}}(x_f)$. Then, integration from x_f to x_∞ yields

$$\int\limits_{Y_f}^{Y_\infty} dY\, \frac{1}{Y^2} = \int\limits_{x_f}^{x_\infty} dx\, \left(-\frac{\lambda}{x^2}\right), \tag{2.20}$$

resulting in the condition

$$\frac{1}{Y_f} - \frac{1}{Y_\infty} = -\frac{\lambda}{x_f} + \frac{\lambda}{x_\infty}\,. \tag{2.21}$$

Since Y drops quickly during the non-equilibrium evolution, typically $Y_f \gg Y_\infty$. Further, using $x_\infty \gg x_f$, we find

$$Y_\infty \approx \frac{\lambda}{x_f}, \tag{2.22}$$

which expresses the asymptotic value Y_∞ through λ and the yet undetermined freeze-out temperature parameter x_f.

The value of x_f can be estimated using the freeze-out condition given in Eq. (2.5). Inserting n from Eq. (2.7), H from Eq. (2.13), and $v \approx \sqrt{2T/m_\chi}$ yields

$$e^{-x_f} \approx \frac{\pi^{\frac{5}{2}}}{3\sqrt{10}}\, \frac{\sqrt{g_{\text{eff}}(T_f)}}{m_\chi M_{\text{Pl}} \sigma_{\chi\chi}}. \tag{2.23}$$

For a weak-scale cross section $\sigma_{\chi\chi}$ one finds

$$e^{-x_f} \approx 10^{-12}, \tag{2.24}$$

which translates to

$$x_f \approx 28. \tag{2.25}$$

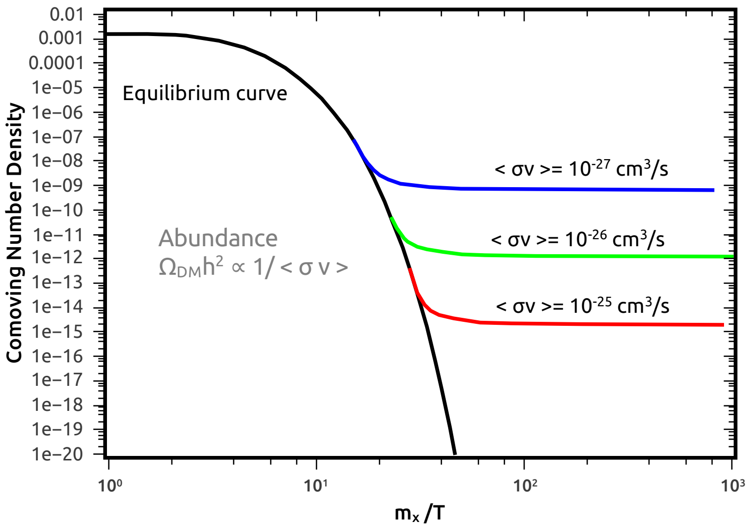

Figure 2.2: Evolution of the comoving DM number density n_χ/s, which is proportional to Y defined in the main text. The onset of freeze-out at $x_f = m_\chi/T_f$ is indicated by the starting points of the colored curves for different annihilation cross sections $\langle\sigma v\rangle$. The asymptotic value of the comoving DM number density is proportional to $\langle\sigma v\rangle^{-1}$. Figure from Ref. [62].

The dependence of x_f on the annihilation cross section is illustrated in Fig. 2.2. After freeze-out, the number of WIMPS is conserved. Therefore, the DM number density $n_\chi(T_0)$ in the universe today is given by

$$n_\chi(T_0) = \frac{a_\infty^3}{a(T_0)^3}\, n_\chi(T_\infty) = \frac{g_{\text{eff}}(T_0)}{g_{\text{eff}}(T_f)}\,\frac{T_0^3}{T_\infty^3}\, n(T_\infty) = \frac{g_{\text{eff}}(T_0)}{g_{\text{eff}}(T_f)}\, T_0^3\, \frac{x_f}{\lambda}, \tag{2.26}$$

where we used Eq. (2.9) in the second step, as well as the assumption that g_{eff} stays constant during freeze-out. In the last step, we plugged in Y_∞ from Eq. (2.22). The effective number of degrees of freedom today is $g_{\text{eff}}(T_0) = 3.91$.

Now, we can translate $n_\chi(T_0)$ into the relic abundance $\Omega_\chi h^2 = \rho_\chi(T_0)/\rho_c(T_0)\; h^2$. Here, $\rho_c(T_0) = 3M_{\text{Pl}}^2 H_0^2$ denotes the critical density. Further, $\rho_\chi(T_0) = m_\chi n_\chi(T_0)$, and $h = H_0/(100 \text{ km s}^{-1} \text{ Mpc}^{-1})$.

Finally, the result for the DM relic abundance reads [3, 61, 50]

$$\begin{aligned}\Omega_\chi h^2 &= \frac{\rho_\chi(T_0)}{3M_{\text{Pl}}^2 H_0^2}\, h^2 = \frac{m_\chi}{3M_{\text{Pl}}^2 H_0^2}\,\frac{g_{\text{eff}}(T_0)}{g_{\text{eff}}(T_f)}\, T_0^3\, x_f\, \frac{\pi\sqrt{g_{\text{eff}}(T_f)}}{\sqrt{90} M_{\text{Pl}} m_\chi}\,\frac{1}{\langle\sigma v\rangle}\, h^2 \\ &\approx 0.12\, \frac{x_f}{28}\, \frac{10}{\sqrt{g_{\text{eff}}(T_f)}}\, \frac{2\cdot 10^{-26}\text{cm}^3/\text{s}}{\langle\sigma v\rangle}\,. \end{aligned} \tag{2.27}$$

This means that a WIMP annihilating with a typical weak-interaction cross section can reproduce the observed DM relic abundance as given in Sec. 2.1. Note that the resulting relic abundance as given in Eq. (2.27) depends on the DM mass only indirectly through the freeze-out parameter x_f and thus only logarithmically. Therefore, the main parameter determining the relic abundance is the annihilation cross section. Hence, we find to good approximation $\Omega_\chi h^2 \propto \langle \sigma v \rangle^{-1}$, as illustrated in Fig. 2.2. Further, note that for the inverse dependence of the DM abundance on $\sqrt{g_{\text{eff}}}$ it is crucial that g_{eff} is roughly constant during freeze-out. This is not necessarily the case if additional degrees of freedom contributing to g_{eff} are co-annihilating with dark matter, as described in Sec. 2.3.2.

In the derivation above, we assumed the annihilation cross section to be independent of the DM velocity v, cf. Eq. (2.18). More generally, $\langle \sigma_{\chi\chi} v \rangle$ can be expanded in powers of v as

$$\langle \sigma_{\chi\chi} v \rangle = \langle s_0 + s_1 v^2 + \mathcal{O}(v^4) \rangle \ . \tag{2.28}$$

Using terminology from partial wave analysis, so-called s-wave annihilation contributes to both s_0 and s_1. For p-wave annihilation, s_0 vanishes. Hence, in this case, the leading term in σv is velocity suppressed by v^2. Since $v^2 \sim T \sim x^{-1}$, the parameter λ, defined in Eq. (2.17), thus gains an additional dependence on x if DM annihilates through a p-wave. In this case, one can define $\lambda_0 = \lambda x$, which is again constant. Then, Eq. (2.19) can be written as

$$\frac{dY}{dx} = -\frac{\lambda_0}{x^{2+1}}\, Y(x)^2 \ , \tag{2.29}$$

which may be solved analogously to the derivation for s-wave processes shown above. Furthermore, whether DM in a particular model annihilates through s-wave or p-wave processes depends on the type of DM particle and mediator. A general overview is given in Tab. 2.1. Since the average DM velocity depends on temperature, a possible velocity suppression is particularly relevant when comparing DM annihilation at different times in the history of the universe.

	s-channel mediator				t-channel mediator			
	$\bar{f}f$	$\bar{f}\gamma^5 f$	$\bar{f}\gamma^\mu f$	$\bar{f}\gamma^\mu\gamma^5 f$	$\bar{f}f$	$\bar{f}\gamma^5 f$	$\bar{f}\gamma^\mu f$	$\bar{f}\gamma^\mu\gamma^5 f$
Dirac fermion	v^2	v^0	v^0	v^0	v^0	v^0	v^0	v^0
Majorana fermion	v^2	v^0	0	v^0	v^0	v^0	v^0	v^0
real/complex scalar	v^0	v^0	$0/v^2$	$0/v^2$				

Table 2.1: Velocity suppression of the leading term in σv for different types of DM and couplings to the mediator. Table from Ref. [61].

2.3.2 Co-annihilation

Furthermore, the simple picture with a single annihilation process, as shown in Eq. (2.4) can be modified in models with an extended dark sector containing more than one particle. For example, if, in addition to χ_1, a heavier state χ_2 exists, annihilation can proceed through the processes

$$\chi_1\chi_1 \to f\bar{f}\ , \qquad \chi_1\chi_2 \to f\bar{f}\ , \qquad \chi_2\chi_2 \to f\bar{f}\ . \tag{2.30}$$

The prerequisite for co-annihilation is that χ_2 is not too much heavier than χ_1. Following Eq. (2.7), the ratio of equilibrium number densities reads

$$\frac{n_{2,\text{eq}}}{n_{1,\text{eq}}} = \frac{g_2}{g_1}\left(1+\frac{\Delta m_\chi}{m_{\chi_1}}\right)^{3/2} e^{-\Delta m/T} \tag{2.31}$$

Hence, for co-annihilation to be relevant, $\Delta m_\chi = m_2 - m_1$ should not be larger than m_1 by more than about 10% [61]. Otherwise, the state χ_2 is already too rare by the time χ_1 freezes out. If the first two processes in Eq. (2.30) dominate, the Boltzmann equation for n_1 takes the form [61]

$$\begin{aligned}\dot{n}_1(t) + 3H(t)n_1(t) =& - \langle\sigma_{\chi_1\chi_1}v\rangle\ \left(n_1(t)^2 - n_{1,\text{eq}}(t)^2\right)\\ &- \langle\sigma_{\chi_1\chi_2}v\rangle\ \left(n_1(t)n_2(t) - n_{1,\text{eq}}(t)n_{2,\text{eq}}(t)\right)\\ \approx& - \langle\sigma_{\chi_1\chi_1}v\rangle\ \left(n_1(t)^2 - n_{1,\text{eq}}(t)^2\right)\\ &- \langle\sigma_{\chi_1\chi_2}v\rangle\ \left(n_1^2(t) - n_{1,\text{eq}}(t)^2\right)\ \frac{n_{2,\text{eq}}}{n_{1,\text{eq}}}\end{aligned} \tag{2.32}$$

Inserting Eq. (2.31), this reads

$$\begin{aligned}&\dot{n}_1(t) + 3H(t)n_1(t)\\ &= -\left[\langle\sigma_{\chi_1\chi_1}v\rangle + \langle\sigma_{\chi_1\chi_2}v\rangle\ \frac{g_2}{g_1}\ \left(1+\frac{\Delta m_\chi}{m_{\chi_1}}\right)^{3/2}\ e^{-\Delta m_\chi/T}\right]\left(n_1(t)^2 - n_{1,\text{eq}}(t)^2\right)\ .\end{aligned} \tag{2.33}$$

Thus, the solution to Eq. (2.33) can be related to the results from Sec. (2.3.1) by the substitution

$$\langle\sigma_{\chi\chi}\,v\rangle \to \langle\sigma_{\chi_1\chi_1}v\rangle + \langle\sigma_{\chi_1\chi_2}v\rangle\ \frac{g_2}{g_1}\ \left(1+\frac{\Delta m_\chi}{m_{\chi_1}}\right)^{3/2}\ e^{-\Delta m_\chi/T}\ . \tag{2.34}$$

Finally, it should be noted that many alternative mechanisms that can lead to the observed DM abundance have been proposed. Scenarios of this kind are, for example, freeze-in [63] and asymmetric dark matter [64]. However, we will consider WIMPs with standard freeze-out throughout.

2.4 Dark matter searches

While we can infer the existence of dark matter from its gravitational effects, as of now, we have not observed dark matter in a detector or seen it interact non-gravitationally in the universe today. However, among others, the freeze-out mechanism presented in the last section motivates the assumption that dark matter also interacts non-gravitationally with Standard Model particles. If such interactions between WIMP DM and SM particles exist, they can be exploited in three different ways for the three main types of WIMP dark matter searches: direct detection, indirect detection, and collider searches. In this section, we will summarize the principles of these searches, focusing on direct detection and LHC searches.

2.4.1 Direct detection

DM direct detection (DD) experiments aim to directly measure the interaction of DM with ordinary matter, typically in the form of elastic scattering of DM on nuclei [65]. WIMP masses of $m_\chi \approx 10$ GeV to 10 TeV thereby result in typical nuclear recoil energies of $E \approx 1$ keV to 100 keV [66]. The recoil energy is maximal if the mass of the nucleus m_A approximately matches the DM mass [61]. The following overview of the physics of direct detection mostly follows Ref. [66].

The interaction rate for DM-nucleus scattering is determined by the DM flux and the scattering cross section. The differential recoil spectrum reads [67]

$$\frac{dR}{dE}(E,t) = \frac{\rho_0}{m_\chi m_A} \int v \, f(\mathbf{v},t) \, \frac{d\sigma}{dE}(E,v) \, d^3v, \tag{2.35}$$

where $\rho_0 \approx 0.3 \text{ GeV/cm}^3$ denotes the local DM density, $\frac{d\sigma}{dE}$ the differential scattering cross section, and $f(\mathbf{v},t)$ the DM velocity distribution shifted from the galactic rest frame to the Earth's rest frame. In the galactic rest frame, $f(\mathrm{v})$ can be described by an isotropic Maxwell distribution, i.e. [66]

$$f(\mathbf{v}) = \frac{1}{\sqrt{2\pi\sigma}} \, \exp\left(-\frac{|\mathbf{v}|^2}{2\sigma_v^2}\right), \tag{2.36}$$

which is cut off at the galactic escape velocity $v_{\text{esc}} \approx 544$ km/s [66]. The standard deviation is given by $\sigma_v = \sqrt{3/2}v_c$, with $v_c \approx 220$km/s denoting the local circular velocity. Hence, DM moves through our galaxy with velocities similar to the rotational velocities of stars. The Earth's revolution around the sun is responsible for the time-dependence of the shifted distribution $f(\mathbf{v},t)$. Thus, a possible DM signal is expected to show an annual modulation of the form [66]

$$\frac{dR}{dE}(E,t) \approx S_0(E) + S_m(E) \, \cos\left(\frac{2\pi\,(t-t_0)}{T}\right) \tag{2.37}$$

where T is the rotation period of the Earth around the sun and $t_0 \approx 150$ d the time at which the WIMP velocity with respect to the Earth's rest frame is maximal. This expected modulation is one feature that distinguishes a potential DM signal from background.

For DM-nucleon scattering one commonly distinguishes between spin-independent and spin-dependent interactions, the latter of which are sensitive to the nuclear spin content. The differential cross section in Eq. (2.35) can be written as the sum [66]

$$\frac{d\sigma}{dE} = \frac{m_A}{2\mu_A^2 v^2} \left(\sigma_0^{\mathrm{SI}} \, F_{\mathrm{SI}}^2(E) \; + \; \sigma_0^{\mathrm{SD}} \, F_{\mathrm{SD}}^2(E)\right), \tag{2.38}$$

with the reduced mass μ_A of the DM-nucleus system. Here, σ_0^{SI} and σ_0^{SD} are the spin-independent and the spin-dependent cross sections at zero momentum transfer. These are both weighted by a nuclear form factor, denoted by F_{SI} and F_{SD}, respectively.

Since spin-independent interactions add up coherently over all protons and neutrons in the nucleus, the spin-independent cross section for a nucleus with mass number A and atomic number Z reads [66]

$$\sigma_0^{\mathrm{SI}} = \sigma_p \, \frac{\mu_A^2}{\mu_p^2} \, \left[Z \, f^p \; + \; (A - Z) \, f^n\right]^2, \tag{2.39}$$

where μ_p stands for the reduced WIMP-nucleon mass, and f^p and f^n denote the coupling strengths to the proton and neutron, respectively. If isospin is conserved, i.e. $f^p = f^n$, Eq. (2.39) takes the form

$$\sigma_0^{\mathrm{SI}} = \sigma_p \, \frac{\mu_A^2}{\mu_p^2} \, A^2 \, \left[f^p + f^n\right]^2, \tag{2.40}$$

which includes an enhancement by the square of the mass number A^2. Hence, to detect spin-independent interactions, heavy nuclei, like Xenon, are preferred.

The spin-dependent cross section, on the other hand, depends on the nucleon spins and can be expressed as [66]

$$\sigma_0^{\mathrm{SD}} = \frac{32}{\pi} \mu_A^2 \, G_F^2 \, \left[a_p \, \langle S^p \rangle \; + \; a_n \, \langle S^n \rangle\right]^2 \, \frac{J+1}{J}, \tag{2.41}$$

with Fermi's constant G_F, the total nuclear spin J, and the effective proton (neutron) couplings $a_{p,n}$. Further, $\langle S^{p,n} \rangle$ denote the spin expectation values from protons and neutrons, respectively. In contrast to the spin-independent case, the spin-dependent interactions with nucleons are not summed coherently. Therefore, there is no significant enhancement of the cross section with the mass of the nucleus.

Instead of distinguishing only spin-independent and spin-dependent interactions, one can also describe the interactions between DM and the nucleus in the framework of a non-relativistic effective field theory [68].

Overall, the recoil spectrum from Eq. (2.35) assumes an approximately exponential form [67], i.e.

$$\frac{dR}{dE}(E) \approx \left(\frac{dR}{dE}\right)_0 \, F^2(E) \, \exp\left(-\frac{E}{E_c}\right), \tag{2.42}$$

with a characteristic energy scale E_c. Hence, the spectrum is dominated by events with low recoil energies. In general, for a fixed energy threshold of the detector, the lower the DM mass, the smaller is the part of the recoil spectrum that the detector is sensitive to. Due to the exponential form of Eq. (2.42), this means that for low DM masses detectors are typically only sensitive to a very small fraction of the spectrum, underlining the need for low-threshold detectors.

Typical rates expected for example for a MSSM neutralino are in the range below 1 event $d^{-1}kg^{-1}$ [4], which lies far below the typical radioactive background. It is therefore essential to use extremely radio-pure materials in the experiment and to shield it well from cosmic rays.

So far, there has been no convincing DM signal from direct detection experiments. Only the DAMA collaboration has reported a supposed signal, which is claimed to be consistent with a WIMP of either $m_\chi \approx 50$ GeV and $\sigma_{\chi p} \approx 7 \cdot 10^{-6}$ pb, or $m_\chi \approx$ 6-16 GeV and $\sigma_{\chi p} \approx 2 \cdot 10^{-4}$ pb. However, these options are strongly excluded by other experiments [69, 70].

In absence of a signal, the different direct detection experiments are currently setting limits on the DM-nucleon interaction cross section. At present, the strongest limits for DM with masses $\gtrsim 6$ GeV stem from liquid noble gas detectors, with Xenon or Argon as target elements. This type of detector is, for example, employed by the XENON [69], PandaX [70] and LUX [71] collaborations. These three experiments are all Xenon-based. Furthermore, they are dual phase detectors containing both a liquid and a gaseous phase. This detector design brings the advantage that two scintillation signals S1 and S2 can be measured for each event. The primary scintillation S1 is induced directly by the scattering event, whereas the second, later scintillation S2 originates from ionization electrons that drift from the liquid into the gas and are amplified there. The time delay between S1 and S2 makes it possible to determine the position of the scattering event in the z-direction. Moreover, by comparing S1 and S2 one can distinguish between nuclear and electronic recoils.

Fig. 2.3 shows current limits from XENON1T, which at the moment provides the strongest limits on the spin-independent DM-nucleon cross section for DM masses above 6 GeV, with a minimum of $4.1 \cdot 10^{-47}$ cm^2 at $m_\chi = 30$ GeV [69]. Towards lower masses the limits quickly become much weaker due to the energy threshold of the detector, in combination with the exponential form of the recoil spectrum as given in Eq. (2.42). The weakening of the limits towards larger masses, on the other hand, is due to the fact that for higher masses the local DM mass density ρ_0 corresponds to a lower DM number density and, thus, lower scattering rates, cf. Eq. (2.35). The local abundance of a given DM constituent is also reduced if it comprises only part of the dark matter and hence does not account for the full relic density. Therefore, in this case, weaker, rescaled DD limits have to be applied.

In the case of spin-dependent DM-nucleon scattering, one needs to distinguish between DM-proton and DM-neutron scattering. The currently strongest limits on the spin-dependent DM-neutron cross section result from the full exposure of the LUX experiment [71]. The best DM-proton scattering limits, on the other hand, stem from the PICO-60 experiment [72], which employs a bubble chamber filled

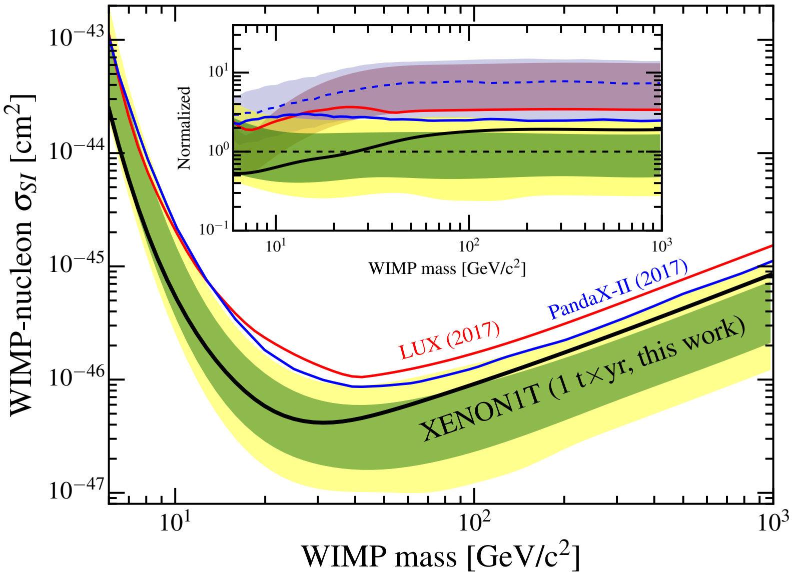

Figure 2.3: 90% confidence level upper limit on the spin-independent cross section σ_{SI} from the XENON1T experiment with 1 t×yr exposure. From Ref. [69].

with C_3F_8.

Upcoming noble gas detectors, like XENONnT [73], LZ [74] and DARWIN [75], will yield sensitivity improvements of up to two orders of magnitude compared to the current capabilities of XENON1T. Thus, DARWIN is expected to eventually become sensitive to the large, irreducible background from neutrino scattering [75]. This background is commonly referred to as the neutrino floor, since it constitutes a limit on the sensitivity attainable with the current approach to DM direct detection, which relies on very low background.

In addition to the ones mentioned above, several other detector designs and approaches are being pursued. One example are solid state detectors, which are particularly sensitive to light DM in the GeV range, due to their lower energy threshold compared to noble gas detectors. Different approaches include for example exploiting ionization electrons from nuclear recoils to measure low-energy nuclear recoils that are otherwise undetectable [76].

Overall, direct detection experiments aim to conclusively test the WIMP freeze-out scenario over the next years.

2.4.2 Indirect detection

Another approach is to detect dark matter indirectly through its annihilation products, which can complement direct searches, in particular for large DM mass and coupling scenarios that direct detection is not sensitive to. In regions of high DM density, e.g at the centers of galaxies, dark matter may still be annihilating today at a sizable rate into particle-antiparticle pairs or photons. Possible annihilation channels are, for example [61]

$$\begin{aligned}
&\chi\chi \to l^+ l^- \\
&\chi\chi \to q\bar{q} \to p\bar{p} + X \\
&\chi\chi \to \tau^+\tau-,\, W^+W^-,\, b\bar{b} + X \to l^+l^-,\, p\bar{p} + X \qquad ... \\
&\chi\chi \to \gamma\gamma\,,
\end{aligned} \tag{2.43}$$

where the last annihilation into a pair of photons is only possible at loop level. Particle-antiparticle pairs are usually searched for through antiparticles, since the background of e.g. positrons from other astrophysical sources is much lower than for electrons. Depending on whether the measured annihilation products are directly pair-produced or radiated off other final state particles, the signal either takes the form of a monoenergetic line or of a continuous spectrum with a cutoff [61], i.e.

$$E_{e^+,\gamma} = m_\chi \qquad \text{or} \qquad E_{e^+,\gamma} < m_\chi\,. \tag{2.44}$$

In terms of the discrete or continuous annihilation spectrum $\frac{dN_{e^+,\gamma}}{dE_{e^+,\gamma}}$, the flux of positrons or photons measured by an observer over the solid angle $\Delta\Omega$ and along a particular line of sight is given by [61]

$$\frac{d\Phi_{e^+,\gamma}}{dE_{e^+,\gamma}} = \frac{\langle\sigma v\rangle}{8\pi m_\chi^2}\,\frac{dN_{e^+,\gamma}}{dE_{e^+,\gamma}}\int_{\Delta\Omega} d\Omega \int_{\text{line of sight}} dz\;\rho_\chi^2(z). \tag{2.45}$$

As can be observed from Eq. 2.45, the DM density profile ρ_χ represents a key input for indirect detection, which can however not be measured directly. Instead, one needs to rely on simulation results, which are usually parameterized as NFW, Einasto or Burkert profiles.

Examples for indirect detection experiments are the Fermi-LAT collaboration [77] studying photon signals, and AMS02 [78], which investigates the antimatter flux.

2.4.3 Dark matter searches at the LHC

A third way of detecting dark matter lies in its production at colliders, which provide a controlled environment with many collisions where the kinematics and backgrounds are better understood than in direct or indirect detection experiments. The sizable interactions with Standard Model particles that are needed for thermal freeze-out should allow for the production of WIMPs at the LHC, at least if they interact with quarks or gluons. However, dark matter itself does not interact with the detector. Therefore, collider searches need to rely on detecting visible particles produced in association with dark matter, while the DM particles carry away part of the energy. At a hadron collider the longitudinal momentum of the partons entering any particular collision is not known. Instead, the probability that a parton enters the hard process carrying a fraction $x = 0..1$ of the proton momentum is parametrized by parton distribution functions $f_i(x)$, with $i = u, d, c, s, g$, such that cross sections take the form

$$\sigma = \int_0^1 dx_1 \int_0^1 dx_2 \sum_{ij} f_i(x_1)\, f_j(x_2)\, \hat{\sigma}_{ij}(x_1 x_2 s) \,, \tag{2.46}$$

where i, j denote the incoming partons and x_1, x_2 the momentum fractions they carry. However, the transverse momenta add to zero. At the LHC dark matter hence manifests itself as missing transverse energy $E_{T,\text{miss}}$, which has to be reconstructed from the visible particles that the DM recoils against. These can be jets, leptons, photons, W, Z or Higgs bosons. Processes where dark matter is produced in association with one such visible object X, i.e.

$$pp \to \chi\bar{\chi} \ + \ X \,, \tag{2.47}$$

are referred to as mono-X processes [5]. The resulting signature is $X \ + \ E_{T,\text{miss}}$.

Experimental signals

A broad program of experimental dark matter searches is carried out by ATLAS and CMS. As of yet, none of these have yielded a significant excess over the expected background. In the following we briefly summarize the different types of mono-X and related signals. This overview follows Ref. [79].

Mono-jet: Mono-jet (jet + $E_{T,\text{miss}}$) [6–9, 80, 81] strictly speaking refers to the production of DM in association with exactly one high-p_T QCD jet. However, in practice, events with multiple jets are typically also included. The leading backgrounds are $Z(\to \nu\bar{\nu})$ + jets, $W(\to l\nu)$ + jets where the lepton is lost, and jet mismeasurements faking $E_{T,\text{miss}}$. Mono-jet processes usually come with the largest rates of all mono-X processes, due to the large QCD coupling involved.

Mono-photon: Mono-photon ($\gamma + E_{T,\text{miss}}$) [10, 11, 82, 83] signals are typically associated with lower rates than mono-jet. However, mono-photon signals profit from their very clean final state with one high-p_T photon. The background for this signal is very low and typically stems from detector effects, e.g. electron or jet misidentification, and beam induced events [79].

Mono-Z: Leptonically decaying mono-Z ($Z(\to ll) + E_{T,\text{miss}}$) [15–20, 84, 85] provides another clean signal, for which background can be effectively suppressed by requiring the p_T of the leptons to be opposite in azimuthal direction and to be similar in magnitude to $E_{T,\text{miss}}$. Further, the invariant mass of the leptons is required to be similar to m_Z. The dominant, irreducible backgrounds stem from di-boson production, particularly $Z(\to \nu\nu)Z$. Apart from that, hadronically decaying Z bosons [21, 86] can contribute to the mono-jet rate, if the transverse momentum of the Z is sufficiently high. This is the case if $m_Z/(2p_{T,Z}) \lesssim R$, where R denotes the distance parameter of the jet-clustering algorithm.

Mono-W: Mono-W [12–14, 87, 88] gives rise to a mono-lepton signal. Since an identical signal is produced in the decay of an off-shell W, background suppression is more difficult than for the mono-Z signal. Nonetheless, mono-W may be an attractive channel as it is sensitive to differences between the couplings of DM to up- and down-type quarks [89]. However, some set-ups used in studies to argue that mono-W rates can be large have been found to violate gauge-invariance [90].

Mono-Higgs: Mono-Higgs [22–25] processes where the Higgs decays into photons $(h(\to \gamma\gamma) + E_{T,\text{miss}})$ [91, 92] profit from low background and good invariant-mass resolution for the photon pair. For the decay $h \to b\bar{b}$ [93, 94], on the other hand, rejecting the large backgrounds from $t\bar{t}$ and Z/W + jets is of great importance. Like for mono-Z and mono-W, the hadronic decay can result in a single fat jet if $m_h/(2p_{T,Z}) \lesssim R$.

DM + tops: In addition to mono-X signatures, it can be attractive to search for dark matter in the channel $t\bar{t} + E_{T,\text{miss}}$, if DM couples most strongly to heavy flavors [95–97]. The strongest limits for this process stem from the semi-leptonic channel where one of the W bosons from the decay $t \to bW$ decays hadronically while the other decays into leptons. Furthermore, DM production together with a single top quark has been considered [98–101]. Such a signal must rely on flavor-changing transitions or b quarks from the initial state.

Invisible Higgs decays: If dark matter couples to the Higgs boson and is lighter than half the Higgs mass, i.e. $m_\chi < m_h/2$, the decay $h \to \chi\chi$ contributes to the invisible branching ratio of the Higgs boson. Both ATLAS and CMS are searching for invisible Higgs decays [102–104]. The most sensitive channel, yielding the strongest bound of $\text{BR}_{h\to\text{inv}} < 24\%$ [105], is vector boson fusion (VBF), in which a Higgs boson is produced in association with two jets with large $\Delta\eta_{jj}$ and large invariant mass m_{jj} [106]. Other, less sensitive channels are associated Vh production and gluon fusion with a jet from initial state radiation. Note that Vh production followed by an invisible V decay is also a contribution to mono-V.

EFTs and simplified models

On the theory side, a number of different approaches to making predictions for mono-X processes are being pursued. On the one hand, dark matter eventually needs to be part of a consistent, UV-complete theory. On the other hand, too strong model assumptions may mean missing important signals. For that reason, DM signatures are being studied within frameworks that range from the generality of effective field theories (EFT) to the completeness of full models like the (N)MSSM. Furthermore, simplified models attempt to strike a balance between these two approaches. The structure of the summary presented here follows Ref. [79].

EFTs constitute the most minimal and agnostic approach to dark matter at the LHC [107, 108]. The underlying assumption is that the DM particle is the only kinematically accessible new state at the LHC, while other new particles are heavy enough to always be far below their mass shell. Integrating out these heavy states gives rise to effective operators with mass dimension greater than four, linking DM to SM fields. These operators are suppressed by powers of a suppression scale Λ, with $1/\Lambda^{n-4}$ being the suppression factor for an operator of mass dimension n. For example, interactions via a heavy mediator V with axial-vector coupling to both DM and quarks are captured by an operator that reads [79]

$$\frac{1}{\Lambda^2}\left(\bar{q}\gamma^{\mu}\gamma_5 q\right)\left(\bar{\chi}\gamma_{\mu}\gamma_5\chi\right) \ . \tag{2.48}$$

Here, Λ denotes a suppression scale, which in this case can be identified as

$$\Lambda = \frac{m_V}{\sqrt{g_q g_\chi}} \ , \tag{2.49}$$

where g_q is the coupling of the mediator to quarks, g_χ the coupling to DM, and m_V and denotes the mediator mass. In an analogous fashion, one can write down effective operators that represent interactions between DM and SM Higgs or gauge bosons.

However, despite its generality, DM EFT is limited in its scope of application [109, 110]. An obvious limitation is that other particles like mediators or additional dark-sector states, may only be integrated out if their masses lie sufficiently far above the typical center of mass energy in processes at the LHC. In the example of the axial-vector mediator above, this requires m_V to be at least in the TeV range, suppressing the operator Eq. (2.48). On the other hand, sizable cross sections are typically only obtained if $\Lambda < 1$ TeV [79]. As can be observed from Eq. (2.49), this requirement can only be reconciled with a significantly larger mass m_V if the couplings g_q, g_χ are large. However, this scenario can lead to unitarity violation [111]. Within the EFT, this can be seen considering the fact that cross sections scale as s/Λ^4. Hence, at large center of mass energies $\sqrt{s}$, the cross section can violate unitarity, even if $\sqrt{s} \ll m_V$. This has been found to typically be the case for $\sqrt{s} > (2..3)\Lambda$ [79]. Moreover, for DM and mediator masses, for which an EFT description is viable and does not make unphysical predictions, it is challenging to obtain the correct relic density while still predicting appreciable LHC rates [109]. Again, this is the case because the relic abundance scales as $\langle\sigma v\rangle^{-1} \sim m_{\text{med}}^4/(m_\chi^2 g_q^2 g_\chi^2)$, where m_{med} needs to be large while g_q, g_χ must not be too large. Otherwise an EFT description is not possible. Finally, it is known that EFTs can predict incorrect shapes for kinematic distribution [109]. For instance, p_T-spectra obtained within an EFT description of DM are typically too hard.

A central shortcoming of the EFT framework is that it precludes light mediators. Simplified models attempt to remedy this problem without introducing too much model dependence [112–114]. In contrast to the EFT, a simplified model explicitly includes a mediator, which couples to both DM and SM quarks or gluons. Depending on the interaction structure, the simplified model can allow production of DM at the LHC either through s-channel or, if the mediator carries color charge, through t-channel processes. In the case of an s-channel mediator, the parameters in the simplified model Lagrangian are the DM mass m_χ, the mediator mass m_{med}, the coupling of the mediator to quarks g_q, and the coupling of the mediator to DM g_χ. Scalar, pseudoscalar, vector, and axial-vector mediators have been considered. The interaction part of the Lagrangian for an s-channel scalar mediator ϕ reads [79]

$$\mathcal{L} \supset g_q\, \phi \sum_q \frac{y_q}{\sqrt{2}} \bar{q} q \;+\; g_\chi\, \phi \bar{\chi} \chi\, . \tag{2.50}$$

Analogously, for a pseudoscalar a we have [79]

$$\mathcal{L} \supset g_q\, a \sum_q \frac{y_q}{\sqrt{2}} \bar{q} \gamma_5 q \;+\; g_\chi\, a \bar{\chi} \gamma_5 \chi\, . \tag{2.51}$$

For a vector mediator V it takes the form [79]

$$\mathcal{L} \supset g_q\, V_\mu \sum_q \bar{q} \gamma^\mu q \;+\; g_\chi\, V_\mu \bar{\chi} \gamma^\mu \chi\, , \tag{2.52}$$

and finally for an axial-vector V the form [79]

$$\mathcal{L} \supset g_q\, V_\mu \sum_q \bar{q} \gamma^\mu \gamma_5 q \;+\; g_\chi\, V_\mu \bar{\chi} \gamma^\mu \gamma_5 \chi\, . \tag{2.53}$$

For the (axial)vector model, minimal flavor violation is implemented by requiring the mediator-quark couplings to be identical for all quarks [112]. For the (pseudo)scalar, minimal flavor violation requires the couplings to be proportional to the respective Yukawas y_q [112].

The only additional parameter needed to define the simplified model is the mediator width Γ_{med}. However, simplified model studies often make the assumption that the mediator can only decay to DM, quarks, or gluons, as specified in the simplified model Lagrangian [79], i.e.

$$\Gamma_{\mathrm{med}} = \Gamma_{\chi\bar{\chi}} \;+\; \sum_q \Gamma_{q\bar{q}} \;+\; \Gamma_{gg}\, . \tag{2.54}$$

Further, it is commonly assumed that kinematic spectra and other results have only a trivial dependence on the couplings g_q and g_χ, such that these may be fixed to constant values. The most common choice is $g_q = 0.25$ and $g_\chi = 1$ [79]. Thus, the only free parameters left in the simplified model are the masses m_χ and m_{med}. Correspondingly, constraints are usually depicted in the plane spanned by m_χ and m_{med}.

While simplified models are useful to translate experimental limits into mass and coupling constraints and to guide LHC searches, they are not complete models that well-defined at the quantum-level. Like for EFT approaches, issues of unitarity and gauge invariance have been shown to also arise in simplified models, in particular again in the context of mono-W signals [14, 115]. Moreover, simplified models are often not anomaly-free, for example if a new mediator couples to quarks, but not to leptons. The hope is that, despite not being realistic models, simplified models still capture the relevant phenomenology correctly. However, it is not clear that that is always the case. For instance, unitarity, gauge invariance, and freedom from anomalies typically require the existence of additional particles in the dark sector, which may contribute to processes at the LHC [116, 117]. The presence of these other states may affect phenomenological predictions. Furthermore, simplified models fail to account for relations between the masses and couplings that may arise from a complete theory.

One way to remedy these problems is to study dark matter as part of a UV-complete model [118–124]. One interesting possibility are Two-Higgs-Doublet Models (2HDM) [116, 117]. These contain two Higgs doublets, whose components after electroweak symmetry breaking mix to form the SM Higgs, another neutral scalar, one neutral pseudoscalar, and one charged scalar. Electroweak symmetry breaking in a model with two Higgs doublets will be elaborated on in more detail in Sec. 3.2, as part of the treatment of the Minimal Supersymmetric Standard Model (MSSM).

An alternative, bottom-up approach is to impose the requirements of unitarity and gauge invariance directly onto the simplified model instead of deriving the simplified model from a UV-completion [125].

In our analysis, we will use the MSSM and NMSSM, described in Sec. 3.2 and Sec. 3.3, as UV-complete frameworks for dark matter.

Mono-X from ISR

Independent of the model framework, one type of topology that can always produce a mono-X signal is initial state radiation (ISR). As long as DM can be produced from a quark initial state through a mediator or some EFT operator, a jet, photon, or vector-boson can be radiated off the initial state quarks. Representative diagrams for ISR mono-jet, ISR mono-photon, and ISR mono-Z are shown in Fig. 2.4. While all three diagrams shown in Fig. 2.4 exhibit the same structure, the involved couplings are different. Neglecting the Z boson mass, this leads to the simple estimate for the cross sections [126]

$$
\begin{aligned}
\frac{\sigma_{\chi\chi\gamma}}{\sigma_{\chi\chi j}} &\approx \frac{\alpha}{\alpha_s}\frac{Q_q^2}{C_F} \approx \frac{1}{40} \\
\frac{\sigma_{\chi\chi\ell\ell}}{\sigma_{\chi\chi j}} &\approx \frac{\alpha}{\alpha_s}\frac{Q_q^2 s_w^2}{C_F}\,\mathrm{BR}(Z\to\ell^+\ell^-) \approx \frac{1}{2000}\,.
\end{aligned}
\tag{2.55}
$$

Including the Z mass, one finds $\sigma_{\chi\chi\ell\ell}/\sigma_{\chi\chi j} \approx 10^{-4}$.

Moreover, the scaling relations in Eq. (2.55) also apply to the leading $Z(\to \nu\bar{\nu})Z$ background. Further, the similarity of the diagrams suggests that kinematic x-distributions should have roughly the same shape for the different types of ISR processes [126], i.e.

$$
\frac{1}{\sigma_{\chi\chi j}}\frac{d\sigma_{\chi\chi j}}{dx} \approx \frac{1}{\sigma_{\chi\chi\gamma}}\frac{d\sigma_{\chi\chi\gamma}}{dx} \approx \frac{1}{\sigma_{\chi\chi ff}}\frac{d\sigma_{\chi\chi ff}}{dx}\,. \tag{2.56}
$$

Fig. 2.5 illustrates this point for a simplified model with a heavy vector mediator Z'. Indeed, there is no visible difference between the shapes of the distributions for the different mono-X signals. The same applies to the shapes of the background distributions.

If the leading uncertainties are statistical, the significances are given by

$$
n_{\sigma,X} = \sqrt{\epsilon_X \mathcal{L}}\,\frac{\sigma_{\chi\chi X}}{\sqrt{\sigma_{\nu\nu X}}}\,, \tag{2.57}
$$

with $\mathcal{L}$ denoting the luminosity and ϵ_X the efficiency for acceptance and other cuts. Hence, comparing mono-photon and mono-jet significances, one finds [126]

$$
\frac{n_{\sigma,\gamma}}{n_{\sigma,j}} \approx \sqrt{\frac{\epsilon_\gamma}{\epsilon_j}}\sqrt{\frac{\sigma_{\chi\chi\gamma}}{\sigma_{\chi\chi j}}} \approx \frac{1}{6.3}\sqrt{\frac{\epsilon_\gamma}{\epsilon_j}}\,, \tag{2.58}
$$

and analogously for mono-Z. Therefore, as long as the efficiencies do not strongly prefer photons over jets, mono-jet is by far the most promising ISR mono-X channel. Mono-Z, mono-W and mono-Higgs, on the other hand, are negligible as long as only initial state radiation is considered.

Hence, to understand where large Mono-Z, mono-W or mono-Higgs rates could originate from we need to study a different type of topology. A more promising class

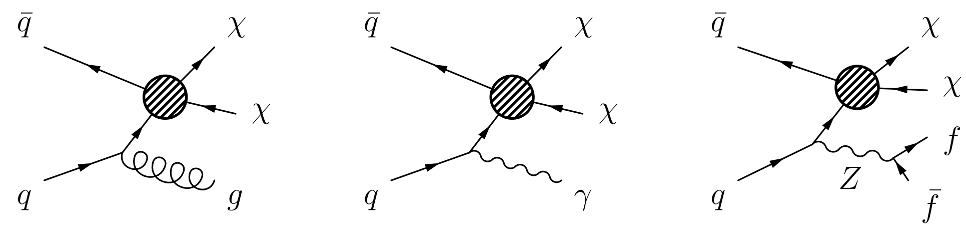

Figure 2.4: Feynman diagrams contributing to mono-X production. Figure from Ref. [126].

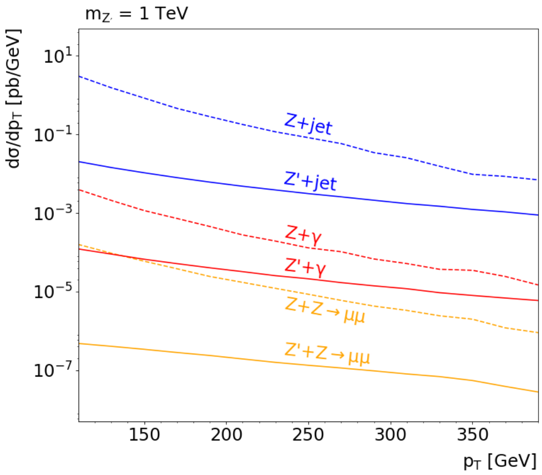

Figure 2.5: Transverse momentum spectrum for different mono-X signals and backgrounds assuming a heavy vector mediator. Figure from Ref. [126].

of topologies, namely decays in the final state, appears for non-minimal dark matter sectors. To study these processes we employ the Minimal and the Next-to-Minimal Supersymmetric Standard Model (MSSM and NMSSM) as frameworks for WIMPs as part of an extended dark matter sector.

3 Supersymmetric dark matter

Supersymmetry (SUSY) is the unique extension of the symmetries of space and time [127, 128]. It extends the Poincaré algebra by fermionic generators. This has the remarkable consequence of relating bosons to fermionic superpartners and fermions to bosonic superpartners. Supersymmetry not only provides a WIMP DM candidate, but is also motivated by gauge coupling unification and as a solution to the hierarchy problem [129]. Regarding the latter, supersymmetry leads to a cancellation between the bosonic and fermionic loop contributions to the Higgs mass. This explains why the Higgs mass is not subject to large quantum corrections from heavy particles beyond the Standard Model. In this chapter, we briefly introduce the MSSM and NMSSM, focusing on their dark matter sectors. We follow the presentation and conventions of Ref. [129] and Ref. [130].

3.1 SUSY generalities

In $N = 1$ supersymmetry, the Poincaré algebra, which generates the Poincaré group, is extended by Grassmann-valued generators Q fulfilling the (anti-)commutation relations

$$\begin{aligned}
\{Q_\alpha, \overline{Q}_{\dot\beta}\} &= 2\sigma^\mu_{\alpha\dot\beta}\, P_\mu \\
\{Q_\alpha, Q_\beta\} &= \{\overline{Q}_{\dot\alpha}, \overline{Q}_{\dot\beta}\} = 0 \\
[P_\mu, Q_\alpha] &= [P_\mu, \overline{Q}_{\dot\alpha}] = 0
\end{aligned} \tag{3.1}$$

with spinor indices $\alpha, \dot\alpha$. $\sigma^\mu_{\alpha\dot\alpha}$ denote the Pauli matrices. In supersymmetric extensions of the Standard Model, a particle and its superpartner form a supermultiplet. Supermultiplets are irreducible representations of the supersymmetry algebra. For example, for a massless particle with $P_\mu = (E, 0, 0, E)$ and, hence,

$$\sigma^\mu_{\alpha\dot\alpha} P_\mu = \begin{pmatrix} 0 & 0 \\ 0 & 4E \end{pmatrix} , \tag{3.2}$$

the ladder operators

$$a \coloneqq \frac{1}{\sqrt{4E}}\, Q_2 \ , \quad a^\dagger \coloneqq \frac{1}{\sqrt{4E}}\, \overline{Q}_{\dot 2} \tag{3.3}$$

define a fermionic harmonic oscillator, i.e. $\{a, a^\dagger\} = 1$. One can show that

$$[J_3, a] = -\frac{1}{2} a \ , \quad [J_3, a^\dagger] = \frac{1}{2} a^\dagger \ . \tag{3.4}$$

Hence, a lowers the helicity of a state by $\frac{1}{2}$, while $a^\dagger$ raises it by $\frac{1}{2}$, thus turning bosonic states into fermionic states, and vice versa. In supersymmetric extensions of the SM, the SM fermions and their superpartners form chiral multiplets, which are defined by the lowest-helicity state having helicity $\lambda_0 = 0$. Applying $a^\dagger$ yields

$$a^\dagger \, |\lambda = 0\rangle \; = \; |\lambda = \frac{1}{2}\rangle \; . \tag{3.5}$$

The helicity can only be raised once, since $(a^\dagger)^2 = a^2 = 0$. To make the theory CPT-invariant, one needs to add the CPT conjugates. Hence, the full massless chiral multiplet consists of the states

$$\left\{ |-\frac{1}{2}\rangle \, , \; |0\rangle \, , \; |0\rangle_{\mathrm{CPT}} \, , \; |\frac{1}{2}\rangle \right\} \; , \tag{3.6}$$

where each state is labeled by its helicity. Thus, a chiral multiplet comprises two scalar degrees of freedom, one chiral (positive helicity) Weyl fermion, and one anti-chiral (negative helicty) Weyl fermion, exactly as needed to contain an SM fermion and its scalar superpartner.

Starting instead from the state with $\lambda_0 = \frac{1}{2}$, such that

$$a^\dagger \, |\frac{1}{2}\rangle = |1\rangle \; , \tag{3.7}$$

and again adding the CPT conjugate, defines a vector multiplet

$$\left\{ |-1\rangle \, , \; |-\frac{1}{2}\rangle \, , \; |\frac{1}{2}\rangle \, , \; |1\rangle \right\} \; , \tag{3.8}$$

containing a chiral and an anti-chiral Weyl fermion, and a massless vector. In supersymmetric extensions of the SM, the latter are the gauge bosons, and the former their fermionic superpartners.

The choices $\lambda_0 = 1$ and $\lambda = \frac{3}{2}$ correspond to the gravitino multiplet and the gravity multiplet, respectively.

Massive chiral and vector multiplets can be defined in an analogous fashion, see e.g. Ref. [130]. Finally, according to Eq. (3.1), the generators Q commute with P_μ and, hence, also with $P_\mu P^\mu = m^2$. Therefore, if SUSY is unbroken, all states in a supermultiplet have the same mass.

As a consequence of extending the Poincaré algebra by anticommuting generators Q_α and $Q_{\dot\alpha}$, spacetime obtains Grassmann-valued directions θ_α and $\overline{\theta}_{\dot\alpha}$. In this space, the generators of SUSY transformations are represented by

$$\begin{aligned} Q_\alpha &= -i\frac{\partial}{\partial\theta^\alpha} - \sigma^\mu_{\alpha\dot\beta}\overline{\theta}^{\dot\beta}\partial_\mu \; , \\ \overline{Q}_{\dot\alpha} &= \; i\frac{\partial}{\partial\overline{\theta}_{\dot\alpha}} + \theta^\beta\sigma^\mu_{\beta\dot\alpha}\partial_\mu \; . \end{aligned} \tag{3.9}$$

A SUSY transformation hence acts on a (scalar) superfield as

$$e^{-i(\epsilon Q+\bar{\epsilon}\overline{Q})} f\left(x^{\mu}, \theta, \overline{\theta}\right) = f\left(x^{\mu} + i\epsilon\sigma^{\mu}\overline{\theta} + i\theta\sigma^{\mu}\bar{\epsilon}, \theta + \epsilon, \overline{\theta} + \bar{\epsilon}\right) \tag{3.10}$$

For the theory to be supersymmetric, the action S has to be invariant under SUSY transformations. Using superfields, which are fields in superspace, i.e. functions of x, θ and $\overline{\theta}$, it is possible to build actions that are manifestly invariant under the transformation Eq. (3.10). In addition to being invariant under SUSY transformations, the action needs to be a spacetime scalar of mass dimension four. The ordinary action in four dimensional spacetime is then obtained by integrating over the Grassmann coordinates, i.e.

$$\int d^4x\, \mathcal{L} \;=\; \int d^4x\, d^2\theta\, d^2\overline{\theta}\, \mathcal{L}_{\text{SUSY}}\,. \tag{3.11}$$

Now, we can introduce the types of superfields corresponding to the chiral and vector multiplets introduced above.

A chiral superfield $\Phi(x, \theta, \overline{\theta})$ is defined as fulfilling the constraint

$$\overline{D}_{\dot{\alpha}}\, \Phi = 0\,, \tag{3.12}$$

where D_{α} denotes the SUSY-covariant derivative, which is defined such that $\{D, Q\} = 0$. Explicitly, one finds

$$\begin{aligned} D_{\alpha} &= \frac{\partial}{\partial\theta^{\alpha}} + i\sigma^{\mu}_{\alpha\dot{\beta}}\overline{\theta}^{\dot{\beta}}\partial_{\mu}\,, \\ \overline{D}_{\dot{\alpha}} &= -\frac{\partial}{\partial\overline{\theta}^{\dot{\alpha}}} - i\theta^{\beta}\sigma^{\mu}_{\beta\dot{\alpha}}\partial_{\mu}\,. \end{aligned} \tag{3.13}$$

Using the constraint Eq. (3.12), one can show that chiral superfields take the form

$$\begin{aligned} \Phi(x, \theta, \overline{\theta}) \;&= \phi(x) - i\theta\sigma^{\mu}\overline{\theta}\partial_{\mu}\phi(x) - \frac{1}{4}\theta^2\overline{\theta}^2\partial^2\phi(x) + \sqrt{2}\theta\psi(x) \\ &\quad + \frac{i}{\sqrt{2}}\theta^2\partial_{\mu}\psi(x)\sigma^{\mu}\overline{\theta} + \theta^2 F(x)\,. \end{aligned} \tag{3.14}$$

Here, $\phi(x)$ denotes a complex scalar field and $\psi(x)$ a Weyl fermion. The second scalar field $F(x)$ can be shown to be only an auxiliary field, which can be eliminated from the action using the equations of motion. In addition, the equations of motion reduce the number of fermionic degrees of freedom by half. Hence, on-shell, i.e. using the equations of motion, Φ and $\overline{\Phi}$ together comprise 2 scalar and 2 fermionic degrees of freedom, which matches the degrees of freedom in the chiral multiplet, cf. Eq. (3.6).

The kinetic part of the action can then be constructed as

$$\begin{aligned} S_{\text{kin}} &= \int d^4x d^2\theta d^2\overline{\theta}\, \overline{\Phi}\Phi \\ &= \int d^4x\, \left(\partial_{\mu}\overline{\phi}\partial^{\mu}\phi + \partial_{\mu}\psi\sigma^{\mu}\overline{\psi} + \overline{F}F\right) \end{aligned} \tag{3.15}$$

More generally, Φ and $\overline{\Phi}$ can be combined into a real-valued Kähler potential $K(\overline{\Phi}, \Phi)$.

Furthermore, since any holomorphic function of Φ is again a chiral superfield, terms of the form

$$\int d^4x d^2\theta \, W(\Phi) \; + \; h.c. \tag{3.16}$$

where $W(\Phi)$ is holomorphic, are SUSY invariant. The function $W(\Phi)$ is called superpotential.

Vector superfields V are defined as real superfields, i.e. fulfilling

$$V = V^\dagger \; . \tag{3.17}$$

In so-called Wess-Zumino gauge these take the form

$$V(x, \theta, \overline{\theta}) = \theta\sigma^\mu\overline{\theta}A_\mu(x) + i\theta^2\overline{\theta}\,\overline{\lambda}(x) - i\overline{\theta}^2\theta\lambda(x) + \frac{1}{2}\theta^2\overline{\theta}^2 D(x) \; , \tag{3.18}$$

with a massless vector field A_μ, a Weyl fermion λ, and another auxiliary field D. The auxiliary field can again be eliminated by the equations of motion. Hence, on-shell the degrees of freedom are the same as in the vector multiplet given in Eq. (3.8). To build a supersymmetric action from V, one can exploit the fact that the gaugino superfield defined as

$$\begin{aligned} W_\alpha &= -\frac{1}{4}\overline{D}^2 D_\alpha V \; , \\ \overline{W}_{\dot{\alpha}} &= -\frac{1}{4}D^2\overline{D}_{\dot{\alpha}} V \end{aligned} \tag{3.19}$$

is a chiral superfield. By explicit calculation one finds

$$W_\alpha = \lambda_\alpha + \theta_\alpha D - \left(\sigma^{\mu\nu}\theta\right)_\alpha F_{\mu\nu} + i\theta^2 \left(\sigma^\mu\partial_\mu\overline{\lambda}\right)_\alpha \; . \tag{3.20}$$

Since W_α has mass dimension $[W_\alpha] = \frac{3}{2}$, the only renormalizable term that can be built from it reads

$$\frac{1}{4g^2}\int d^2\theta W^\alpha W_\alpha \; + \; h.c. \; , \tag{3.21}$$

where we neglect non-perturbative effects, by assuming a vanishing theta angle $\theta_{\mathrm{YM}} = 0$. Furthermore, a so-called Fayet-Iliopoulos term

$$S_{\mathrm{FI}} = \xi \int d^4x d^2\theta d^2\overline{\theta} \; V \tag{3.22}$$

can also appear in the action.

Finally, in an Abelian gauge theory, in which the chiral superfields charged under the gauge group transform as

$$\Phi \to e^{-q\Lambda}\Phi \; , \tag{3.23}$$

the Kähler potential needs to be modified to $K(\overline{\Phi}, e^{2gV}\Phi)$ to preserve gauge invariance.

In addition, for a non-Abelian gauge group with generators T^a acting on the chiral superfields as

$$\Phi \to e^{-\Lambda^a T^a}\Phi \ , \tag{3.24}$$

the gaugino superfield needs to be modified. In Wess-Zumino gauge, it now takes the form

$$W^a_\alpha = -\frac{1}{4}\overline{D}^2 D_\alpha V + \frac{1}{8}\overline{D}^2 [V, D_\alpha V] \ . \tag{3.25}$$

Supersymmetric non-Abelian gauge theories are also called Super-Yang-Mills theories. Collecting all terms, the most general Lagrangian for a Super-Yang-Mills theory including matter consists of the parts

$$\mathcal{L} = \mathcal{L}_{\text{SYM}} + \mathcal{L}_{\text{matter}} + \mathcal{L}_{\text{FI}} \ , \tag{3.26}$$

which read

$$\mathcal{L}_{\text{SYM}} = \frac{1}{32\pi}\text{Im}[\ \tau \int d^2\theta \ \text{Tr}\ W^\alpha W_\alpha] \ , \tag{3.27}$$

with the complexified gauge coupling $\tau = \theta_{\text{YM}}/(2\pi) + i\ 4\pi/g^2$,

$$\mathcal{L}_{\text{FI}} = \xi \int d^2\theta d^2\overline{\theta}\ V \ , \tag{3.28}$$

and

$$\mathcal{L}_{\text{matter}} = \int d^2\theta d^2\overline{\theta}\ \overline{\Phi} e^{2gV}\Phi \ + \ \left(\int d^2\theta \ W(\Phi) \ + \ h.c.\right) \ . \tag{3.29}$$

3.2 Minimal Supersymmetric Standard Model

The Minimal Supersymmetric Standard Model (MSSM) is the minimal $N = 1$ supersymmetric extension of the Standard Model. It is minimal in the sense that it adds the lowest number of new particles. Moreover, any other supersymmetric extension of the SM has to include the MSSM as a subsector [130].

In the MSSM, the SM quarks and leptons are placed inside chiral supermultiplets/superfields together with their scalar superpartners, called squarks and sleptons, respectively. Furthermore, the Higgs boson, being a scalar particle, is also contained in a chiral multiplet, whose fermionic components are called higgsinos. However, instead of one, supersymmetry requires two Higgs doublets, H_u and H_d, for two separate reasons. First, the superpotential has to be holomorphic, as described in Sec. 3.1. Hence, it is not possible to use both the Higgs doublet ϕ and its

Names	superfield	spin 0	spin 1/2	$SU(3)_C,\ SU(2)_L,\ U(1)_Y$
squarks, quarks	Q	$(\tilde{u}_L\ \ \tilde{d}_L)$	$(u_L\ \ d_L)$	$(\,\mathbf{3},\ \mathbf{2}\,,\ \frac{1}{6})$
($\times 3$ families)	$\overline{u}$	$\tilde{u}^*_R$	$u^\dagger_R$	$(\,\overline{\mathbf{3}},\ \mathbf{1},\ -\frac{2}{3})$
	$\overline{d}$	$\tilde{d}^*_R$	$d^\dagger_R$	$(\,\overline{\mathbf{3}},\ \mathbf{1},\ \frac{1}{3})$
sleptons, leptons	L	$(\tilde{\nu}\ \ \tilde{e}_L)$	$(\nu\ \ e_L)$	$(\,\mathbf{1},\ \mathbf{2}\,,\ -\frac{1}{2})$
($\times 3$ families)	$\overline{e}$	$\tilde{e}^*_R$	$e^\dagger_R$	$(\,\mathbf{1},\ \mathbf{1},\ 1)$
Higgs, higgsinos	H_u	$(H_u^+\ \ H_u^0)$	$(\tilde{H}_u^+\ \ \tilde{H}_u^0)$	$(\,\mathbf{1},\ \mathbf{2}\,,\ +\frac{1}{2})$
	H_d	$(H_d^0\ \ H_d^-)$	$(\tilde{H}_d^0\ \ \tilde{H}_d^-)$	$(\,\mathbf{1},\ \mathbf{2}\,,\ -\frac{1}{2})$

Table 3.1: Chiral supermultiplets in the MSSM. Adapted from Ref. [129].

Names	spin 1/2	spin 1	$SU(3)_C,\ SU(2)_L,\ U(1)_Y$
gluino, gluon	$\tilde{g}$	g	$(\,\mathbf{8},\ \mathbf{1}\,,\ 0)$
winos, W bosons	$\tilde{W}^\pm\ \ \tilde{W}^0$	$W^\pm\ \ W^0$	$(\,\mathbf{1},\ \mathbf{3}\,,\ 0)$
bino, B boson	$\tilde{B}^0$	B^0	$(\,\mathbf{1},\ \mathbf{1}\,,\ 0)$

Table 3.2: Vector supermultiplets in the MSSM. From Ref. [129].

charge conjugate ϕ^c to give masses to up-type quarks, down-type quarks, and leptons. Instead, a second Higgs doublet with opposite weak hypercharge assignment is needed. Secondly, the higgsinos are additional fermions carrying weak hypercharge. If there were only one Higgs doublet in the model, this would lead to a gauge anomaly rendering the theory inconsistent. Tab. 3.1 gives a complete list of chiral superfields in the MSSM, and the SM particles and superpartners they contain.

Analogously, the gauge bosons and their spin-$\frac{1}{2}$ superpartners, the gauginos, are placed inside vector multiplets, as summarized in Tab. 3.2.

The superpotential is given by

$$W_{\text{MSSM}} = \mathbf{Y_u}\,\overline{u}\,Q\,H_u - \mathbf{Y_d}\,\overline{d}\,Q\,H_d - \mathbf{Y_e}\,\overline{e}\,L\,H_d + \mu\,H_u H_d \tag{3.30}$$

where we have suppressed flavor and gauge indices. The Yukawa matrices Y_u, Y_d, and Y_e are the same as in the Standard Model. In addition, the superpotential contains a supersymmetric mass term $H_u H_d$ for the Higgs, whose coefficient is the higgsino mass μ.

Gauge symmetries would also allow for terms in W_{MSSM} of the form [130]

$$\frac{1}{2}\lambda^{ijk} L_i L_j \overline{e}_k + (\lambda')^{ijk}\, L_i Q_j \overline{d}_k + (\mu)^i\, L_i H_u + \frac{1}{2}\,(\lambda'')^{ijk}\, u_i \overline{d}_j\, \overline{d}_k\ . \tag{3.31}$$

However, the first three of these terms violate lepton number and the last one baryon number. Experimentally, this would lead to rapid proton decay, which is in conflict with observation. A way to forbid these additional terms, which has important consequences regarding dark matter, is to introduce an additional Z_2 symmetry called R-parity. The R-parity of a field is given by

$$P_R = (-1)^{3(B-L)+2s} \, , \tag{3.32}$$

where B denotes baryon number, L lepton number, and s spin. All superpartners are odd under this symmetry, while all SM particles and Higgs bosons are even. If R-parity is conserved, any interaction between SM particles and superpartners includes an even number of superpartners. In particular, superpartners can only decay into SM particles and an odd number of superpartners. As a consequence, the lightest supersymmetric particle (LSP) is stable. If the LSP is electrically neutral it can therefore serve as a dark matter candidate.

With R-parity conserved, the MSSM with unbroken supersymmetry contains one less parameter than the SM. However, unbroken supersymmetry predicts that the superpartners have the same mass as their SM counterparts, as explained in Sec. 3.1. As no superpartners have been observed so far, this is clearly not the case. This means that supersymmetry is broken. SUSY breaking that does not spoil the UV properties of the model can be parametrized by soft terms, which are superrenormalizable, explicitly SUSY-breaking terms in the Lagrangian. In the MSSM these take the form

$$\begin{aligned}
\mathcal{L}^{\text{soft}}_{\text{MSSM}} =& \frac{1}{2}\left(M_3\tilde{g}\tilde{g} + M_2\tilde{W}\tilde{W} + M_1\tilde{B}\tilde{B} + h.c.\right) \\
& - \tilde{Q}^\dagger \mathbf{m_Q}^2 \frac{\pi^0}{\sqrt{2}} + \frac{\eta}{\sqrt{6}}\frac{\pi^0}{\sqrt{2}} + \frac{\eta}{\sqrt{6}} deQ - \tilde{L}^\dagger \mathbf{m_L}^2 \tilde{L} - \tilde{u}^*_R \mathbf{m_{\bar{u}}}^2 \tilde{u}^*_R - \tilde{d}^*_R \mathbf{m_{\bar{d}}}^2 \tilde{d}^*_R - \tilde{e}^*_R \mathbf{m_{\bar{e}}}^2 \tilde{e}^*_R \\
& - m^2_{H_u} H_u^\dagger H_u - m^2_{H_d} H_d^\dagger H_d - (bH_uH_d + h.c.) \\
& - \left(\tilde{u}^*_R \mathbf{A_u} \tilde{Q} H_u - \tilde{d}^*_R \mathbf{A_d} \tilde{Q} H_d - \tilde{e}^*_R \mathbf{A_e} \tilde{L} H_d + h.c.\right) \, .
\end{aligned} \tag{3.33}$$

Above, the first line contains soft gaugino masses, the second line soft squark and slepton masses, and the third line soft Higgs masses. The last line contains tri-linear A-terms involving sfermions and Higgs boson.

MSSM Higgs sector

Collecting all contributions to the scalar potential from the superpotential and soft terms, the Higgs scalar potential of the MSSM reads [129]

$$\begin{aligned}
V_{\text{Higgs}} =& \left(|\mu|^2 + m^2_{H_u}\right)\left(|H_u^0|^2 + |H_u^+|^2\right) + \left(|\mu|^2 + m^2_{H_d}\right)\left(|H_d^0|^2 + |H_u^-|^2\right) \\
& + \left(b\left(H_u^+ H_d^- - H_u^0 H_d^0\right) + h.c.\right) \\
& + \frac{1}{8}\left(g^2 + g'^2\right)\left(|H_u^0|^2 + |H_u^+|^2 - |H_d^0|^2 - |H_d^-|^2\right)^2 \\
& + \frac{1}{2} g^2 |H_u^+ H_d^{0*} + H_u^0 H_d^{-*}|^2
\end{aligned} \tag{3.34}$$

The mass spectrum of particles in the Higgs sector is determined by the minimum of this potential. First, the vacuum expectation value $\langle H_u^+\rangle$ can be set to zero by an $SU(2)$ rotation. Second, from the condition that $\frac{\partial V}{\partial H_u^+} = 0$ at the minimum, it follows that also $\langle H_d^-\rangle$ vanishes. Hence, electromagnetism is unbroken as required. Relations between the parameters can then be derived using the conditions $\partial V/\partial H_u^0 = 0$ and $\partial V/\partial H_d^0 = 0$ on the remaining potential. It is convenient to introduce the parameter

$$\tan\beta = \frac{v_u}{v_d}\,, \tag{3.35}$$

where $v_u = \langle H_u^0\rangle$ and $v_d = \langle H_d^0\rangle$. These fulfill the relation

$$v_u^2 + v_d^2 = v^2 \tag{3.36}$$

with v being the Higgs vev of the Standard Model. Minimizing the potential yields the relations

$$\sin(2\beta) = \frac{2b}{m_{H_u}^2 + m_{H_d}^2 + 2|\mu|^2}\,, \tag{3.37}$$

$$m_Z^2 = \frac{|m_{H_d}^2 - m_{H_u}^2|}{\sqrt{1-\sin^2(2\beta)}} - m_{H_u}^2 - m_{H_d}^2 - 2|\mu|^2\,. \tag{3.38}$$

The two Higgs doublets comprise eight real scalar degrees of freedom. After electroweak symmetry breaking, three of these become the longitudinal modes of the massive Z, W^+ and W^- bosons. The five remaining degrees of freedom form two CP-even neutral scalars h^0 and H^0, one neutral pseudoscalar A^0, and two CP-even charged scalars H^+ and H^-. These mass eigenstates are related to the gauge eigenstates by

$$\begin{pmatrix} H_u^0 \\ H_d^0 \end{pmatrix} = \begin{pmatrix} v_u \\ v_d \end{pmatrix} + \frac{1}{\sqrt{2}} R_\alpha \begin{pmatrix} h_0 \\ H^0 \end{pmatrix} + \frac{i}{\sqrt{2}} R_{\beta_0} \begin{pmatrix} G^0 \\ A^0 \end{pmatrix} \tag{3.39}$$

and

$$\begin{pmatrix} H_u^+ \\ H_d^{-*} \end{pmatrix} = R_{\beta_\pm} \begin{pmatrix} G^+ \\ H^+ \end{pmatrix}\,, \tag{3.40}$$

with the orthogonal rotation matrices

$$R_\alpha = \begin{pmatrix} \cos\alpha & \sin\alpha \\ -\sin\alpha & \cos\alpha \end{pmatrix},$$

$$R_{\beta_0} = \begin{pmatrix} \sin\beta_0 & \cos\beta_0 \\ -\cos\beta_0 & \sin\beta_0 \end{pmatrix},\ R_{\beta_\pm} = \begin{pmatrix} \sin\beta_\pm & \cos\beta_\pm \\ -\cos\beta_\pm & \sin\beta_\pm \end{pmatrix}\,. \tag{3.41}$$

At tree level, $\beta_0 = \beta_\pm = \beta$ with β as defined in Eq. (3.35) [129]. The masses of the mass eigenstates are

$$\begin{aligned}
m_{A^0}^2 &= \frac{2b}{\sin(2\beta)}, \\
m_{h^0,H^0}^2 &= \frac{1}{2}\left(m_{A^0}^2 + m_Z^2 \mp \sqrt{\left(m_{A^0}^2 - m_Z^2\right)^2 + 4m_Z^2 m_{A^0}^2 \sin^2(2\beta)}\right), \\
m_{H^\pm}^2 &= m_{A^0}^2 + m_W^2 \ ,
\end{aligned} \tag{3.42}$$

where in the second and third line the parameter b has been eliminated in favor of $m_{A^0}^2$. The angle α is determined by

$$\frac{\sin(2\alpha)}{\sin(2\beta)} = -\frac{m_{H^0}^2 + m_{h^0}^2}{m_{H^0}^2 - m_{h^0}^2}, \qquad \frac{\tan(2\alpha)}{\tan(2\beta)} = \frac{m_{A^0}^2 + m_Z^2}{m_{A^0}^2 - m_Z^2} \ . \tag{3.43}$$

From Eq. (3.42) follows that, at tree level, the mass of the light neutral CP-even Higgs is bounded from above by

$$m_{h^0} < m_Z |\cos(2\beta)| \ . \tag{3.44}$$

Hence, if h^0 is to be identified with the known 125 GeV Higgs boson, its mass needs to receive large loop corrections. Indeed, top and stop loops can provide sufficiently large corrections to lift m_{h^0} to match observation [129]. Hence, m_h can be set by, for example, adjusting the parameter A_t, defined as a component of $\mathbf{A}_u$ in Eq. (3.33). Finally, in the decoupling limit, with $m_{A^0}^2 \gg m_Z^2$ and $m_{H^0}^2 \gg m_{h^0}^2$, Eq. (3.43) implies that $\alpha = \beta - \pi/2$. In this limit, the couplings of h^0 are identical to the couplings of the Standard Model Higgs boson.

MSSM dark matter sector: electroweakinos

The neutral part of the MSSM electroweakino sector contains the bino $\tilde{B}$, the neutral wino $\tilde{W}^0$, and the two neutral higgsinos $\tilde{H}_u^0$ and $\tilde{H}_d^0$. These mix to form four mass eigenstates called neutralinos. The neutralinos are neutral Majorana fermions denoted by $\tilde{\chi}_i^0$, with $i = 1..4$. Following usual convention, we label the states $\tilde{\chi}_i^0$ in ascending order of mass from lightest to heaviest. By R-parity conservation, cf. Eq. (3.32), the lightest neutralino $\tilde{\chi}_1^0$ is a good dark matter candidate if it is the lightest supersymmetric particle (LSP). In all that follows, we assume that $\tilde{\chi}_1^0$ is the LSP and, thus, our DM candidate.

In terms of gauge eigenstates $\tilde{\psi}^0 = (\tilde{B}, \tilde{W}^0, \tilde{H}_u^0, \tilde{H}_d^0)$, the mass term in the Lagrangian reads

$$\mathcal{L} \supset -\frac{1}{2}\left(\tilde{\psi}^0\right)^T \mathbf{M}_\chi \, \tilde{\psi}^0 \ + \ h.c. \tag{3.45}$$

The mass matrix takes the form

$$\mathbf{M}_\chi = \begin{pmatrix} M_1 & 0 & -m_Z c_\beta s_w & m_Z s_\beta s_w \\ 0 & M_2 & m_Z c_\beta c_w & -m_Z s_\beta c_w \\ -m_Z c_\beta s_w & m_Z c_\beta c_w & 0 & -\mu \\ m_Z s_\beta s_w & -m_Z s_\beta c_w & -\mu & 0 \end{pmatrix} . \tag{3.46}$$

The diagonal entries M_1 and M_2 stem from the soft SUSY breaking mass terms shown in Eq. (3.33). The higgsino mass entries $\sim \mu$ are off-diagonal since the μ-term in the superpotential combines H_u and H_d, cf. Eq. (3.30.) The remaining entries stem from Higgs-higgsino-gaugino interaction terms, with the Higgses replaced by their vevs. M_1 and M_2 can be chosen real and positive by suitable rotations of the fields $\tilde{B}$ and $\tilde{W}^0$ by a complex phase. H_u and H_d, on the other hand, are already fixed by the Higgs sector, described in Sec. 3.2. Hence, μ has a sign that cannot be rotated away. In general, μ can also be complex. However, this leads to additional CP-violation. In the following, we, therefore, consider only real values of μ.

The mass matrix $\mathbf{M}_\chi$ can be diagonalized by a unitary matrix $\mathbf{N}$, chosen such that

$$\mathbf{N}^* \mathbf{M}_\chi \mathbf{N}^{-1} = \mathrm{diag}\left(m_{\tilde{\chi}_1^0}, m_{\tilde{\chi}_2^0}, m_{\tilde{\chi}_3^0}, m_{\tilde{\chi}_4^0} \right) . \tag{3.47}$$

The neutralino mass eigenstates are thus given by

$$\tilde{\chi}_i^0 \ = \ N_{ij} \, \tilde{\psi}_j \ . \tag{3.48}$$

Hence, the elements N_{ij} of the neutralino mixing matrix describe the bino, wino, and higgsino portions in each of the neutralinos and, thus, their couplings. Even independent of SUSY, the MSSM neutralino sector can be viewed as a model for a mixed dark sector consisting of singlets, doublets and triplets under $SU(2)_L$.

The chargino sector comprises the charged winos and the charged higgsinos. These mix to two charged Dirac fermions called charginos. In terms of the gauge eigenstates $\tilde{\psi}^\pm = (\tilde{W}^+, \tilde{H}_u^+, \tilde{W}^-, \tilde{H}_d^-)$, the mass term is given by

$$\mathcal{L} = -\frac{1}{2} \left(\tilde{\psi}^\pm \right)^T \mathbf{M}_{\tilde{\chi}^\pm} \, \tilde{\psi}^\pm \ + \ h.c. \ , \tag{3.49}$$

where

$$\mathbf{M}_{\tilde{\chi}^\pm} \ = \ \begin{pmatrix} \mathbf{0} & \mathbf{X}^T \\ \mathbf{X} & \mathbf{0} \end{pmatrix} , \tag{3.50}$$

with the 2×2 matrix

$$\mathbf{X} = \begin{pmatrix} M_2 & \sqrt{2} m_W s_\beta \\ \sqrt{2} m_W c_\beta & \mu \end{pmatrix} . \tag{3.51}$$

Since the matrix $\mathbf{X}$ is not symmetric, two unitary matrices $\mathbf{U}$ and $\mathbf{V}$ are necessary to diagonalize it. We then have

$$\mathbf{U}^*\mathbf{X}\mathbf{V}^{-1} = \mathrm{diag}\left(m_{\tilde{\chi}_1^\pm}, m_{\tilde{\chi}_2^\pm}\right) \ . \tag{3.52}$$

The mass eigenstates are related to the gauge eigenstates via

$$\begin{pmatrix} \tilde{\chi}_1^+ \\ \tilde{\chi}_2^+ \end{pmatrix} = \mathbf{V} \begin{pmatrix} \tilde{W}^+ \\ \tilde{H}_u^+ \end{pmatrix}, \qquad \begin{pmatrix} \tilde{\chi}_1^- \\ \tilde{\chi}_2^- \end{pmatrix} = \mathbf{U} \begin{pmatrix} \tilde{W}^- \\ \tilde{H}_d^- \end{pmatrix} \ . \tag{3.53}$$

Neutralino and chargino couplings

In general, neutralinos and charginos couple to W, Z and Higgs bosons, squarks, and sleptons. In the following, we will focus on the interactions with the electroweak and Higgs sector. The relevant couplings are:

Z-neutralino-neutralino interaction: Neutralinos couple to the Z boson through their higgsino content. This is an axial-vector interaction, since the vector current $\bar{\tilde{\chi}}\gamma^\mu\tilde{\chi}$ vanishes for Majorana fermions. The coupling strength reads

$$g_{Z\tilde{\chi}_i^0\tilde{\chi}_j^0} = \frac{g}{2c_w}\left(N_{i3}N_{j3} - N_{i4}N_{j4}\right) \ . \tag{3.54}$$

Higgs-neutralino-neutralino interaction: The scalar coupling to the light Higgs, which is induced by the gaugino-higgsino content in the neutralinos, reads

$$g_{h\tilde{\chi}_i^0\tilde{\chi}_j^0} = \frac{1}{2}\ \left(g'N_{i1} - gN_{i2}\right)\ \left(s_\alpha\ N_{j3} + c_\alpha\ N_{j4}\right)\ + (i \leftrightarrow j) \ . \tag{3.55}$$

In the decoupling limit, with $\alpha = \beta - \pi/2$, the coupling takes the approximate form

$$g_{h\tilde{\chi}_i^0\tilde{\chi}_j^0} \approx \frac{1}{2}\ \left(g'N_{i1} - gN_{i2}\right)\ s_\beta \left(-\frac{N_{j3}}{t_\beta} + N_{j4}\right)\ + (i \leftrightarrow j) \ . \tag{3.56}$$

W-neutralino-chargino interaction: A chargino and a neutralino couple to W bosons through their higgsino content or their wino content. The coupling is, hence, given by

$$g_{W\tilde{\chi}_i^0\tilde{\chi}_j^+} = g\ \left(\frac{1}{\sqrt{2}}N_{i4}V_{j2}^* - N_{i2}V_{j1}^*\right) \ . \tag{3.57}$$

3.3 NMSSM dark matter sector

The Next-to-Minimal Supersymmetric Standard Model (NMSSM) extends the superfield content of the MSSM by one chiral superfield S, which is a singlet with respect to all SM gauge groups. In terms of particles, this adds one scalar and one pseudoscalar to the Higgs sector, as well as a singlino to the neutralino sector. In our presentation of the NMSSM and its DM sector, we follow Ref. [131, 132]. The main theoretical motivation for the NMSSM is the μ-problem: The Higgs sector of the MSSM relates m_{H_u}, m_{H_d}, and μ to m_Z, as shown in Eq. (3.38), and, thus, to the electroweak scale. The soft masses m_{H_u} and m_{H_d} are expected to be on the SUSY breaking scale and, hence, close to the electroweak scale, if SUSY solves the hierarchy problem. However, μ is not tied to the electroweak scale at all. Therefore, fine-tuning seems to be needed to fulfill Eq. (3.38). The NMSSM solves the μ-problem by generating μ as a vev, whose value is determined by soft SUSY-breaking parameters. The superpotential of the scale-invariant NMSSM reads

$$W_{\text{NMSSM}} = \lambda S H_u H_d + \frac{\kappa}{3} S^3 + W_{\text{Yukawa}} \, , \tag{3.58}$$

with W_{Yukawa} the same as in the MSSM. λ and κ are new, dimensionless parameters coupling the singlet to the Higgs sector and to itself, respectively. When S assumes its vev, it generates an effective μ-term given by

$$\mu = \lambda \langle S \rangle \, . \tag{3.59}$$

The additional soft terms are of the form

$$\mathcal{L}^{\text{soft}}_{\text{NMSSM}} \supset m_S^2 |S|^2 - \left(\lambda A_\lambda H_u H_d + \frac{1}{3} \kappa A_\kappa S^3 + h.c. \right) \, . \tag{3.60}$$

Minimizing the scalar potential relates m_S to $\langle S \rangle$ and, thus, to μ. Hence, either m_S or μ can be used as a free parameter.

NMSSM Higgs sector

In the Higgs sector, the two real, scalar degrees of freedom in the singlet superfield give rise to one additional, singlet scalar and one additional, singlet pseudoscalar. From the dark matter perspective, these serve as additional mediators.

In the basis (H, h, S_R), with h and H defined in terms of H_u^0 and H_d^0 as in the MSSM, and S_R denoting the real part of the complex scalar S, the scalar mass matrix reads

$$\mathbf{M}^2_{H,h,S_R} = m_Z^2 \begin{pmatrix} s_{2\beta}^2 \delta + \frac{2\mu}{s_{2\beta} m_Z^2} (A_\lambda + \tilde{\kappa}\mu) & c_{2\beta} s_{2\beta} \delta & -c_{2\beta} \frac{\tilde{\lambda}}{m_Z} (A_\lambda + \tilde{\kappa}\mu) \\ \cdot & c_{2\beta}^2 + s_{2\beta}^2 \tilde{\lambda}^2 & \frac{2\tilde{\lambda}}{m_Z} \left(\mu - s_{2\beta} \frac{A_\lambda}{2} - s_{2\beta} \tilde{\kappa}\mu \right) \\ \cdot & \cdot & s_{2\beta} \frac{\tilde{\lambda}^2 A_\lambda}{2\mu} + \frac{\tilde{\kappa}\mu}{m_Z^2} (A_\kappa + 4\tilde{\kappa}\mu) \end{pmatrix} , \tag{3.61}$$

with the convenient combinations

$$\tilde{\kappa} = \frac{\kappa}{\lambda} \, , \tag{3.62}$$

$$\tilde{\lambda} = \frac{\lambda}{g} \, , \tag{3.63}$$

$$\delta = 1 - \tilde{\lambda} \, . \tag{3.64}$$

Like in the MSSM, in the decoupling limit with $m_H^2 \gg m_h^2$, h has the couplings of the SM Higgs boson. Furthermore, mixing between the singlet and h is suppressed if the off-diagonal element M_{23} in the mass matrix, Eq. (3.61) vanishes. This is the case if [132]

$$A_\lambda = 2\mu \left(\frac{1}{s_{2\beta}} - \tilde{\kappa} \right) . \tag{3.65}$$

In this way, constraints from the Higgs coupling strength can be avoided.

Similarly, the pseudoscalar mass matrix in the basis (A, S_I), where A is again defined like in the MSSM, and S_I denotes the imaginary part of S, reads

$$\mathbf{M}^2_{A,S_I} = m_Z^2 \begin{pmatrix} \frac{2\mu(A_\lambda + \tilde{\kappa}\mu)}{s_{2\beta} m_Z^2} & \frac{tilde\lambda}{m_Z} \left(A_\lambda - 2\tilde{\kappa}\mu \right) \\ \cdot & s_{2\beta}\tilde{\lambda}^2 \left(\frac{A_\lambda}{2\mu} + 2\tilde{\kappa} \right) - 2\tilde{\kappa} \frac{\mu A_\kappa}{m_Z^2} \ . \end{pmatrix} \tag{3.66}$$

NMSSM neutralino sector

Finally, the fermionic component of the singlet superfield, called singlino, enters the neutralino sector. Thus, the neutralino mass matrix is extended to a 5×5 matrix, which reads

$$\mathbf{M}_\chi = \begin{pmatrix} M_1 & 0 & -m_Z c_\beta s_w & m_Z s_\beta s_w & 0 \\ 0 & M_2 & m_Z c_\beta c_w & -m_Z s_\beta c_w & 0 \\ -m_Z c_\beta s_w & m_Z c_\beta c_w & 0 & -\mu & -m_Z s_\beta \tilde{\lambda} \\ m_Z s_\beta s_w & -m_Z s_\beta c_w & -\mu & 0 & -m_Z c_\beta \tilde{\lambda} \\ 0 & 0 & -m_Z s_\beta \tilde{\lambda} & -m_Z c_\beta \tilde{\lambda} & 2\tilde{\kappa}\mu \end{pmatrix} . \tag{3.67}$$

The pure-singlino mass is, hence, given by $m_{\tilde{\chi}_S} = 2\tilde{\kappa}\mu$. More generally, if the LSP is predominantly, but not purely, singlino, its mass is approximately

$$m_{\tilde{\chi}} \approx 2\tilde{\kappa}\mu + \tilde{\lambda}^2 \frac{m_Z^2}{\mu} \frac{2\tilde{\kappa} - s_{2\beta}}{4\tilde{\kappa}^2 - 1} . \tag{3.68}$$

The coupling of neutralinos to a CP-even Higgs boson H_i now reads

$$\begin{aligned} g_{H_k \tilde{\chi}_i^0 \tilde{\chi}_j^0} = \frac{1}{2} [& \lambda\sqrt{2} \left(S_{k1} N_{i4} N_{j5} + S_{k2} N_{i3} N_{j5} + S_{k3} N_{i3} N_{j4} \right) \\ & - \lambda\tilde{\kappa}\sqrt{2} S_{k3} N_{i5} N_{j5} - \left(g' N_{i1} - g N_{i2} \right) \left(S_{k1} N_{j3} - S_{k2} N_{j4} \right)] \\ & + (i \leftrightarrow j) , \end{aligned} \tag{3.69}$$

where S_{ij} is the mixing matrix that rotates the CP-even weak eigenstates $(H^0_{uR}, H^0_{dR}, S_R)$ into mass eigenstates. The coupling to a pseudoscalar A_k has the same form, i.e.

$$\begin{aligned} g_{A_k \tilde{\chi}_i^0 \tilde{\chi}_j^0} = \frac{1}{2} [& \lambda\sqrt{2} \left(P_{k1} N_{i4} N_{j5} + P_{k2} N_{i3} N_{j5} + P_{k3} N_{i3} N_{j4} \right) \\ & - \lambda\tilde{\kappa}\sqrt{2} P_{k3} N_{i5} N_{j5} - \left(g' N_{i1} - g N_{i2} \right) \left(P_{k1} N_{j3} - P_{k2} N_{j4} \right)] \\ & + (i \leftrightarrow j) , \end{aligned} \tag{3.70}$$

only with S_{ij} replaced by P_{ij}, which denotes the pseudoscalar mixing matrix, again with respect to the weak eigenstates. Hence, the coupling of a singlino-higgsino LSP to a singlet-like scalar or pseudoscalar is

$$g_{h_S\tilde{\chi}_1^0\tilde{\chi}_1^0} = g_{a_S\tilde{\chi}_1^0\tilde{\chi}_1^0} = \lambda\sqrt{2}\left(N_{13}N_{14} - \tilde{\kappa}N_{15}^2\right) \ . \tag{3.71}$$

Further, the coupling of a singlino-higgsino LSP to the SM-like Higgs reads

$$g_{h_{125}\tilde{\chi}_1^0\tilde{\chi}_1^0} = -\sqrt{2}\lambda N_{15}\left(N_{13} + \frac{N_{14}}{t_\beta}\right) \ . \tag{3.72}$$

The couplings to W and Z bosons remain as in the MSSM, cf. Eq. (3.57) and Eq. (3.54), since the singlino is a gauge singlet.

3.4 Annihilation channels

Neutralinos in the MSSM can annihilate efficiently towards the observed relic density through a set of mediators. These are the SM Z and Higgs bosons, heavy new Higgs bosons, and scalar superpartners of the SM fermions [133, 134]. In the NMSSM, one additionally gains another CP-even scalar and another pseudoscalar as mediators. These mediators give rise to a large number of s-channel, t-channel, and coannihilation processes. Which of these processes dominate depends on the couplings and masses of the particles involved and, thus, on the (N)MSSM parameter space. As described in Sec. 2.3, the resulting relic density $\Omega_\chi h^2$ approximately follows the inverse thermally-averaged annihilation cross section $\langle\sigma v\rangle^{-1}$. In the following, we briefly summarize the most important channels. As we will be concerned mainly with light neutralinos, giving rise to large mono-X rates, we will focus particularly on the Z, scalar, and pseudoscalar funnel processes.

3.4.1 MSSM annihilation channels

The overview of MSSM annihilation channels in this section follows the corresponding list in Ref. [126].

Z-funnel annihilation

Annihilation through a Z boson in the s-channel, as shown in the left diagram of Fig. 3.1, is mediated by the coupling

$$g_{Z\tilde{\chi}_1^0\tilde{\chi}_1^0} = \frac{g}{2c_W}\left(N_{13}^2 - N_{14}^2\right) \ , \tag{3.73}$$

which follows from Eq. (3.54) with $i = j = 1$. The coupling vanishes for equal higgsino fractions, i.e. $N_{13} = N_{14}$, which is, however, only realized in the limit $\tan\beta \to 1$ or for very large μ, if the LSP is a pure higgsino. As shown in Tab. 3.3,

Annihilation process	σv
Z-funnel	$\frac{3g_\chi^2 g_f^2}{2\pi}\left(\frac{m_f^2}{m_Z^4}+\frac{v^2 m_\chi^2}{3\left(m_Z^2-4m_\chi^2\right)^2}\right)$
(Higgs) scalar funnel	$\frac{3v^2\, m_\chi^2\, g_\chi^2 g_f^2}{8\pi\left(m_h^2-4m_\chi^2\right)^2}$
pseudoscalar funnel	$\frac{3\, g_\chi^2 g_f^2\, m_\chi^2}{2\pi\left(m_a^2-4m_\chi^2\right)^2}$

Table 3.3: Annihilation cross sections for s-channel funnel processes for Majorana DM. Shown are the leading terms assuming small velocity v and small fermion masses m_f. g_χ and g_f denote the couplings of the mediator to DM and fermions, respectively. Note that σv is not yet thermally averaged. Formulae from Ref. [135].

the leading contribution to σv can be either s-wave or p-wave. While the s-wave term is suppressed by the masses of the fermions in the final state of the annihilation process, the p-wave term is, by definition, suppressed by the velocity v^2. Close to the Z-pole, i.e. for $m_{\tilde{\chi}_1^0} \approx m_Z/2$, the cross section is resonantly enhanced and the p-wave contribution dominates. For the correct relic density, the LSP mass typically needs to be slightly above or below 45 GeV, as annihilation directly on the pole is too efficient.

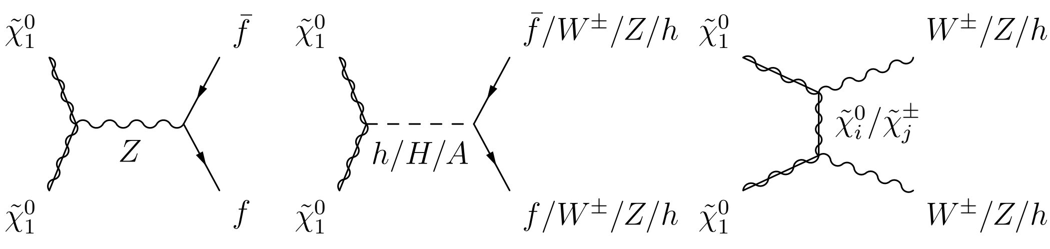

Figure 3.1: Feynman diagrams for the annihilation of neutralinos into fermions, weak bosons, and Higgs bosons, through s-channel Z, s-channel Higgs, and t-channel electroweakino exchange.

Higgs funnel annihilation

Similarly, in the Higgs funnel region around the pole of the SM-like Higgs boson, the annihilation proceeds predominantly through a Higgs s-channel diagram, shown in the center of Fig. 3.1. Here, almost all annihilations go into $b\bar{b}$ final states. The coupling follows from Eq. (3.56) as

$$g_{h\tilde{\chi}_1^0\tilde{\chi}_1^0} = (g' N_{11} + g N_{12}) \left(-\frac{N_{13}}{t_\beta} + N_{14} \right) \ , \tag{3.74}$$

which requires gaugino-higgsino mixing in the LSP. As shown in Tab. 3.3, the scalar coupling gives rise to a velocity-suppressed p-wave annihilation cross section. Due to the narrow Higgs width Γ_h, the width of the funnel region is determined by the DM velocity distribution rather than Γ_h, as described below.

Fig. 3.2 illustrates the Z- and Higgs-funnel annihilation regions for a bino-higgsino LSP for different, fixed values of μ, $M_1 = 10..80$ GeV, and $\tan\beta = 10$. In the non-relativistic limit, the squared propagator in the cross section for the relevant s-channel annihilation process reads

$$\frac{1}{\left(s - m_h^2\right)^2 + m_h^2 \Gamma_h^2} \approx \frac{1}{\left(4m_\chi^2 + m_\chi^2 v^2 - m_h^2\right)^2 + m_h^2 \Gamma_h^2} \tag{3.75}$$

for the Higgs funnel and analogously for the Z-funnel. Here, v denotes the relative velocity of the two annihilating DM particles. Since the annihilating DM particles possess a non-vanishing velocity, the resonant enhancement is strongest when the DM mass is slightly below $m_Z/2$ or $m_h/2$. Furthermore, for a fixed velocity v, the maximum value of the propagator that can be reached by adjusting m_χ is given by $(m_h^2 \Gamma_h)^{-1}$ and $(m_Z^2 \Gamma_Z^2)^{-1}$, respectively. Since $\Gamma_h \ll \Gamma_Z$, this enhancement is much stronger for the Higgs funnel. However, integrating over the velocity distribution to arrive at $\langle \sigma v \rangle$ washes out the sharp Higgs peak, leading to similar widths and similar heights for the Z- and the Higgs peak in Fig. 3.2. The width of the Z-peak is mainly given by the physical Z-width Γ_Z, resulting in an approximately symmetrical peak. The width of the Higgs peak, on the other hand, is predominantly determined by the width of the velocity distribution, leading to a strongly asymmetrical shape. Furthermore, the pure higgsino coupling to the Z, as given in Eq. (3.73), is independent of the sign of μ. In contrast, the mixed gaugino-higgsino coupling, Eq. (3.74), relevant for the Higgs funnel is larger for positive μ.

Heavy Higgs funnel annihilation

Furthermore, the pseudoscalar A gives rise to s-wave annihilation, cf. Tab. 3.3. Like the SM-Higgs funnel described above, the coupling relies on gaugino-higgsino mixing in the LSP. However, due to the strong lower bounds on its mass m_A [136], annihilation through the MSSM pseudoscalar will not play a role in the following.

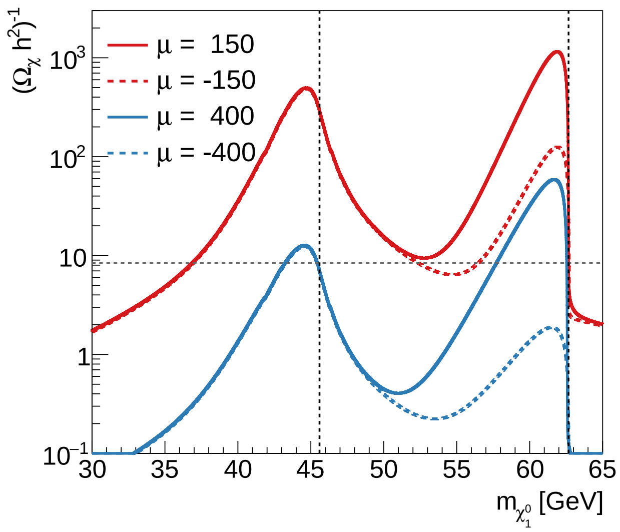

Figure 3.2: Inverse relic density near the Z-pole and Higgs pole in the MSSM. The vertical dashed lines indicate $m_Z/2$ and $m_h/2$. The horizontal dashed line indicates the inverse of the observed relic density. Figure from Ref. [126]

t-channel chargino exchange

The t-channel exchange of a chargino $\tilde{\chi}_i^\pm$, shown in the right diagram of Fig. 3.1, mediates the process $\tilde{\chi}_1^0\tilde{\chi}_1^0 \to WW$. It relies on the coupling

$$g_{W\tilde{\chi}_1^0\tilde{\chi}_i^+} = g\left(\frac{1}{\sqrt{2}}N_{14}V_{i2}^* - N_{12}V_{i1}^*\right) , \tag{3.76}$$

cf. Eq. (3.57). For this process, the LSP needs to be at least as heavy as the W boson. In addition, the chargino should not be much heavier than the LSP. For $m_{\tilde{\chi}_1^0} \lesssim 100$ GeV this process is, therefore, disfavored.

t-channel neutralino exchange

t-channel neutralino exchange can mediate the processes $\tilde{\chi}_1^0\tilde{\chi}_1^0 \to ZZ$ or $\tilde{\chi}_1^0\tilde{\chi}_1^0 \to hh$, shown in the right diagram of Fig. 3.1. The relevant couplings are given in Eq.(3.54) and Eq.(3.55), respectively. The LSP needs to be at least as heavy as the Z boson or the SM Higgs boson, respectively, for this process to be kinematically allowed.

t-channel sfermion exchange

Another t-channel process is given by sfermion exchange, for example via tau sleptons, requiring a sizable wino portion in the LSP. However, for LSP mass $m_{\tilde{\chi}_1^0} \lesssim 100$ GeV, LEP limits [137–145] on the slepton masses strongly constrain this annihilation channel.

Co-annihilation

Finally, co-annihilation processes can significantly enhance neutralino annihilation [146–151]. However, as explained in Sec. 2.3.2, this requires another supersymmetric particles with a mass that is not larger than the LSP mass by more than about 10%. Hence, chargino or slepton co-annihilation is disfavored by LEP [137–145] if $m_{\tilde{\chi}_1^0} \lesssim 100$ GeV. Moreover, since both wino and higgsino neutralinos have chargino counterparts, two neutralinos with similar masses $\lesssim 100$ GeV imply at least one chargino in the same mass range. This is again disfavored by LEP.

The masses of pure bino, wino, or higgsino DM are fixed by the observed relic density. For pure wino LSPs, this requires a mass between about 2 and 3 TeV. Similarly, pure higgsino DM has to fall in a mass range of 1 to 2 TeV [31, 32]. A pure bino LSP requires light sleptons to annihilate, as it does not couple to gauge or Higgs bosons. With general neutralino mixing, a wide DM mass range from tens of GeV to the TeV range is viable [31, 32]. In particular, for relatively light neutralinos in the mass range $\lesssim 100$ GeV, one has to dominantly rely on the Z and SM-like Higgs as mediators, requiring gaugino-higgsino mixing.

3.4.2 NMSSM annihilation channels

In contrast, the NMSSM provides an additional singlet scalar h_S and an additional singlet pseudoscalar A_S. While collider bounds force e.g. the pseudoscalar A of the MSSM to be heavy [136], these singlet mediators can be light and, hence, efficiently annihilate DM in the mass range far below 45 GeV. For this, the LSP needs to be predominantly singlino.

Light singlet scalar funnel

Like in the SM-Higgs-funnel region, the cross section for the annihilation $\tilde{\chi}_1^0\tilde{\chi}_1^0 \to h_S \to f\bar{f}$ is velocity suppressed, see Tab. 3.3. The coupling, as given in Eq. (3.71), is mediated by the singlino and higgsino fractions in the LSP. For this channel to be resonantly enhanced, it is necessary that $m_{\tilde{\chi}_1^0} \approx m_{h_S}/2$, with $m_{\tilde{\chi}_1^0}$ as in Eq. (3.68) and

$$m_{h_S} \approx s_{2\beta}\frac{\tilde{\lambda}^2 A_\lambda}{2\mu} + \frac{\tilde{\kappa}\mu}{m_Z^2}\left(A_\kappa + 4\tilde{\kappa}\mu\right) \,, \tag{3.77}$$

following Eq. (3.61).

Light singlet pseudoscalar funnel

Analogously, annihilation can proceed through a light singlet pseudoscalar, whereby $\tilde{\chi}_1^0\tilde{\chi}_1^0 \to a_S \to f\bar{f}$, which results in an s-wave, i.e. not velocity-suppressed cross section. The coupling, shown in Eq. (3.71), is the same as for the singlet scalar. The pseudoscalar mass reads

$$m_{A_S} \approx s_{2\beta}\tilde{\lambda}^2 \left(\frac{A_\lambda}{2\mu} + 2\tilde{\kappa}\right) - 2\tilde{\kappa}\frac{\mu A_\kappa}{m_Z^2} \, , \tag{3.78}$$

cf. Eq. (3.66).

3.5 Direct detection of neutralinos

As explained in Sec. 2.4.1, direct detection experiments put constraints on the interaction between DM and nucleons. In the case of neutralino DM, these are mediated by Higgs and Z bosons. Due to the Majorana nature of $\tilde{\chi}_1^0$, the coupling to the Z boson is of axial-vector form, inducing a spin-dependent neutralino-nucleon interaction. The scalar coupling to the Higgs, on the other hand, gives rise to spin-independent neutralino-nucleon interactions. Hence, for a given LSP mass $m_{\tilde{\chi}_1^0}$, spin-independent DD limits constrain the coupling $g_{h\tilde{\chi}_1^0\tilde{\chi}_1^0}$, while spin-dependent DD limits constrain $g_{Z\tilde{\chi}_1^0\tilde{\chi}_1^0}$. To illustrate the connection between the fundamental neutralino interactions described in Sec. 3.2 and the neutralino-nucleon cross section relevant for direct detection, we sketch in the following the calculation of the spin-independent cross section, mediated by the Higgs. The presentation and calculations in this section follow Ref. [61].

To determine the coupling of the Higgs to nucleons, the corresponding interaction operator can be related to the nucleon mass, determined by the trace of the energy-momentum tensor, i.e.

$$m_N \langle N|N\rangle = \langle N| T^\mu_\mu |N\rangle \, . \tag{3.79}$$

Including the contribution to T^μ_μ from the running QCD coupling α_S and taking into account contributions with opposite sign from heavy quarks $q = c, b, t$ via loops and gluon splitting, one finds that [61]

$$m_N\langle N|N\rangle = \sum_{u,d,s} m_q \langle N|\bar{q}q|N\rangle + \frac{\alpha_s}{8\pi}\left(\frac{2\times n_{\text{light}}}{3} - \frac{11}{3}N_c\right)\langle N|G^a_{\mu\nu}G^{a\,\mu\nu}|N\rangle \, . \tag{3.80}$$

This means that the nucleon mass is only determined by the light quarks u, d, s, while the heavier quarks decouple.

The dominant contribution to the Higgs-nucleon interaction, on the other hand, stems from heavy quark loops giving rise to an effective coupling between the Higgs and gluons. Here, the heavy quarks do not decouple, since the quark masses cancel between the propagators and the Yukawa couplings. The thus induced effective operator is [61]

$$\mathcal{L} \supset -i\frac{\alpha_s}{12\pi}\, h\, G^a_{\mu\nu}G^{\mu\nu\, a} \, . \tag{3.81}$$

Also taking into account the sub-dominant contribution from the Yukawa coupling to light quarks, the interaction operator between two nucleon states reads

$$\langle N|\sum_{u,d,s} m_q\, H\bar{q}q|N\rangle - \langle N|\sum_{c,b,t} \frac{\alpha_s}{12\pi}\, HG^a_{\mu\nu}G^{a\,\mu\nu}|N\rangle \ . \tag{3.82}$$

The contribution from the light quark masses to the nucleon mass, Eq. (3.80), and to the interaction operator, Eq. (3.82), are both negligible. Then, comparing Eq. (3.80) and Eq. (3.82), we find that they have the same structure, but there is a mismatch in the coefficients. Explicitly, we have

$$\begin{aligned}\langle N|\, m_q H\bar{q}q\, |N\rangle &= \frac{\frac{2n_{\text{heavy}}}{3}}{\frac{11}{3}N_c - \frac{2n_{\text{light}}}{3}}\, Hm_N\, \langle N|N\rangle \\ &= \frac{2}{9}\, Hm_N\, \langle N|N\rangle \end{aligned} \tag{3.83}$$

Hence, the nucleon Yukawa coupling to the Higgs is given by [61]

$$\frac{2}{9} m_N f_N \ , \tag{3.84}$$

with $f_N = \langle N|N\rangle$.

Now, one can use this result to calculate the spin-independent neutralino-nucleon cross section from Higgs exchange. As explained in Sec. 2.4.1, the momentum exchange in such a scattering event is much lower than the Higgs mass. Therefore, the Higgs can be integrated out, resulting in an effective four-fermion interaction between nucleons and neutralinos, with suppression scale $\Lambda = m_h$. Using Eq. (3.84), the coupling for this interaction is given by

$$g_{NN\tilde{\chi}^0_1\tilde{\chi}^0_1} = \frac{2}{9} m_N f_N\ g_{h\tilde{\chi}^0_1\tilde{\chi}^0_1} \ , \tag{3.85}$$

with the Higgs-neutralino coupling $g_{h\tilde{\chi}^0_1\tilde{\chi}^0_1}$ as in Eq. (3.74). Then, the matrix element reads [61]

$$\mathcal{M} = \frac{g_{NN\tilde{\chi}^0_1\tilde{\chi}^0_1}}{\Lambda^2}\ \bar{u}_\chi(k_2)u_\chi(k_1)\bar{u}_N(p_2)u_N(p_1) \ . \tag{3.86}$$

Spin-averaging and using the fact that all particles involved are non-relativistic, yields

$$\overline{|\mathcal{M}|^2} = \frac{16\ g^2_{NN\tilde{\chi}^0_1\tilde{\chi}^0_1}}{\Lambda^4}\ m^2_{\tilde{\chi}^0_1}\ m^2_N \ . \tag{3.87}$$

Plugging this result into the neutralino-nucleon cross section and using $\Lambda = m_h$, we find

$$\sigma^{\text{SI}}\left(\tilde{\chi}^0_1 N \to \tilde{\chi}^0_1 N\right) = \frac{1}{16\pi s}\overline{|\mathcal{M}|^2} = \frac{g^2_{NN\tilde{\chi}^0_1\tilde{\chi}^0_1}\ m^2_{\tilde{\chi}^0_1} m^2_N}{\pi\left(m_N + m_{\tilde{\chi}^0_1}\right)^2 m^4_h} \ . \tag{3.88}$$

Including the coherent enhancement with the number of nucleons, as described in Sec. 2.4.1, the SI cross section for neutralino-nucleus scattering reads

$$\sigma^{\mathrm{SI}}\left(\tilde{\chi}_1^0 A \to \tilde{\chi}_1^0 A\right) = \frac{A^2\, g^2_{NN\tilde{\chi}_1^0\tilde{\chi}_1^0}\, m^2_{\tilde{\chi}_1^0} m_N^2}{\pi \left(m_N + m_{\tilde{\chi}_1^0}\right)^2 m_h^4} \,. \tag{3.89}$$

As described in Sec. 3.4.1, the coupling $g_{h\tilde{\chi}_1^0\tilde{\chi}_1^0}$ and, thus, the SI cross section are driven by gaugino-higgsino mixing in the lightest neutralino. In addition, $g_{h\tilde{\chi}_1^0\tilde{\chi}_1^0} = (g' N_{11} - g N_{12})(-N_{13}/t_\beta + N_{14})$ vanishes if the higgsino portions fulfill the relation

$$\frac{N_{13}}{t_\beta} = N_{14} \,, \tag{3.90}$$

giving rise to a blind spot in SI direct detection. Another blind spot can arise from negative interference between t-channel with the light and the heavy Higgs scalar [152]. However, this will not be relevant in the following, as we decouple the heavy Higgs states, see Sec. 3.6.

Finally, in the NMSSM, a light, predominantly singlet-like scalar can mediate a sizable spin-independent interaction, if the cross section is sufficiently enhanced by small $\Lambda = m_{h_S}$. The relevant coupling in this case is given in Eq. (3.71).

Similarly, the axial-vector coupling to the Z boson gives rise to another four-fermion interaction once the Z is integrated out. In this case, the matrix element reads [61]

$$\mathcal{M} = \frac{g_{NN\tilde{\chi}_1^0\tilde{\chi}_1^0,Z}}{\Lambda^2}\; \bar{u}_\chi(k_2)\gamma^\mu\gamma_5 u_\chi(k_1)\bar{u}_N(p_2)\gamma_\mu\gamma_5 u_N(p_1) \,, \tag{3.91}$$

where

$$g_{NN\tilde{\chi}_1^0\tilde{\chi}_1^0} \propto g_{Zqq}\; g_{Z\tilde{\chi}_1^0\tilde{\chi}_1^0} \,. \tag{3.92}$$

The spin-dependent cross section then reads

$$\sigma^{\mathrm{SD}}\left(\tilde{\chi}_1^0 N \to \tilde{\chi}_1^0 N\right) = \frac{1}{16\pi s}\overline{|\mathcal{M}|^2} = \frac{g^2_{NN\tilde{\chi}_1^0\tilde{\chi}_1^0,Z}\, m^2_{\tilde{\chi}_1^0} m_N^2}{\pi \left(m_N + m_{\tilde{\chi}_1^0}\right)^2 m_Z^4} \,. \tag{3.93}$$

As mentioned in Sec. 3.4.1, the coupling $g_{Z\tilde{\chi}_1^0\tilde{\chi}_1^0}$ and, hence, the spin-dependent direct detection rate only vanishes for pure higgsinos.

3.6 SFitter setup

We employ the SFitter framework [133, 134, 153–156, 132] for our global analysis. However, we emphasize that, while we use SFitter for parameter scans and as a toolbox, we do not carry out a likelihood fit. We use the following tools, interfaced to SFitter:

For a given set of parameters, the MSSM particle spectrum, including the masses and mixing matrices described in Sec. 3.2, is calculated in SuSpect3 [157, 158]. Based on this spectrum, the branching ratios of supersymmetric particles and in the Higgs sector are determined using SUSY-Hit [159–161], which contains the tools SDecay and HDecay. For the NMSSM, we employ NMSSMTools, which comprises NMSPEC [162] for spectrum calculations, and NMHDECAY [163, 164] and NMSDECAY [165] for decay widths and branching ratios. We use micrOMEGAs [166] to calculate DM annihilation cross sections and the resulting relic density, as well as DM-nucleon cross sections relevant to direct detection. Finally, we employ MadGraph5 [167] to calculate leading-order cross sections for LHC processes. Next-to-leading order corrections to the processes considered by us are known and typically too small to have an impact on our discussion [168–174].

Since we focus on the electroweakino sector, we decouple all sfermions by setting their masses to 5 TeV. This assumption is further motivated by strong bounds on squark and slepton masses rendering them largely irrelevant for light neutralino dark matter in the mass range $\lesssim$ 100 GeV [175, 137–145]. Furthermore, we decouple all Higgs (pseudo-)scalars except the SM-like Higgs boson and, in the NMSSM, the light singlet-like scalar and pseudoscalar. Again, we realize this decoupling by setting $m_H = m_A = m_{H^\pm} = 5$ TeV. While these heavy Higgs states can in principle play an important role for dark matter phenomenology [116, 176, 117, 177], their contribution to e.g. the annihilation of light dark matter is suppressed due to the lower bounds on their masses. Regarding the mass of the SM-like Higgs boson, we ensure that $m_{h_{125}} = (125 \pm 3)$ GeV by adjusting the tri-linear coupling A_t [178–184], defined as a component of $\mathbf{A}_u$ in Eq. (3.33). Throughout our analysis, we assume

Observable	Constraint
$\Gamma_{Z\to\chi\chi}$	< 2 MeV [137–145]
$\mathrm{BR}_{h\to inv}$	$< 24\%$ [104, 102, 103]
$m_{\tilde{\chi}_1^\pm}$	> 103.5 GeV [137–145]
$\Omega_\chi h^2$	$0.1187 \pm 20\%$ [49]
σ_{SI}	Xenon1T [69], PandaX [70]
σ_{SD}^p	Pico60 [72]
σ_{SD}^n	LUX [71]

Table 3.4: Constraints on the dark matter sector. From Ref. [126].

$\tan\beta = 10$. Whenever we decouple the wino from the other neutralino states, we set $M_2 = 1$ TeV.

Observables and constraints

Tab. 3.4 lists the constraints on the dark sector we successively include in our analysis.

First, decays of the Z boson to pairs of neutralinos contribute to the invisible Z decay width if they are kinematically allowed. The corresponding partial width reads [185]

$$\Gamma_{Z\to\tilde{\chi}_1^0\tilde{\chi}_1^0} = \frac{m_z}{24\pi}\, g^2_{Z\tilde{\chi}_1^0\tilde{\chi}_1^0}\left(1-\frac{4m^2_{\tilde{\chi}_1^0}}{m_Z^2}\right)^{3/2}, \tag{3.94}$$

for $m_{\tilde{\chi}_1^0} \leq m_Z/2$ and with $g_{Z\tilde{\chi}_1^0\tilde{\chi}_1^0}$ as in Eq. (3.73). As listed in Tab. 3.4, we impose an upper limit of 2 MeV [137–145] on the neutralino contribution to the invisible Z-width.

Analogously, sufficiently light neutralinos contribute to the invisible branching ratio of the Higgs. The partial width of the decay $h \to \tilde{\chi}_1^0\tilde{\chi}_1^0$ is given by [185]

$$\Gamma_{h\to\tilde{\chi}_1^0\tilde{\chi}_1^0} = \frac{m_h}{16\pi}\, g^2_{h\tilde{\chi}_1^0\tilde{\chi}_1^0}\left(1-\frac{4m^2_{\tilde{\chi}_1^0}}{m_Z^2}\right)^{3/2}, \tag{3.95}$$

for $m_{\tilde{\chi}_1^0} \leq m_h/2$ and with $g_{h\tilde{\chi}_1^0\tilde{\chi}_1^0}$ as in Eq. (3.74). Apart from decays to neutralinos, in the NMSSM, there is an additional contribution to $\mathrm{BR}_{h\to inv}$ from decays of the SM-like Higgs to light singlet (pseudo-)scalars which in turn decay invisibly. We impose the currently strongest experimental upper limit of $\mathrm{BR}_{h\to inv} < 24\%$ from CMS [105].

Furthermore, LEP places constraints on charge particles decaying to leptons, photons, jets, or missing energy [137–145]. As described above, we assume all charged scalars to be decoupled with masses of 5 TeV. Hence, in our analysis, mass limits from LEP are only relevant for charginos. We impose a conservative lower bound of $m_{\tilde{\chi}_1^\pm} < 103.5$ GeV on the mass of the lightest chargino.

When we impose the relic density as a constraint, we consider a window of 20% around the measured value of $\Omega_\chi h^2 = 0.1187 \pm 0.002$ [49]. Note that a narrower window would not make a difference to our discussion.

Of course, any particular DM candidate might only comprise part of the relic density and, conversely, additional mediators or co-annihilation partners may reduce the relic density if the result is too large. Furthermore, there may be deviations from the standard thermal production mechanism. Nevertheless, we stress that the correct relic density is an important constraint for a global dark matter interpretation.

Finally, we include the current best limits on neutralino-nucleon scattering from direct detection experiments. For spin-independent scattering, these have been obtained by the Xenon1T experiment [69]. For spin-dependent interactions with protons and neutrons, the best bounds are currently provided by Pico60 [72] and LUX [71], respectively.

4 Final state decays in the MSSM

The research presented in this chapter has been previously published in Ref. [126]. All plots and large parts of the text of this chapter are identical to Sec. 4, "Final state decays in the MSSM", in that article.

To estimate the power of mono-X analysis from final state decays we need a dark matter model with several particles, where the heavier states have an enhanced production rate at the LHC. Supersymmetric winos and higgsinos are obvious and established candidates for such searches. While for example the bino fraction allows us to explain the relic density with a light neutralino, the winos and higgsinos couple strongly to our SM mediators, cf. Sec. 3.2. We will discuss such signatures first for the MSSM, where we have to negotiate a large LHC rate with the relic density and direct detection constraints. Ignoring these constraints would allow us to quote much large LHC rates, but we feel that this would mean taking the experimentalists for a ride. Because the main change in the NMSSM electroweakino sector is a new mediator, we can use this extension to estimate an increased LHC reach from non-SM mediators.

4.1 Mono-Z

In the MSSM framework, mono-Z production is defined as the hard process

$$pp \to \tilde{\chi}_1^0 \tilde{\chi}_1^0 \, Z \; . \tag{4.1}$$

As long as we decouple the sfermions and heavy Higgs bosons, the diagrams shown in Fig. 4.1 are the only diagrams contributing to this process at tree level. This means we can separate three distinct topologies

$$\begin{aligned} & pp \to ZZ \to Z \, (\tilde{\chi}_1^0 \tilde{\chi}_1^0) && \text{ISR} \\ & pp \to Zh \to Z \, (\tilde{\chi}_1^0 \tilde{\chi}_1^0) && \text{invisible Higgs decays} \\ & pp \to \tilde{\chi}_j^0 \tilde{\chi}_1^0 \to (\tilde{\chi}_1^0 Z) \, \tilde{\chi}_1^0 && \text{heavy neutralinos } j = 2,3,4 \; . \end{aligned} \tag{4.2}$$

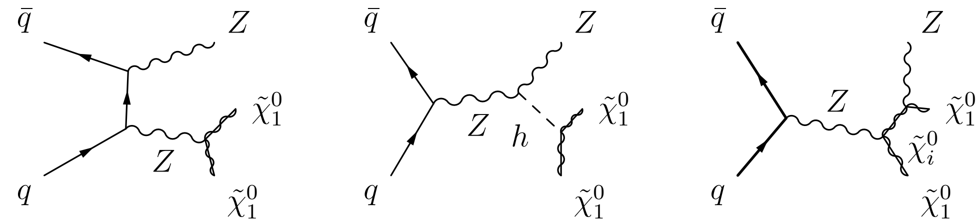

Figure 4.1: Feynman diagrams contributing to mono-Z production in the MSSM, including initial-state Z-radiation with a Z-portal, Zh production with a SM-like Higgs portal, and heavy neutralino decays.

To avoid issues with gauge invariance we always include all topologies in our simulation. If kinematically allowed, intermediate on-shell states lead to a significant enhancement of the LHC production rate in all three cases.

The first two topologies gain impact when the neutralinos are lighter than 45 GeV or 62 GeV. Because of the LEP limits on charginos, this implies that the dark matter agent cannot be a wino or a higgsino and instead requires a sizable bino admixture. Based on the couplings discussed in Sec. 3.2, invisible Z-decays require a large higgsino fraction, leading us to focus on bino–higgsino dark matter. Similarly, invisible SM-like Higgs decays [186–192] require gaugino–higgsino mixing, or in our case also bino–higgsino dark matter.

For the third topology with its intermediate heavy neutralinos the production process requires a sizable higgsino content in both of the neutralinos involved. The decay $\tilde{\chi}_j^0 \to Z\tilde{\chi}_1^0$ is mediated by the same coupling, giving

$$\sigma_{\tilde{\chi}_1^0\tilde{\chi}_1^0 Z} \propto \frac{g^4_{Z\tilde{\chi}_1^0\tilde{\chi}_j^0}}{\Gamma_{\tilde{\chi}_j^0}} \; . \tag{4.3}$$

It is then crucial that the mass difference between the two relevant neutralinos is large, $m_{\tilde{\chi}_j^0} - m_{\tilde{\chi}_1^0} > m_Z$. For dominantly higgsino dark matter with $m_Z \ll |\mu \pm M_1|, |\mu \pm M_2|$ we can approximate [193, 129]

$$\begin{aligned} m_{\tilde{\chi}_{1,2}^0} &= |\mu| + \frac{m_Z^2(1 \pm s_{2\beta})(\mu \mp M_1 c_w^2 \pm M_2 s_w^2)}{2(\mu \mp M_1)(\mu \mp M_2)} \\ m_{\tilde{\chi}_2^0} - m_{\tilde{\chi}_1^0} &= m_Z \left(\frac{m_Z}{M_2} c_w^2 + \frac{m_Z}{M_1} s_w^2 \right) \; . \end{aligned} \tag{4.4}$$

This mass difference is always smaller than m_Z [31, 32, 194], again indicating that higgsinos alone will not lead to a large mono-Z signal. The obvious solution is to again add a sizable bino content to the dark matter candidate and analyze all three topologies in the limit

$$M_1 < |\mu| \ll M_2 \; , \tag{4.5}$$

with three propagating neutralinos.

In the left panel of Fig. 4.2 we show the combined LHC production and decay rate for all three mono-Z topologies in the $\mu - M_1$ plane. The dominant contribution to the sizable rate slightly below the pb range comes from on-shell heavy neutralinos. In the absence of all constraints, the slight asymmetry in the sign of μ comes from the decay threshold as a function of μ and M_1. Limits from invisible Z-decays constrain small M_1 values through the dark matter mass and small $|\mu|$ through the higgsino fraction. In contrast, invisible decays of the SM-like Higgs require a large bino–higgsino mixing and are therefore sensitive to the relative sign of N_{13} and N_{14} in Eq.(3.56). This leads to a cancellation and hence weaker constraints for $\mu < 0$.

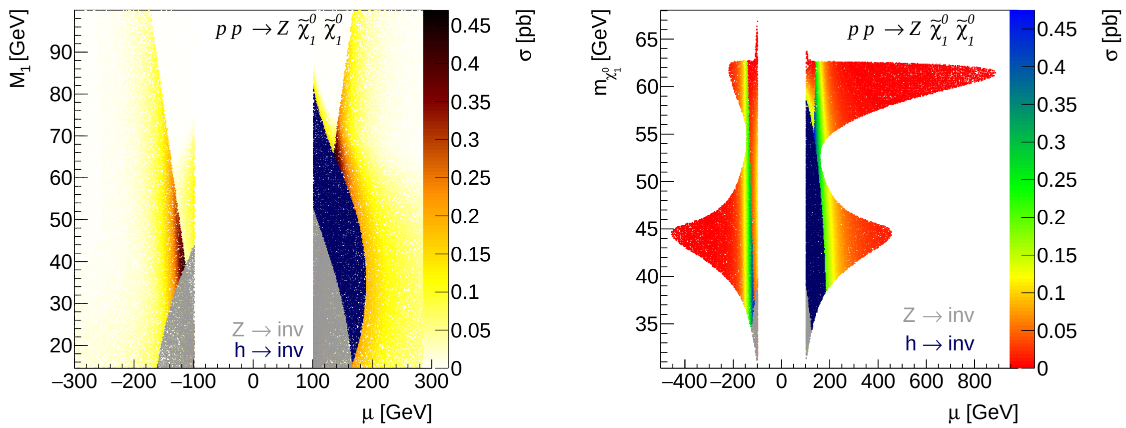

Figure 4.2: Cross section profiles for the mono-Z process in the $\mu - M_1$ plane. All points fulfill the chargino mass bound (left) and, in addition, predict at most the measured relic density (right). Regions excluded by invisible Z and Higgs decays are shown in light gray and dark blue.

As explained Sec. 2.3 and Sec. 3.6, in any realistic thermal dark matter model the observed relic density is a major constraint. Even the weaker assumption that a given dark matter candidate only contributes a fraction of the observed relic density translates into a relevant lower limit on the dark matter annihilation rate. In the right panel of Fig. 4.2 we show the allowed parameter space in terms of the dark matter mass $m_{\tilde{\chi}_1^0}$ and μ. The general feature is that for a given dark matter mass the relic density defines minimum coupling strengths for bino–higgsino dark matter, translated into maximum values of μ. The Higgs poles are highly asymmetric with respect to the sign of μ, while the Z poles are approximately symmetric, as already seen in Fig. 3.2. Because of the on-shell enhancement of the annihilation rate, the invisible decay constraints do not significantly constrain these parameter regions. Other annihilation channels would appear for example for heavier dark matter, but since we are interested in large LHC production rates we limit ourselves to $m_{\tilde{\chi}_1^0} <$ 70 GeV at this stage.

In the upper left panel of Fig. 4.3 we start with all parameter points in agreement with the observed relic density. The curve is identical to the shape shown in Fig. 4.2. The important result is that for the Z and Higgs funnels the higgsino fractions are relatively small, leading to mono-Z rates around 10 fb at the LHC. Larger LHC rates up to 350 fb are possible, but in regions where the dark matter annihilation is not enhanced by on-shell diagrams.

When we include the exact relic density constraint, we should also consider the DD limits described in Sec. 3.6. As explained in Sec. 3.5, the limits translate into limits on the $g_{Z\tilde{\chi}_1^0\tilde{\chi}_1^0}$ and $g_{h\tilde{\chi}_1^0\tilde{\chi}_1^0}$ couplings, competitive with the full range of the on-shell peaks in Fig. 4.2. In the remaining three panels of Fig. 4.3 we show all parameter points predicting the observed relic density and indicate if they agree with the current DD constraints.

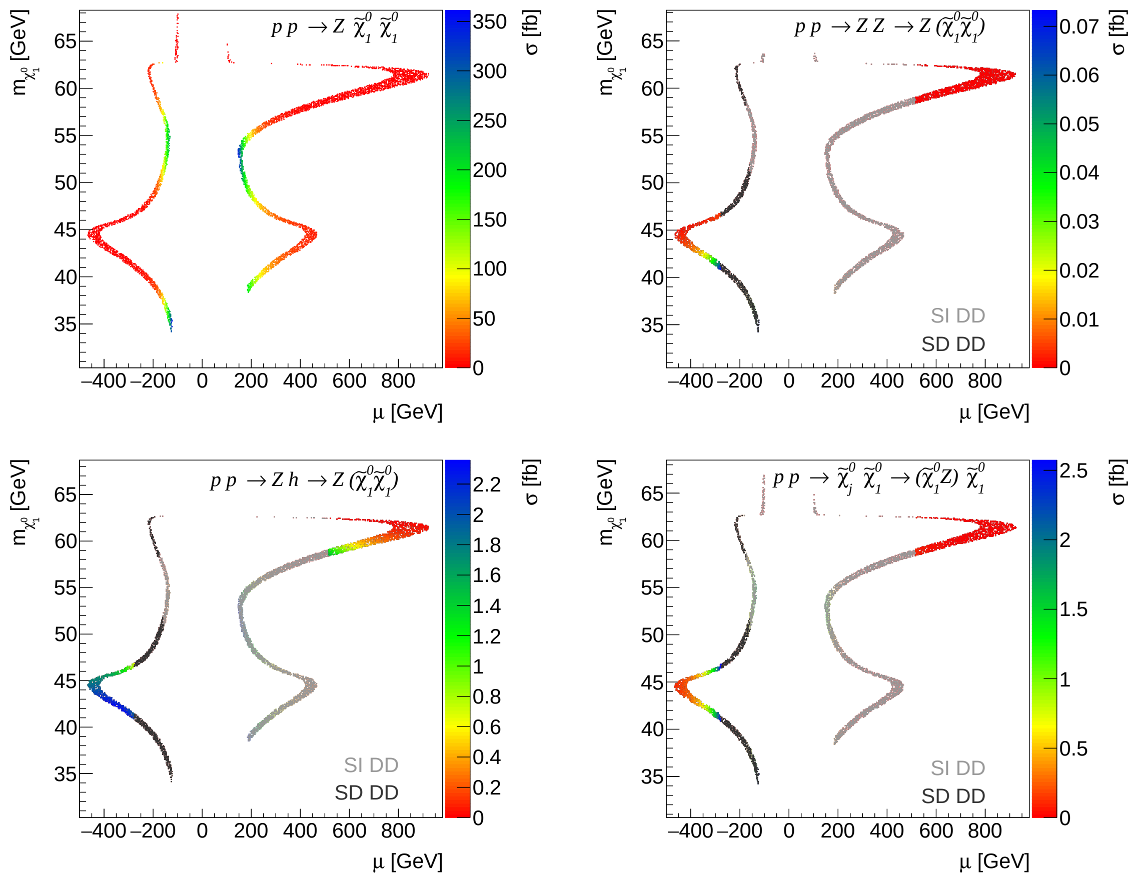

Figure 4.3: Mono-Z cross sections in agreement with the observed relic density (upper left). For the three LHC topologies we also show the combination with DD limits (upper right to lower right). Points excluded by spin-independent DD limits are light gray, points excluded by spin-dependent direct detection in dark gray.

The upper right panel of Fig. 4.3 shows the results for the ISR topology. First, we observe some general features from the interplay of the relic density constraint with spin-independent and spin-dependent direct detection. Just like the shape of the Higgs pole annihilation, the spin-independent constraints are very asymmetric in the sign of μ. This reflects the mixed bino–higgsino coupling to the Higgs with a relative sign between N_{13} and N_{14}. Large preferred values of $\mu > 0$ imply small $g_{h\tilde{\chi}_1^0\tilde{\chi}_1^0}$ and correspond to the usual peak in the allowed parameter space. This peak is not (yet) ruled out by direct detection. For $\mu < 0$ the spin-independent DD constraints are weak, so the leading constraints are spin-dependent limits. Even for $m_{\tilde{\chi}_1^0} \approx m_h/2$ they are driven by $g_{Z\tilde{\chi}_1^0\tilde{\chi}_1^0}$.

As expected from our general ISR discussion in Sec. 2.4, the expected LHC mono-Z rates are very small. They reach 0.07 fb at most, and in a very small region of parameter space around $m_{\tilde{\chi}_1^0} \approx 42$ GeV. This is the only region of parameter space

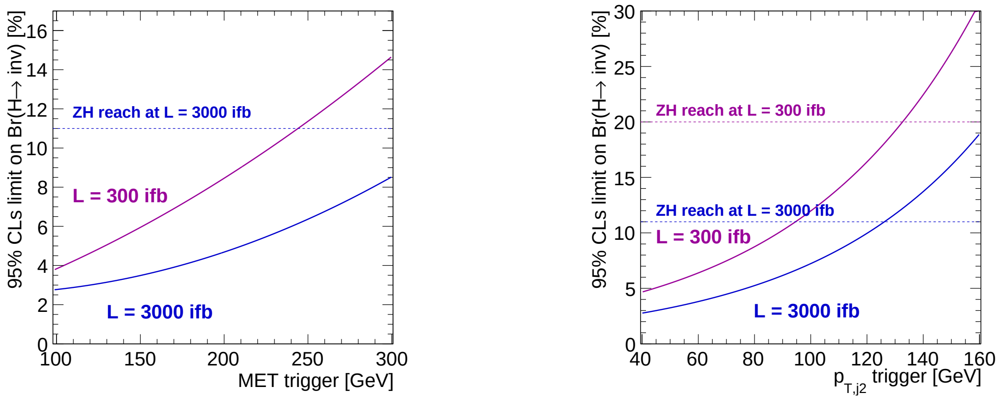

Figure 4.4: CLs limits on invisible Higgs decays from weak boson fusion, as a function of trigger cuts on missing transverse energy (left) or the transverse momentum of the tagging jets (right), compared to the expected reach in the leptonic Zh channel. Figures from Ref [195].

where the LHC process is still enhanced by an on-shell Z-decay, but the couplings are not ruled out spin-dependent direct detection.

The next, lower left panel shows the same information for the Zh topology combined with invisible Higgs decays. The structure is similar to ISR case, but with significantly large cross sections. The reason are the limits from invisible Z and Higgs decays, which following Sec. 3.6 look similar in terms of the partial width, but very different in terms of invisible branching ratios. The latter are relevant for the different $(2 \to 2)$ mono-Z channels. Driven by the relic density constraint the largest rate for the Zh topology of around 2 fb appears for $m_{\tilde{\chi}_1^0} \approx 41$ GeV. The large Higgs couplings are barely allowed by DD constraints.

We can skip a dedicated analysis of mono-Z production in the Zh topology and instead resort to the literature [196–200]: the problem is that we can search for exactly the same model using invisible Higgs decays in weak boson fusion [201, 195]. In Fig. 4.4 we show the results from Ref. [195] which indicate that even with conservative assumptions on triggering at the high-luminosity LHC the Zh topology will never be the discovery channel for such dark matter models.

Finally, we show the expected rates for on-shell neutralinos in the lower right panel. Typical mono-Z rates can reach 2.5 fb for light dark matter, $m_{\tilde{\chi}_1^0} = 40 \ldots 47$ GeV. This window is given by the relic density requirement, where annihilation off the Z-pole is preferred because of the larger corresponding couplings. While the rate for this topology does not reach the invisible Higgs rates, this channel generally extends to larger dark matter masses. The limiting factor is the lower limits on the heavier two higgsino masses and the corresponding LHC production cross sections through an s-channel Z.

While we are not arguing that ATLAS and CMS should not perform mono-Z

searches, we have seen that any interpretation of such a signal as dark matter is likely to require a modification of the standard thermal freeze-out cosmology. In large parts of the allowed parameter space, the dominant mono-Z topology in the MSSM, after taking into account all constraints, is invisible Higgs decays. Those are best searched for in weak-boson-fusion production [201, 195], while mono-Z production can only confirm the invisible Higgs measurement and add at most very little new information. So there goes the glory of mono-Z.

4.2 Mono-W(-pairs)

Mono-W production is defined through the hard process

$$pp \to \tilde{\chi}_1^0 \tilde{\chi}_1^0 \, W^\pm \; . \tag{4.6}$$

The relevant MSSM diagrams contributing to this process are shown as the first three diagrams in Fig. 4.5. Like for mono-Z production, we can distinguish three topologies,

$$\begin{aligned}
&pp \to W^\pm Z \to W^\pm \, (\tilde{\chi}_1^0 \tilde{\chi}_1^0) && \text{ISR} \\
&pp \to W^\pm h \to W^\pm \, (\tilde{\chi}_1^0 \tilde{\chi}_1^0) && \text{invisible Higgs decays} \\
&pp \to \tilde{\chi}_j^\pm \tilde{\chi}_1^0 \to (\tilde{\chi}_1^0 W^\pm) \, \tilde{\chi}_1^0 && \text{heavy charginos } j = 1, 2 \; .
\end{aligned} \tag{4.7}$$

The first two rely on the same dark matter couplings as their mono-Z counterparts and only differ in the production process of the SM-like mediators. Therefore, we will again focus on bino-higgsino dark matter for the ISR and invisible Higgs topologies.

Also in analogy to mono-Z production, a third topology features heavy states from the dark matter sector decaying into dark matter and a weak boson. The heavy state is one of the two charginos with the decay $\tilde{\chi}_j^\pm \to W \tilde{\chi}_1^0$. Again, production and decay are mediated by the same coupling,

$$\sigma_{\tilde{\chi}_1^0 \tilde{\chi}_1^0 W} \propto \frac{g^4_{W \tilde{\chi}_1^0 \tilde{\chi}_j^\pm}}{\Gamma_{\tilde{\chi}_j^\pm}} \; . \tag{4.8}$$

The coupling $g_{W \tilde{\chi}_1^0 \tilde{\chi}_j^\pm}$ is in part a higgsino-higgsino coupling, which following Sec. 4.1 leads us to consider bino-higgsino dark matter. In addition, $g_{W \tilde{\chi}_1^0 \tilde{\chi}_j^\pm}$ includes a

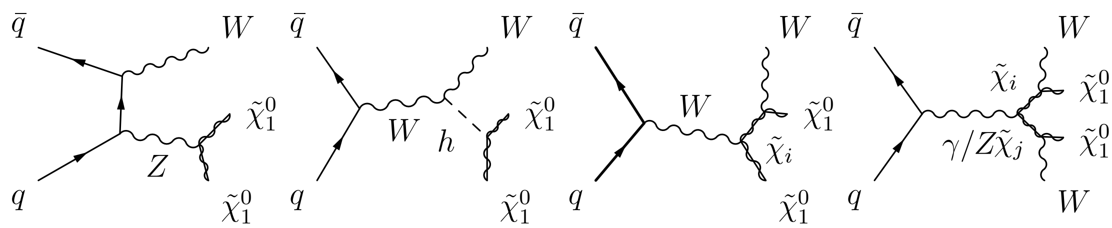

Figure 4.5: Feynman diagrams contributing to mono-W production in the MSSM, including initial-state W-radiation with a Z-portal, Wh production with a SM-like Higgs portal, chargino decays, and W-pair production.

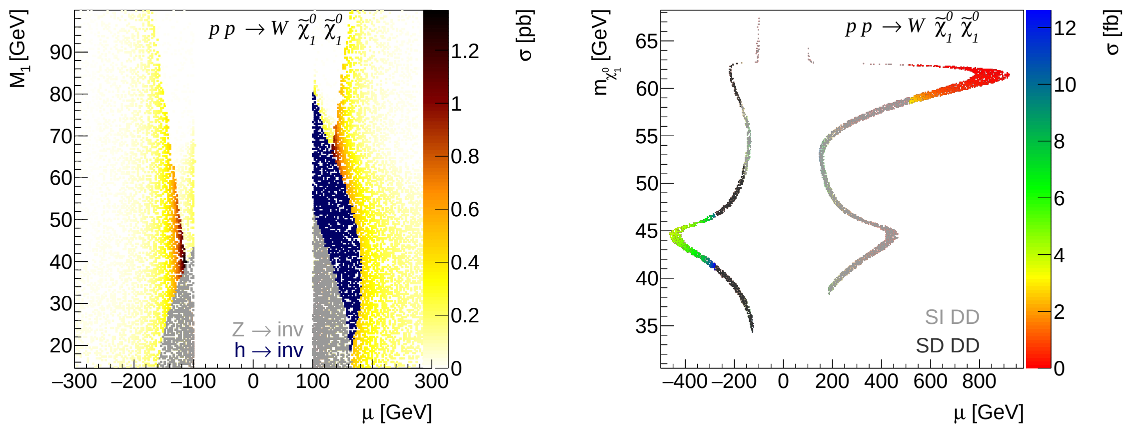

Figure 4.6: Cross section for the mono-W process in the $\mu - M_1$ plane. Left: points fulfilling the chargino mass bound, shown with the limits on invisible Z and Higgs decays. Right: points also predicting the correct relic density, shown with DD bounds.

wino-wino interaction, cf. Eq. (3.57). However, bino-wino dark matter is difficult to reconcile with LEP bounds in the absence of explicit bino-wino mixing in the neutralino mass matrix. Therefore, all three mono-W topologies again lead us to focus on bino-higgsino dark matter with

$$M_1 < |\mu| \ll M_2 \,, \tag{4.9}$$

just like for the mono-Z analysis in Sec. 4.1.

In the left panel of Fig. 4.6 we show the mono-W rate in the $\mu - M_1$ plane. Like in Fig. 4.2 we again include the limits on invisible decays. The largest rates lie in the pb range and stem from the chargino-decay topology. They are two to three times as large as the largest mono-Z rates passing the same constraints. This is due partly to the combination of mono-W^+ and mono-W^- production, and partly to the relevant Z and W couplings.

In the right panel of Fig. 4.6 we show the points in agreement with the observed relic density. In addition, we indicate spin-independent and spin-dependent DD limits. Since the mono-W topologies rely on the same type of dark matter couplings as mono-Z production, the constraints work the same way as in Sec. 4.1: ISR rates become negligible, while rates from chargino decays are suppressed by the large (charged) higgsino masses required by direct detection. The largest LHC rates are again found in a narrow window around the Z-pole annihilation funnel. The only difference is that typically mono-W rates are roughly twice as large as mono-Z rates.

A major constraint on mono-Z and mono-W rates at the LHC are DD limits. Both, spin-independent and spin-dependent DD limits impose a strong upper bound

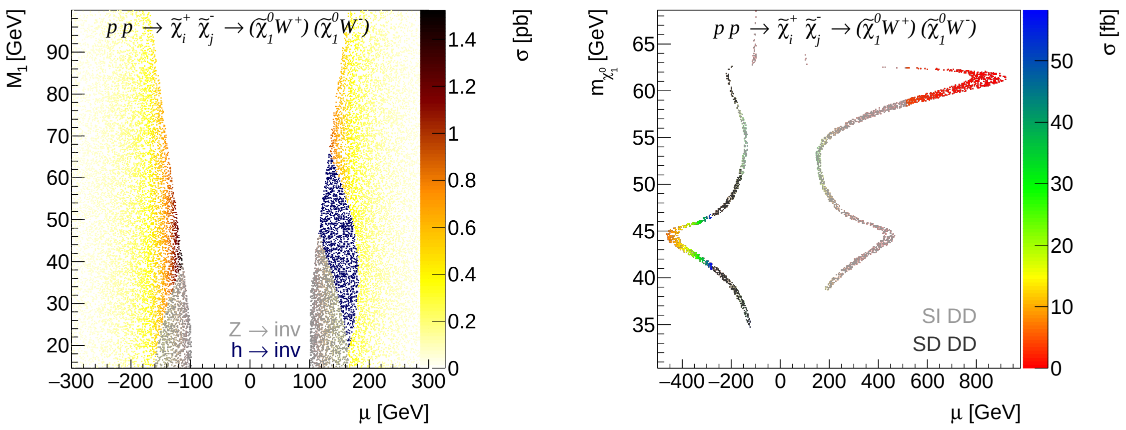

Figure 4.7: Cross section for the mono-W-pair process in the $\mu - M_1$ plane in analogy to Fig. 4.6. Left: points fulfilling the chargino mass bound, shown with the limits on invisible Z and Higgs decays. Right: points also predicting the correct relic density, shown with DD bounds.

on the higgsino admixture in the dark matter candidate through the $g_{Z\tilde{\chi}_1^0\tilde{\chi}_1^0}$ and $g_{h\tilde{\chi}_1^0\tilde{\chi}_1^0}$ couplings. We can try to circumvent them through an LHC production process which survives the limit $N_{13}, N_{14} \to 0$. This happens for mono-W-pair production

$$pp \to \tilde{\chi}_i^+ \tilde{\chi}_j^- \to (\tilde{\chi}_1^0 W^+)\,(\tilde{\chi}_1^0 W^-) \qquad \text{with } i,j = 1,2\,, \tag{4.10}$$

shown in the right diagram of Fig. 4.5. The rate for chargino pair production through an s-channel photon is strongly enhanced compared to purely weak mono-W production. It does not have a counterpart in mono-Z production. Furthermore, even for small couplings we can assume

$$\text{BR}\left(\tilde{\chi}_1^\pm \to W^\pm \tilde{\chi}_1^0\right) \approx 1\,, \tag{4.11}$$

since it is the only kinematically allowed two-particle decay mode at tree level. We show the rates for mono-W-pair production in Fig. 4.7. Before taking into account DD constraints, the rates for mono-W and mono-W-pair production are similar. Since the actual couplings are not constrained by direct detection, the maximum rates remain larger than for mono-W production. However, we find that the spin-dependent DD bound on the neutral higgsino, $|\mu| \gtrsim 250$ GeV leads to a kinematic suppression of the $\tilde{\chi}_j^- \tilde{\chi}_j^+$ production rate.

Our mono-W study implies that in contrast to, for instance, effective theory arguments, intermediate on-shell states prefer mono-W production over mono-Z production. One of the mechanisms behind this is the mono-W-pair topology. Its contributions are removed, if we employ jet or lepton vetoes to remove top backgrounds for the mono-W signal. Again, there is no point in performing a detailed signal-background analysis of this channel, because chargino pair production is a bread-and-butter signature for electroweakinos at the LHC [202, 203].

4.3 Mono-Higgs(-pairs)

Mono-Higgs production is the third electroweak process we consider in our comprehensive study of final state decay leading to mono-X signatures. The hard process reads

$$pp \to \tilde{\chi}_1^0 \tilde{\chi}_1^0 h \; . \tag{4.12}$$

The Higgs boson in the final state is the SM-like light scalar of the MSSM. The Feynman diagrams shown in Fig. 4.8 define two mono-Higgs topologies

$$\begin{aligned} & pp \to hZ \to h\,(\tilde{\chi}_1^0 \tilde{\chi}_1^0) && \text{invisible } Z\text{-decays} \\ & pp \to \tilde{\chi}_j^0 \tilde{\chi}_1^0 \to (\tilde{\chi}_1^0 h)\,\tilde{\chi}_1^0 && \text{heavy neutralinos } j = 2,3,4 \; . \end{aligned}$$

Obviously, the usual ISR topology is not relevant for the Higgs case. The Zh topology is based on the same production mechanism as for mono-Z production, but combined with a strongly constrained branching ratio $\text{BR}_{Z \to \chi\chi}$. The two relevant couplings driving the neutralino decay topology are

$$\sigma_{\tilde{\chi}_1^0 \tilde{\chi}_1^0 h} \propto \frac{g^2_{Z \tilde{\chi}_1^0 \tilde{\chi}_i^0} g^2_{h \tilde{\chi}_1^0 \tilde{\chi}_i^0}}{\Gamma_{\tilde{\chi}_i^0}} \; . \tag{4.14}$$

The production process still requires a sizable coupling to the Z, while the decay proceeds through the Higgs coupling. The decay $\tilde{\chi}_i^0 \to \tilde{\chi}_1^0 h$ competes with the decay $\tilde{\chi}_i^0 \to \tilde{\chi}_1^0 Z$. Just like for mono-$Z$ and mono-W production, the observed relic density combined with all available constraints motivates mixed bino-higgsino dark matter,

$$M_1 < |\mu| \ll M_2 \; . \tag{4.15}$$

In the left panel of Fig. 4.9 we show the rates we start with, before considering relic density and DD constraints. We see that the mono-Higgs rates are more than an order of magnitude smaller than their mono-Z or mono-W counterparts shown in Fig. 4.2 and Fig. 4.6. For the Zh topology the limiting factor is the smaller invisible branching ratio of the Z-boson as compared to the invisible Higgs decays, described

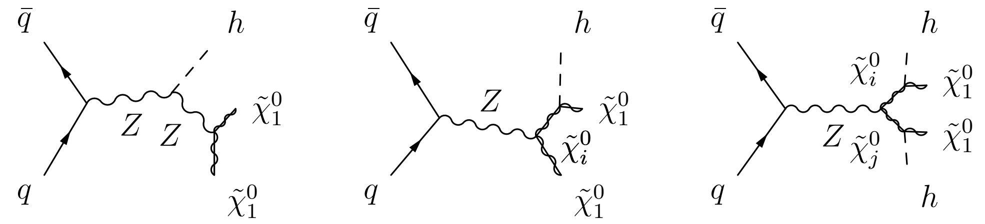

Figure 4.8: Feynman diagrams contributing to mono-Higgs production in the MSSM, Zh production with a Z-portal, and heavy neutralino decays, and Higgs pair production.

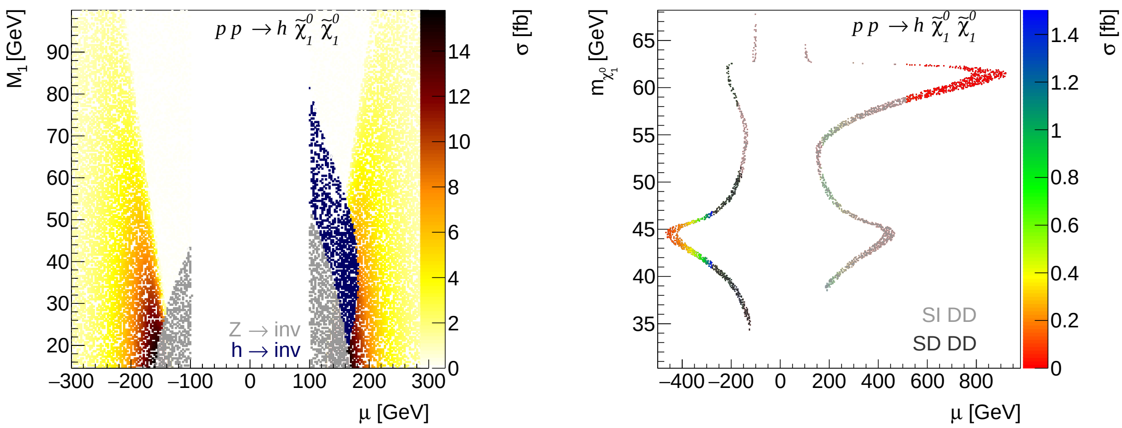

Figure 4.9: Cross section for the mono-Higgs process in the $\mu - M_1$ plane. Left: points fulfilling the chargino mass bound, shown with the limits on invisible Z and Higgs decays. Right: points also predicting the correct relic density, shown with DD bounds.

in Sec. 3.6. The neutralino decay topology predicts smaller rates because especially for large production rates and before considering DD limits the competing decay rate $\tilde{\chi}^0_{2,3} \to \tilde{\chi}^0_1 Z$ is large.

In the right panel of Fig. 4.9 we see the effect of the spin-dependent and spin-independent DD limits. The Zh topology is now suppressed to unobservable LHC rates through the invisible Z branching ratio, just like the ISR topology of the mono-Z signature described in Sec. 4.1. Unlike for the mono-Z case, the neutralino decay topology becomes the leading channel with possible LHC rates in the range of 1 fb. The predicted mono-Higgs rate after taking into account DD constraints is indeed not much smaller than the expected mono-Z rates from neutralino decay.

Inspired by the mono-W case, it turns out that one way out of some of the leading constraints is mono-Higgs-pair production shown in the right panel of Fig. 4.8,

$$pp \to \tilde{\chi}^0_i \tilde{\chi}^0_j \to (\tilde{\chi}^0_1 h)\,(\tilde{\chi}^0_1 h) \qquad \text{with } i,j = 2,3,4\,. \tag{4.16}$$

The neutralino production couplings are now separated from the decay couplings and, more importantly, from the couplings mediating direct detection,

$$\sigma_{\tilde{\chi}^0_1\tilde{\chi}^0_1 hh} \propto \frac{g^2_{Z\tilde{\chi}^0_i\tilde{\chi}^0_j}\, g^2_{h\tilde{\chi}^0_1\tilde{\chi}^0_i}\, g^2_{h\tilde{\chi}^0_1\tilde{\chi}^0_j}}{\Gamma_{\tilde{\chi}^0_i}\Gamma_{\tilde{\chi}^0_j}}\,. \tag{4.17}$$

In our preferred scenario with bino-higgsino dark matter and another, relatively light higgsino the production of heavy neutralino pairs will be sizable. At the same time, the decay to Higgs bosons requires a gaugino content just like the annihilation responsible for the correct relic density.

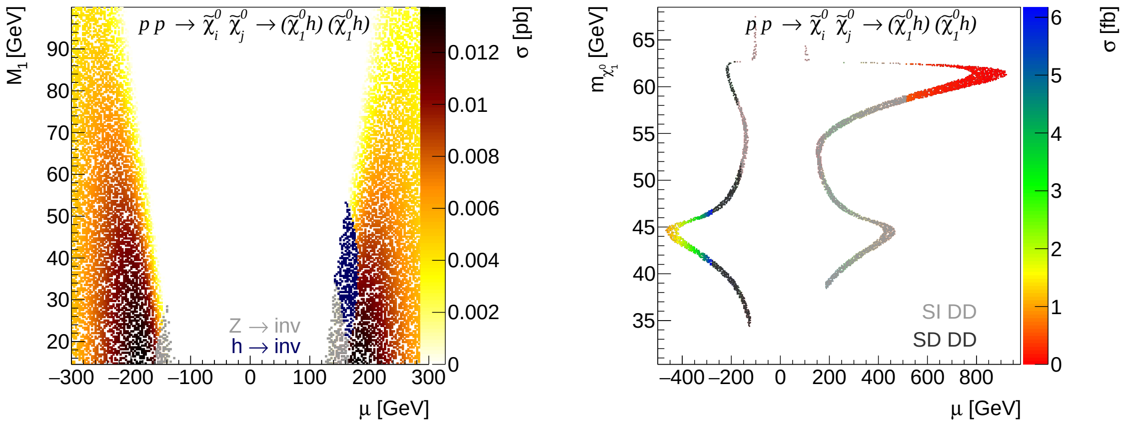

Figure 4.10: Cross section for the mono-Higgs-pair process in the $\mu - M_1$ plane. Left: points fulfilling the chargino mass bound, shown with the limits on invisible Z and Higgs decays. Right: points also predicting the correct relic density, shown with DD bounds.

We show the LHC rates for the mono-Higgs-pair signature in Fig. 4.10. First, the mono-Higgs-pair cross section is suppressed by the phase space of two heavy higgsinos in the final state with $|\mu| \gtrsim 300 \ldots 400$ GeV, just like the mono-W-pair rate. This is why the rate before applying any constraints is in the same range as the mono-Higgs rate. On the other hand, every coupling contributing to the LHC rate is unrelated to direct detection. Through a large bino fraction of the dark matter agent we can essentially decouple the DD constraints, so the LHC rates with and without relic density and DD constraints are very similar. All we need to do is enhance the annihilation rate in the early universe through an on-shell condition $m_{\tilde{\chi}_1^0} \approx M_1 \approx m_Z/2$ or $m_{\tilde{\chi}_1^0} \approx M_1 \approx m_h/2$.

The LHC signature of mono-Higgs-pair production is similar to Higgs pair production at the LHC. While the expected production rate for a pair of SM-like Higgs bosons is around 35 fb, the additional missing energy in the mono-Higgs-pair signal of Eq.(4.16) should allow for a better background rejection. Which decay combination of the two Higgs bosons works best for this purpose is currently under study [204]. For SM-like Higgs pairs the combination $b\bar{b}\,\gamma\gamma$ works best to guarantee detection and reduce backgrounds, but for the smaller dark matter signal the combinations $b\bar{b}\,b\bar{b}\,\not{E}_T$ or $b\bar{b}\,WW\,\not{E}_T$ might be more promising.

Finally, for completeness and in analogy to mono-W pairs and mono-Higgs pairs, we consider the mono-Wh pair process given by

$$pp \to \tilde{\chi}_i^\pm \tilde{\chi}_j^0 \to (\tilde{\chi}_1^0 W^\pm)\,(\tilde{\chi}_1^0 h) \qquad \text{with } i = 1,2 \text{ and } j = 2,3,4\;. \tag{4.18}$$

This topology is driven by the production coupling $g_{W\tilde{\chi}_j^0\tilde{\chi}_i^\pm}$ and, for the decay, $g_{W\tilde{\chi}_1^0\tilde{\chi}_i^\pm}$

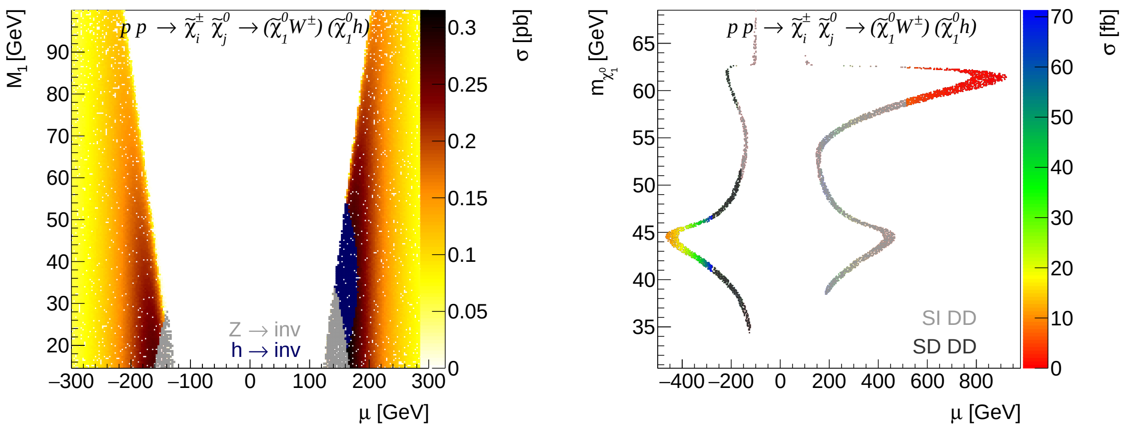

Figure 4.11: Cross section for the mono-Wh-pair process in the $\mu - M_1$ plane. Left: points fulfilling the chargino mass bound, shown with the limits on invisible Z and Higgs decays. Right: points also predicting the correct relic density, shown with DD bounds.

and $g_{h\tilde{\chi}_1^0\tilde{\chi}_j^0}$,

$$\sigma_{\tilde{\chi}_1^0\tilde{\chi}_1^0 Wh} \propto \frac{g^2_{W\tilde{\chi}_j^0\tilde{\chi}_i^\pm}\, g^2_{W\tilde{\chi}_1^0\tilde{\chi}_i^\pm}\, g^2_{h\tilde{\chi}_1^0\tilde{\chi}_j^0}}{\Gamma_{\tilde{\chi}_i^\pm}\Gamma_{\tilde{\chi}_j^0}} \; . \tag{4.19}$$

In the scenario of a bino-higgsino LSP, heavier higgsinos and a decoupled wino, the production cross section for a heavy chargino-neutralino pair will be sizable. Like in the mono-W(-pair) process, we again have

$$\text{BR}\left(\tilde{\chi}_1^\pm \to W^\pm \tilde{\chi}_1^0\right) \approx 1 \; . \tag{4.20}$$

On the other hand, the decay $\tilde{\chi}_j^0 \to \tilde{\chi}_1^0 h$ of the heavy neutralino, requiring gaugino and higgsino parts in the LSP, competes with the decay $\tilde{\chi}_j^0 \to \tilde{\chi}_1^0 h$.

Hence, rates before relic density and direct detection constraints, shown in the left panel of Fig. 4.11, lie between the rates for mono-Higgs pairs and those for mono-W pairs. Like for mono-W pairs and mono-Higgs pairs, production couplings and decays are decoupled from direct detection. The correct relic density can be guaranteed through the resonant enhancement at $m_{\tilde{\chi}_1^0} \approx M_1 \approx m_Z/2$ or $m_{\tilde{\chi}_1^0} \approx M_1 \approx m_h/2$. Hence, the mono-$Wh$-pair cross section is only suppressed kinematically through the production of heavy higgsinos. The resulting rates are shown in the right panel of Fig. 4.11. We find cross sections of up to 70 fb, slightly above the mono-W-pair rate. We do not perform a signal-background analysis, since neutralino-chargino pairs belong to the electroweakino signatures already being studied at the LHC [205].

5 Final state decays beyond the MSSM

The research presented in this chapter has been previously published in Ref. [126]. All plots and large parts of the text of this chapter are identical to Sec. 5, "Final state decays beyond the MSSM", in that article.

The leading constraint on the size of electroweak mono-X signals in the MSSM comes from direct detection or, more specifically, from the combination of the relic density constraint and the DD limits. The reason is that we need large couplings to the Z and SM-like Higgs mediators to reach the observed relic density, direct detection strongly constrains these couplings, and most LHC rates again rely on the same couplings. In extended models like the NMSSM a dark sector mediator is responsible for the correct relic density, in spite of very small couplings to the Standard Model. From our mono-W(-pair) and mono-Higgs(-pair) we know how to decouple the decay topologies at the LHC from the DD constraints, which motivates our NMSSM study.

Following Sec. 3.3 we adjust the singlet–singlino dark matter sector such that a light singlino with $m_{\tilde{\chi}_1^0} = 10$ GeV can annihilate to the correct relic density through an on-shell singlet. Because this annihilation relies on the couplings within the singlet–singlino sector we can decouple the gaugino masses in our $|\mu| \ll M_1 = M_2 = 1$ TeV. Following Eq. (3.68), we ensure the corresponding mass relation by choosing $\tilde{\kappa}$ such that

$$m_{\tilde{\chi}_1^0} \approx 2\tilde{\kappa}\mu + \frac{m_Z^2}{\mu}\,\tilde{\lambda}^2\,\frac{2\tilde{\kappa} - s_{2\beta}}{4\tilde{\kappa}^2 - 1} = 10 \text{ GeV} . \tag{5.1}$$

If we include the LEP constraints $|\mu| \gtrsim 100$ GeV, this typically implies

$$|\tilde{\kappa}| = \frac{m_{\tilde{\chi}_1^0}}{2|\mu|} \lesssim 0.05 . \tag{5.2}$$

or $|\kappa| \ll |\lambda|$ in the original notation. For our mass hierarchy this means

$$|\tilde{\kappa}\mu| \ll |\mu| \ll M_1 \approx M_2 . \tag{5.3}$$

The singlino couplings from Eq.(3.71) are approximately given by

$$g_{a_s\tilde{\chi}_1^0\tilde{\chi}_1^0} \approx g_{h_s\tilde{\chi}_1^0\tilde{\chi}_1^0} \approx -\sqrt{2}g\,\tilde{\lambda}\tilde{\kappa}\,N_{15}^2 . \tag{5.4}$$

They are not large compared for example to gauge couplings, but sufficiently large to explain the observed relic density for an on-shell annihilation process. The remaining free parameters in the NMSSM electroweakino sector which we vary in our analysis are $\tilde{\kappa}$, $\tilde{\lambda}$ and A_κ.

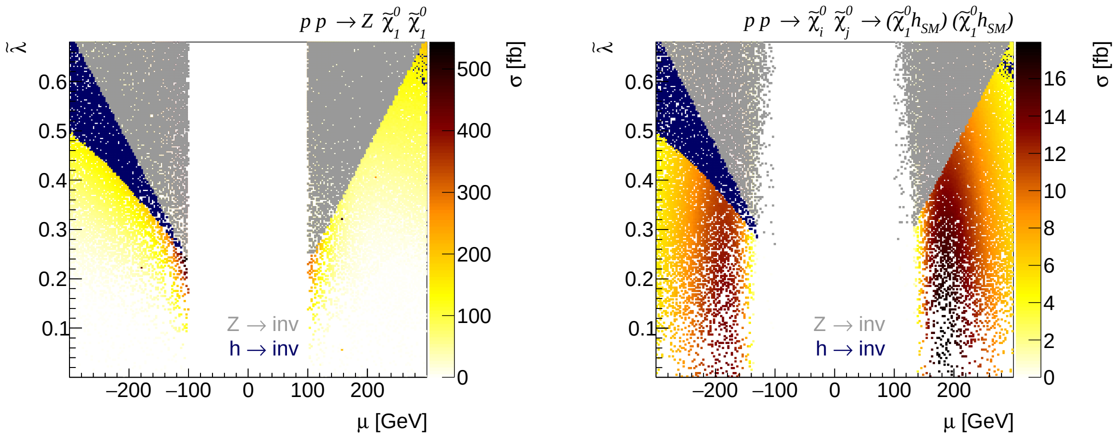

Figure 5.1: Cross section profiles for the mono-Z (left) and mono-Higgs-pair (right) processes in the $\mu - \lambda$ plane. All points fulfill the chargino mass bounds. Regions excluded by invisible Z and Higgs decays are shown in light gray and dark blue.

While it is generally possible to extend all MSSM analyses of Sec. 4 to the NMSSM we focus on the two most interesting cases, the strongly constrained mono-Z signal and the most flexible mono-Higgs-pair signal

$$pp \to \tilde{\chi}_1^0 \tilde{\chi}_1^0 \, Z \qquad \text{and} \qquad pp \to \tilde{\chi}_i^0 \tilde{\chi}_j^0 \to (\tilde{\chi}_1^0 h) \, (\tilde{\chi}_1^0 h) \, . \tag{5.5}$$

For the mono-Z signal the ISR, invisible SM-like Higgs h_{125}, and heavy neutralino topologies shown in Fig. 4.1 are supplemented by the associated Zh_s mediator production.

As usual, we start with the cross sections without the dark matter constraints in Fig. 5.1. Because we fix the dark matter mass to 10 GeV, there is no threshold left to consider. Instead, we show the correlation between the higgsino mass and the singlino–higgsino mixing parameter $\tilde{\lambda}$. In general, the LHC cross section grows with λ, since all contributing diagrams are driven by bino-higgsino mixing, times $\tilde{\lambda}$ connecting the higgsino content to the singlino content. For heavy gaugino masses, the Z and Higgs decay constraints limit the size of the higgsino fraction of the lightest neutralino, or $\tilde{\lambda}$ for a given value of μ. While in the MSSM the invisible Higgs limits were stronger for $\mu > 0$, they now constrain mostly $\mu < 0$. This is because of the sign difference between the singlino–Higgs coupling and the bino-Higgs coupling,

$$g_{h_{125}\tilde{\chi}_1^0\tilde{\chi}_1^0} \approx \begin{cases} g' N_{11} s_\beta \left(-\dfrac{N_{13}}{t_\beta} + N_{14} \right) & \text{bino} \\ -\sqrt{2}\lambda N_{15} \left(N_{13} + \dfrac{N_{14}}{t_\beta} \right) & \text{singlino.} \end{cases} \tag{5.6}$$

The mono-Higgs-pairs rate shown in the right panel of Fig. 5.1 are similar to the NMSSM case shown in Fig. 4.10. As expected from the enhanced flexibility in all couplings, they prefer a small higgsino mass and can exceed the mono-Z rates.

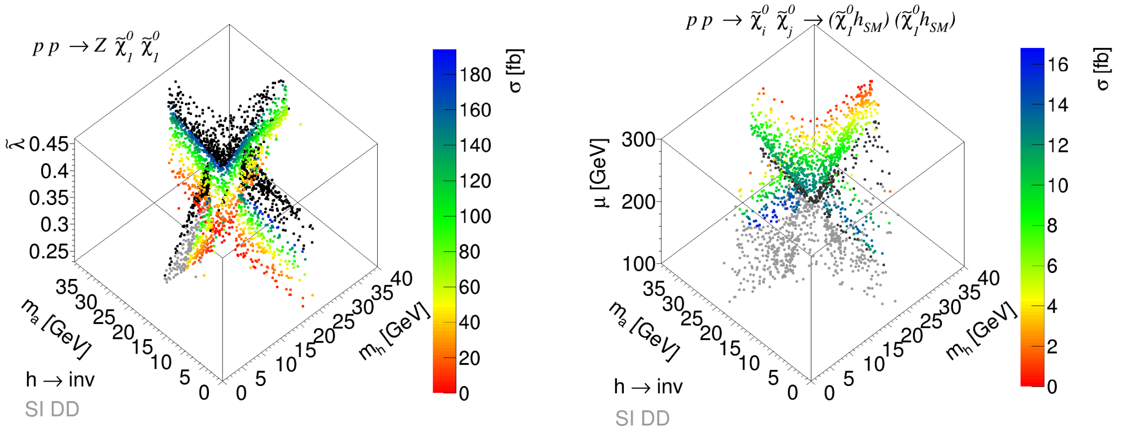

Figure 5.2: Mono-Z (left) and mono-Higgs-pair (right) cross section versus the singlet-like pseudoscalar and scalar masses and the singlino–higgsino mixing parameter. All points fulfill the relic density, chargino mass, and invisible Z decay bounds. The effects of the invisible Higgs decays and spin-independent direct detection are shown in grey.

The interesting question is, how these large LHC rates change when we apply the constraints from the relic density and direct detection. In the left panel of Fig. 5.2 we show the results for mono-Z production in the NMSSM framework. The general pattern confirms that either the scalar or the pseudo-scalar mediator has to be just slightly off its mass shell, with a width given by the velocity distribution. The main difference between them arises from CMB bounds, which are irrelevant for scalar p-wave annihilation, while a 10 GeV neutralino is barely allowed for s-wave annihilation through the pseudoscalar [206, 207]. In addition, following Eq.(5.6) the LHC production rate is roughly proportional to a factor λ from the explicit couplings and another factor $\tilde{\lambda}$ from the higgsino fractions.

After including all constraints, the Zh topology with an invisible Higgs again emerges as the dominant mono-Z process. However, while for the MSSM the direct detection constraints effectively enforce $\text{BR}\,(h_{125} \to \tilde{\chi}_1^0 \tilde{\chi}_1^0) \lesssim 0.003$, they now fall behind the LHC limit of 24%. This way, the LHC rate in the NMSSM can be forty times as large as in the MSSM, exceeding 100 fb. The light, new scalar mediator also leads to spin-independent singlino–nucleon scattering. This manifests itself in the excluded points at low m_{h_S} and large singlino–higgsino mixing λ.

Also in Fig. 5.2 we show the same effects for mono-Higgs-pair production. In that case the relevant third parameter is not the singlino–higgsino mixing, but the higgsino mass parameter. In the NMSSM the LHC rates can be three times as large as in the MSSM. The reason is a kinematic effect, because the weaker DD bounds for smaller dark matter masses allow for a larger higgsino fraction in the dark matter candidate and hence lighter on-shell higgsinos. The subsequent branching ratios for the decays $\tilde{\chi}_{2,3}^0 \to h_{125} \tilde{\chi}_1^0$ are similar to typical MSSM values, namely around 40%.

For constant μ this branching ratio is approximately independent of λ, since both $g_{h\tilde{\chi}_1^0\tilde{\chi}_1^0}$ and $g_{Z\tilde{\chi}_1^0\tilde{\chi}_1^0}$ are proportional to λ^2 from the explicit and implicit dependences.

Altogether, we indeed see how the light NMSSM mediators allow us to decouple the different relic density, direct detection, and LHC observables. Most importantly, our dark matter singlet as well as the heavier higgsinos can now be lighter than in the MSSM. For all channels this directly translates into an increase of the LHC rate by a factor three to forty. The mono-W channel will obviously follow the same pattern.

6 Conclusion

Mono-X processes provide a promising class of signatures for dark matter searches at the LHC. These processes are typically motivated employing EFT frameworks or as initial state radiation in simplified models. In this thesis, we instead focused on mono-X signals from final state decays. Such processes rely on the on-shell production of heavy intermediate particles and are, therefore, clearly not covered by an EFT approach.

We studied mono-Z, mono-W (pair), and mono-Higgs (pair) processes in the MSSM and NMSSM, focusing on how decays involving heavy electroweakinos can structurally lead to large LHC cross sections. In the MSSM, we found that, while large mono-Z rates are initially possible, the combination of relic density and direct detection constraints cuts deeply into the allowed parameter space, reducing LHC expectations. In particular, we found that strong resonant enhancement of the annihilation cross section becomes necessary to reach the observed relic density. Overall, we found that large mono-Z rates at the LHC could not be reconciled with dark matter constraint when only SM mediators were involved. Furthermore, associated Zh production followed by invisible Higgs decay emerged as a leading mono-Z channel. However, this signature is known to be a weaker probe of invisible Higgs decays than weak boson fusion.

For mono-W, we found larger cross sections than for mono-Z, contrary to EFT arguments. Moreover, considering mono-W pairs allowed us to largely decouple annihilation and direct detection from LHC expectations, reducing, in particular, the impact of direct detection limits to a mere kinematic suppression through the masses of intermediate higgsinos. Note that experimentally it needs to be ensured that the pair contribution to mono-W signals is not removed through jet or lepton vetoes.

Mono-Higgs does not appear promising at first. However, we found that one can, again, consider pairs, in order to largely decouple LHC cross sections from dark matter constraints. Hence, including constraints, this allows for larger rates for mono-Higgs pairs than for simple mono-Higgs. A detailed analysis of the mono-Higgs pair signature is currently under study [204]. Furthermore, the mono-Wh process also allows to largely decouple direct detection and relic density from the LHC cross sections, resulting in slightly larger cross sections than mono-W-pairs.

Finally, we examined how the remaining constraints can be alleviated in the dark matter sector of the NMSSM. To this end, we reconsidered mono-Z, which was the most constrained process considered by us in the MSSM, and mono-Higgs pairs, which was the most flexible, in the NMSSM. The additional NMSSM scalar and pseudoscalar mediators allowed for the efficient annihilation of significantly lighter dark matter than in the MSSM. Thus, the annihilation is completely separated from mono-X processes at the LHC, and direct detection can be decoupled more efficiently. Hence, an NMSSM scenario with light singlino dark matter allowed for much larger mono-X cross sections. Furthermore, our conclusions that mono-W appears more promising than mono-Z and that pairs should be included remained valid.

Acknowledgments

First of all, I would like to thank my supervisor Tilman Plehn for coming up with this project and giving me the opportunity to work on it, write a paper on it, and give talks about it. All of that was not only interesting, but also great fun. Thank you also for continually awarding me the “Johann Brehmer prize for smartassery” and for always being a good sport about any remark I made.
I would like to thank Anja Butter for having been my day-to-day supervisor during much of this project. Thank you for letting me in on your knowledge on SUSY dark matter and the tools to deal with it. Whenever I asked if I could talk to you, the response always was “Klar, komm hoch!” Thank you for that!
Special thanks also go to Jan Horak for helping me get started on this project and our collaboration in the first couple of weeks.
Peter, thank you for proofreading this thesis! I owe you one.
I also want to thank Jennie, who I shared an office with the whole time, for endless banter and for her patience whenever I was talking her ear off while she was trying to work.
Last, but definitely not least, I want to thank absolutely everyone in our pheno group for Marstall, ice cream, coffee breaks, and for simply being a fantastic group to be part of.

A Bibliography

[1] F. Zwicky, Helvetica Physica Acta **6**, 110 (1933).

[2] G. Bertone and D. Hooper, Submitted to: Rev. Mod. Phys. (2016), arXiv:1605.04909 [astro-ph.CO].

[3] D. Hooper, arXiv:0901.4090 [hep-ph].

[4] Particle Data Group, M. Tanabashi *et al.*, Phys. Rev. D **98**, 030001 (2018).

[5] S. P. Liew, M. Papucci, A. Vichi, and K. M. Zurek, JHEP **1706**, 082 (2017), arXiv:1612.00219 [hep-ph].

[6] UA1 Collaboration, G. Arnison *et al.*, Phys. Lett. **139B**, 115 (1984).

[7] H. L.J., R. L. Jaffe, and J. Rosner, Snowmass Summer Study 1984:822 .

[8] L. J. Hall and J. Polchinski, Phys. Lett. **152B**, 335 (1985).

[9] O. Nachtmann, A. Reiter, and M. Wirbel, Z. Phys. C **27**, 577 (1985).

[10] P. J. Fox, R. Harnik, J. Kopp, and Y. Tsai, Phys. Rev. D **85**, 056011 (2012), arXiv:1109.4398 [hep-ph].

[11] Y. Gershtein, F. Petriell, S. Quackenbush, and K. M. Zurek, Phys. Rev. D **78**, 095002 (2008), arXiv:0809.2849 [hep-ph].

[12] Y. Bai and T. M. P. Tait, Phys. Lett. B **723**, 384 (2013), arXiv:1208.4361 [hep-ph].

[13] N. F. Bell, Y. Cai, and R. K. Leane, JCAP **1601**, 051 (2016), arXiv:1512.00476 [hep-ph].

[14] U. Haisch, F. Kahlhoefer, and T. M. P. Tait, Phys. Lett. B **760**, 207 (2016), arXiv:1603.01267 [hep-ph].

[15] A. Alves and K. Sinha, Phys. Rev. D **92**, 115013 (2015), arXiv:1507.08294 [hep-ph].

[16] A. Anandakrishnan, L. M. Carpenter, and S. Raby, Phys. Rev. D **90**, 055004 (2014), arXiv:1407.1833 [hep-ph].

[17] L. M. Carpenter, A. Nelson, C. Shimmin, T. M. P. Tait, and D. Whiteson, Phys. Rev. D **87**, 074005 (2013), arXiv:1212.3352 [hep-ex].

[18] M. Neubert, J. Wang, and C. Zhang, JHEP **1602**, 082 (2016), arXiv:1509.05785 [hep-ph].

[19] F. J. Petriello, S. Quackenbush, and K. M. Zurek, Phys. Rev. D **77**, 115020 (2008), arXiv:0803.4005 [hep-ph].

[20] D. Yang and Q. Li, JHEP **1802**, 090 (2018), arXiv:1711.09845 [hep-ph].

[21] Y. Bai, J. Bourbeau, and T. Lin, JHEP **1506**, 205 (2015), arXiv:1504.01395 [hep-ph].

[22] S. Banerjee, B. Batell, and M. Spannowsky, Phys. Rev. D **95**, 035009 (2017), arXiv:1608.08601 [hep-ph].

[23] L. Carpenter *et al.*, Phys. Rev. D **89**, 075017 (2014), arXiv:1312.2592 [hep-ph].

[24] K. Ghorbani and L. Khalkhali, J. Phys. G **44**, 105044 (2017), arXiv:1608.04559 [hep-ph].

[25] A. A. Petrov and W. Shepherd, Phys. Lett. B **730**, 178 (2014), arXiv:1311.1511 [hep-ph].

[26] G. Bertone, D. Hooper, and J. Silk, Phys. Rept. **405**, 279 (2005), arXiv:hep-ph/0404175.

[27] M. Drees and M. M. Nojiri, Phys. Rev. D **47** (1993), arXiv:hep-ph/9207234.

[28] J. R. Ellis, J. S. Hagelin, D. V. Nanopoulos, K. A. Olive, and M. Srednicki, Nucl. Phys. B **238**, 453 (1984).

[29] H. Goldberg, Phys. Rev. Lett. **50**, 1419 (1983).

[30] G. Jungman, M. Kamionkowski, and K. Griest, Phys. Rept. **267**, 195 (1996), arXiv:hep-ph/9506380.

[31] J. Bramante *et al.*, Phys. Rev. D **91**, 054015 (2015), arXiv:1412.4789 [hep-ph].

[32] J. Bramante *et al.*, Phys. Rev. D **93**, 063525 (2016), arXiv:1510.03460 [hep-ph].

[33] M. Roos, (2010), arXiv:1001.0316 [astro-ph].

[34] K. G. Begeman, A. H. Broeils, and R. H. Sanders, Mon. Not. Roy. Astron. Soc. **249**, 523 (1991).

[35] N. A. Bahcall, Phys. Scripta **T85**, 32 (2000), arXiv:astro-ph/9901076.

[36] R. G. Carlberg *et al.*, The Astrophysical Journal **516**, 552 (1999).

[37] A. Kashlinsky, Physics Reports **307**, 67 (1998), arXiv:astro-ph/9806236.

[38] D. Clowe *et al.*, Astrophys. J. **648**, L109 (2006), arXiv:astro-ph/0608407.

[39] M. Bartelmann, Classical and Quantum Gravity **27**, 233001 (2010), arXiv:1010.3829 [astro-ph.CO].

[40] H. Hoekstra, H. Yee, and M. Gladders, New Astron. Rev. **46**, 767 (2002), arXiv:astro-ph/0205205.

[41] L. V. E. Koopmans and T. Treu, Astrophys. J. **583**, 606 (2003), arXiv:astro-ph/0205281.

[42] R. Massey *et al.*, Nature **445**, 286 (2007), arXiv:0701594 [astro-ph].

[43] M. Bradac *et al.*, Astrophys. J. **687**, 959 (2008), arXiv:0806.2320 [astro-ph].

[44] N. S. Israel and J. W. Moffat, Galaxies **6**, 41 (2018), arXiv:1606.09128 [astro-ph.CO].

[45] W. Hu, N. Sugiyama, and J. Silk, (1995), arXiv:astro-ph/9504057.

[46] W. Hu and S. Dodelson, Ann. Rev. Astron. Astrophys. **40**, 171 (2002), arXiv:astro-ph/0110414.

[47] C. L. Bennett *et al.*, Astrophys. J. **436**, 423 (1994), arXiv:9401012 [astro-ph].

[48] WMAP Collaboration, D. N. Spergel *et al.*, Astrophys. J. Suppl. **148**, 175 (2003), arXiv:0302209 [astro-ph].

[49] Planck Collaboration, P. A. R. Ade *et al.*, Astron. Astrophys. **594**, A13 (2016), arXiv:1502.01589 [astro-ph.CO].

[50] D. Baumann, http://www.damtp.cam.ac.uk/people/d.baumann.

[51] V. Springel, Mon. Not. Roy. Astron. Soc. **364**, 1105 (1005), arXiv:0505010 [astro-ph].

[52] E. W. Kolb and M. S. Turner, Front. Phys. **69**, 1 (1990).

[53] M. Milgrom, Canadian Journal of Physics **93**, 107 (2015).

[54] L. Bernard and L. Blanchet, Phys. Rev. **D91**, 103536 (2015), arXiv:1410.7708 [astro-ph.CO].

[55] Particle Data Group, C. Patrignani *et al.*, Chin. Phys. **C40**, 100001 (2016).

[56] Particle Data Group, M. Tanabashi *et al.*, Phys. Rev. D **98**, 030001 (2018).

[57] S. Weinberg, Phys. Rev. Lett. **40**, 223 (1978).

[58] F. Wilczek, Phys. Rev. Lett. **40**, 279 (1978).

[59] A. Kusenko, Phys. Rept. **481**, 1 (2009), arXiv:0906.2968 [hep-ph].

[60] B. Carr, F. Kuhnel, and M. Sandstad, Phys. Rev. **D94**, 083504 (2016), arXiv:1607.06077 [atro-ph.CO].

[61] T. Plehn, (2017), arXiv:1705.01987 [hep-ph].

[62] G. Arcadi *et al.*, Eur. Phys. J. C **78**, 203 (2018), arXiv:1703.07364 [hep-ph].

[63] L. J. Hall, K. Jedamzik, J. March-Russell, and S. M. West, JHEP **03**, 080 (2010), arXiv:0911.1120 [hep-ph].

[64] K. M. Zurek, Phys. Rept. **537**, 91 (2014), arXiv:1308.0338 [hep-ph].

[65] M. W. Goodman and E. Witten, Phys. Rev. **D31**, 3059 (1985).

[66] T. M. Undagoitia and L. Rauch, J. Phys. G **43**, 013001 (2016), arXiv:1509.08767 [physics.ins-det].

[67] J. Lewin and P. Smith, Astropart. Phys. **6**, 87 (1996).

[68] A. L. Fitzpatrick, W. Haxton, E. Katz, N. Lubbers, and Y. Xu, Journal of Cosmology and Astroparticle Physics **2013**, 004 (2013), arXiv:1203.3542 [hep-ph].

[69] XENON Collaboration, E. Aprile *et al.*, (2018), arXiv:1805.12562 [astro-ph.CO].

[70] PandaX-II Collaboration, X. Cui *et al.*, Phys. Rev. Lett. **119**, 181302 (2017), arXiv:1708.06917 [astro-ph.CO].

[71] LUX Collaboration, D. S. Akerib *et al.*, Phys. Rev. Lett. **118**, 021303 (2017), arXiv:1608.07648 [astro-ph.CO].

[72] PICO Collaboration, C. Amole *et al.*, Phys. Rev. Lett. **118**, 251301 (2017), arXiv:1702.07666 [astro-ph.CO].

[73] E. Aprile and Xenon Collaboration, The XENONnT Dark Matter Experiment, in *APS April Meeting Abstracts*, p. J9.003, 2017.

[74] LUX-ZEPLIN, D. S. Akerib *et al.*, (2018), arXiv:1802.06039 [astro-ph.IM].

[75] DARWIN, J. Aalbers *et al.*, JCAP **1611**, 017 (2016), arXiv:1606.07001 [astro-ph.IM].

[76] M. J. Dolan, F. Kahlhoefer, and C. McCabe, (2017), arXiv:1711.09906 [hep-ph].

[77] Fermi-LAT, M. Ackermann *et al.*, Phys. Rev. Lett. **115**, 231301 (2015), arXiv:1503.02641 [astro-ph].

[78] AMS, M. Aguilar *et al.*, Phys. Rev. Lett. **117**, 091103 (2016).

[79] F. Kahlhoefer, Int. J. Mod. Phys. **A32**, 1730006 (2017), 1702.02430.

[80] ATLAS, M. Aaboud *et al.*, Phys. Rev. **D94**, 032005 (2016), arXiv:1604.07773 [hep-ex].

[81] CMS Collaboration, T. C. Collaboration, CERN Report No. CMS-PAS-EXO-16-037, 2016 (unpublished).

[82] ATLAS, M. Aaboud *et al.*, JHEP **06**, 059 (2016), arXiv:1604.01306 [hep-ex].

[83] CMS Collaboration, T. C. Collaboration, CERN Report No. CMS-PAS-EXO-16-039, 2016 (unpublished).

[84] ATLAS, T. A. collaboration, (2016).

[85] CMS, A. M. Sirunyan *et al.*, JHEP **03**, 061 (2017), arXiv:1701.02042, [Erratum: JHEP09,106(2017)].

[86] ATLAS, T. A. collaboration, (2018).

[87] ATLAS, G. Aad *et al.*, JHEP **09**, 037 (2014), arXiv:1407.7494 [hep-ex].

[88] CMS, V. Khachatryan *et al.*, Phys. Rev. **D91**, 092005 (2015), arXiv:1408.2745 [hep-ex].

[89] F. Giuliani, Phys. Rev. Lett. **95**, 101301 (2005), arXiv:hep-ph/0504157.

[90] N. F. Bell, Y. Cai, J. B. Dent, R. K. Leane, and T. J. Weiler, Phys. Rev. **D92**, 053008 (2015), arXiv:1503.07874 [hep-ph].

[91] T. A. Collaboration, CERN Report No. ATLAS-CONF-2016-011, 2016 (unpublished).

[92] CMS Collaboration, T. C. Collaboration, CERN Report No. CMS-PAS-EXO-16-011, 2016 (unpublished).

[93] ATLAS, M. Aaboud *et al.*, Phys. Rev. Lett. **119**, 181804 (2017), arXiv:1707.01302 [hep-ex].

[94] CMS, C. Collaboration, (2016).

[95] C. Arina *et al.*, JHEP **11**, 111 (2016), arXiv:1605.09242 [hep-ph].

[96] ATLAS, G. Aad *et al.*, Eur. Phys. J. **C75**, 92 (2015), arXiv:1410.4031 [hep-ex].

[97] CMS Collaboration, T. C. Collaboration, CERN Report No. CMS-PAS-EXO-16-005, 2016 (unpublished).

[98] J. Andrea, B. Fuks, and F. Maltoni, Phys. Rev. **D84**, 074025 (2011), 1106.6199.

[99] ATLAS, G. Aad *et al.*, Eur. Phys. J. **C75**, 79 (2015), arXiv:1410.5404 [hep-ex].

[100] CMS Collaboration, T. C. Collaboration, CERN Report No. CMS-PAS-EXO-16-040, 2016 (unpublished).

[101] T. Plehn, J. Thompson, and S. Westhoff, Phys. Rev. **D98**, 015012 (2018), arXiv:1712.08065 [hep-ph].

[102] ATLAS Collaboration, G. Aad *et al.*, JHEP **1511**, 206 (2015), arXiv:1509.00672 [hep-ex].

[103] CMS Collaboration, V. Khachatryan *et al.*, JHEP **1702**, 135 (2017), arXiv:1610.09218 [hep-ex].

[104] T. Corbett *et al.*, JHEP **1508**, 156 (2015), arXiv:1505.05516 [hep-ph].

[105] CMS, V. Khachatryan *et al.*, JHEP **02**, 135 (2017), arXiv:1610.09218 [hep-ex].

[106] D. L. Rainwater and D. Zeppenfeld, JHEP **12**, 005 (1997), arXiv:hep-ph/9712271.

[107] J. Goodman *et al.*, Phys. Rev. D **82**, 116010 (2010), arXiv:1008.1783 [hep-ph].

[108] S. Profumo, W. Shepherd, and T. Tait, Phys. Rev. D **88**, 056018 (2013), arXiv:1307.6277 [hep-ph].

[109] M. Bauer, A. Butter, N. Desai, J. Gonzalez-Fraile, and T. Plehn, Phys. Rev. D **95**, 075036 (2017), arXiv:1611.09908 [hep-ph].

[110] S. Bruggisser, F. Riva, and A. Urbano, JHEP **1611** (2016), arXiv:1607.02475 [hep-ph].

[111] M. Endo and Y. Yamamoto, JHEP **06**, 126 (2014), arXiv:1403.6610 [hep-ph].

[112] J. Abdallah *et al.*, Phys. Dark Univ. **9-10** (2015), arXiv:1506.03116 [hep-ph].

[113] D. Abercrombie *et al.*, arXiv:1507.00966 [hep-ex].

[114] A. Boveia *et al.*, arXiv:1603.04156 [hep-ex].

[115] N. F. Bell, Y. Cai, and R. K. Leane, JCAP **1601**, 051 (2016), arXiv:1512.00476 [hep-ph].

[116] D. Goncalves, P. A. N. Machado, and J. M. No, Phys. Rev. D **95**, 055027 (2017), arXiv:1611.04593 [hep-ph].

[117] M. Bauer, U. Haisch, and F. Kahlhoefer, JHEP **1705**, 138 (2017), arXiv:1701.07427 [hep-ph].

[118] M. R. Buckley, D. Feld, and D. Goncalves, Phys. Rev. D **91**, 015017 (2015), arXiv:1410.6497 [hep-ph].

[119] Y. Cui and F. D'Eramo, Phys. Rev. D **96**, 095006 (2017), arXiv:1705.03897 [hep-ph].

[120] M. Duerr, F. Kahlhoefer, K. Schmidt-Hoberg, T. Schwetz, and S. Vogl, JHEP **1609**, 042 (2016), arXiv:1606.07609 [hep-ph].

[121] J. Ellis, M. Fairbairn, and P. Tunney, JHEP **1708**, 053 (2017), arXiv:1704.03850 [hep-ph].

[122] C. Englert, M. McCullough, and M. Spannowsky, Phys. Dark Univ. **14**, 48 (2016), arXiv:1604.07975 [hep-ph].

[123] P. Harris, V. V. Khoze, M. Spannowsky, and C. Williams, Phys. Rev. D **91**, 055009 (2015), arXiv:1411.0535 [hep-ph].

[124] F. Kahlhoefer, K. Schmidt-Hoberg, T. Schwetz, and S. Vogl, JHEP **1602**, 016 (2016), arXiv:1510.02110 [hep-ph].

[125] F. Kahlhoefer, K. Schmidt-Hoberg, T. Schwetz, and S. Vogl, JHEP **02**, 016 (2016), arXiv:1510.02110 [hep-ph].

[126] E. Bernreuther, J. Horak, T. Plehn, and A. Butter, submitted to SciPost Phys. (2018), arXiv:1805.11637 [hep-ph].

[127] S. R. Coleman and J. Mandula, Phys. Rev. **159**, 1251 (1967).

[128] R. Haag, J. T. Lopuszanski, and M. Sohnius, Nucl. Phys. **B88**, 257 (1975).

[129] S. P. Martin, *A Supersymmetry Primer* (World Scientific, 2011), pp. 1–98, arXiv:9709.356 [hep-ph].

[130] T. Weigand, http://www.thphys.uni-heidelberg.de/ weigand/SUSY-QFT-16-17.html.

[131] U. Ellwanger, C. Hugonie, and A. M. Teixeira, Phys. Rept. **496**, 1 (2010), arXiv:0910.1785 [hep-ph].

[132] A. Butter, *Global Fits for New Physics at the LHC and Beyond*, PhD thesis, Universität Heidelberg, 2017.

[133] T. Cohen and J. G. Wacker, JHEP **1309**, 061 (2013), arXiv:1305.2914 [hep-ph].

[134] A. Butter, S. Murgia, T. Plehn, and T. M. P. Tait, Phys. Rev. D **96**, 035036 (2017), arXiv:1612.07115 [hep-ph].

[135] A. Berlin, D. Hooper, and S. D. McDermott, Phys. Rev. D **89**, 115022 (2014), arXiv:1404.0022 [hep-ph].

[136] Particle Data Group, M. Tanabashi *et al.*, Phys. Rev. D **98**, 030001 (2018).

[137] ALEPH Collaboration, A. Heister *et al.*, Phys. Lett. B **526**, 206 (2002), arXiv:hep-ex/0112011.

[138] ALEPH Collaboration, A. Heister *et al.*, Phys. Lett. B **583**, 247 (2004).

[139] DELPHI Collaboration, J. Abdallah *et al.*, Eur. Phys. J. C **31**, 421 (2003), arXiv:hep-ex/0311019.

[140] L3 Collaboration, P. Achard *et al.*, Phys. Lett. B **580**, 37 (2004), arXiv:hep-ex/0310007.

[141] OPAL Collaboration, G. Abbiendi *et al.*, Eur. Phys. J. C **32** (2004), arXiv:hep-ex/0309014.

[142] ALEPH Collaboration, A. Heister *et al.*, Phys. Lett. B **537**, 5 (2002), arXiv:hep-ex/0204036.

[143] OPAL Collaboration, G. Abbiendi *et al.*, Phys. Lett. B **545**, 272 (2002), arXiv:hep-ex/0209026.

[144] ALEPH Collaboration, A. Heister *et al.*, Phys. Lett. B **533**, 223 (2002), arXiv:hep-ex/0203020.

[145] L3 Collaboration, M. Acciarri *et al.*, Phys. Lett. B **471**, 308 (1999), arXiv:hep-ex/9910020.

[146] K. Griest and D. Seckel, Phys. Rev. D **43**, 3191 (1991).

[147] S. Mizuta and M. Yamaguchi, Phys. Lett. B **298**, 120 (1993), arXiv:hep-ph/9208251.

[148] J. R. Ellis, T. Falk, and K. A. Olive, Phys. Lett. B **444**, 367 (1998), arXiv:hep-ph/9810360.

[149] P. Binetruy, G. Girardi, and P. Salati, Nucl. Phys. B **237**, 285 (1984).

[150] S. Mizuta and M. Yamaguchi, Phys. Lett. B **298**, 120 (1993), arXiv:hep-ph/9208251.

[151] C. Boehm, A. Djouadi, and M. Drees, Phys. Rev. D **62**, 035012 (2000), arXiv:hep-ph/9911496.

[152] P. Huang and C. E. M. Wagner, Phys. Rev. **D90**, 015018 (2014), arXiv:1404.0392 [hep-ph].

[153] A. Butter *et al.*, Phys. Rev. D **93**, 015011 (2016).

[154] R. Lafaye, T. Plehn, M. Rauch, and D. Zerwas, Eur. Phys. J. C **54**, 617 (2008), arXiv:0709.3985 [hep-ph].

[155] C. Adam *et al.*, Eur. Phys. J. C **71**, 1520 (2011), arXiv:1007.2190 [hep-ph].

[156] S. Henrot-Versille *et al.*, Phys. Rev. D **89**, 055017 (2014), arXiv:1309.6958 [hep-ph].

[157] A. Djouadi, J. L. Kneur, and G. Moultaka, Comput. Phys. Commun. **176**, 426 (2007), arXiv:hep-ph/0211331.

[158] G. Brooijmans *et al.*, arXiv:1203.1488 [hep-ph].

[159] A. Djouadi, J. Kalinowski, and M. Spira, Comput. Phys. Commun. **108**, 56 (1998), arXiv:hep-ph/9704448.

[160] M. Mühlleitner, A. Djouadi, and Y. Mambrini, arXiv:hep-ph/0311167.

[161] A. Djouadi, M. M. Mühlleitner, and M. Spira, Acta Phys. Polon. B **38**, 635 (2007), arXiv:hep-ph/0609292.

[162] U. Ellwanger and C. Hugonie, Comput. Phys. Commun. **177**, 399 (2007), arXiv:hep-ph/0612134 [hep-ph].

[163] U. Ellwanger, J. F. Gunion, and C. Hugonie, JHEP **02**, 066 (2005), arXiv:hep-ph/0406215 [hep-ph].

[164] U. Ellwanger and C. Hugonie, Comput. Phys. Commun. **175**, 290 (2006), arXiv:hep-ph/0508022 [hep-ph].

[165] D. Das, U. Ellwanger, and A. M. Teixeira, Comput. Phys. Commun. **183**, 774 (2012), arXiv:1106.5633 [hep-ph].

[166] G. Belanger *et al.*, Comput. Phys. Commun. **182**, 842 (2011), arXiv:1004.1092 [hep-ph].

[167] J. Alwall *et al.*, JHEP **1407**, 079 (2014), arXiv:1405.0301 [hep-ph].

[168] W. Beenakker *et al.*, Phys. Rev. Lett. **83**, 3780 (1999), arXiv:hep-ph/9906298.

[169] H. Sun *et al.*, Phys. Rev. D **73**, 055002 (2006), arXiv:hep-ph/0602089.

[170] J. Debove, B. Fuks, and M. Klasen, Nucl. Phys. B **842**, 51 (2011), arXiv:1005.2909 [hep-ph].

[171] J. Debove, B. Fuks, and M. Klasen, Nucl. Phys. B **849**, 64 (2011), arXiv:1102.4422 [hep-ph].

[172] G. Cullen, N. Greiner, and G. Heinrich, Eur. Phys. J. C **73**, 2388 (2013), arXiv:1212.5154 [hep-ph].

[173] J. Baglio, B. Jäger, and M. Kesenheimer, JHEP **1607**, 083 (2016), arXiv:1605.06509 [hep-ph].

[174] J. Baglio, B. Jäger, and M. Kesenheimer, arXiv:1711.00730 [hep-ph].

[175] A. Freitas, JHEP **1404**, 070 (2014), arXiv:1401.2447 [hep-ph].

[176] N. F. Bell, G. Busoni, and I. W. Sanderson, JCAP **1703**, 015 (2017), arXiv:1612.03475 [hep-ph].

[177] M. Bauer, M. Klassen, and V. Tenorth, arXiv:1712.06597 [hep-ph].

[178] M. S. Carena, J. R. Espinosa, M. Quiros, and C. E. M. Wagner, Phys. Lett. B **335**, 209 (1995), arXiv:hep-ph/9504316.

[179] H. E. Haber, R. Hempfling, and A. H. Hoang, Z. Phys. C **75**, 539 (1997), arXiv:hep-ph/9609331.

[180] S. Heinemeyer, W. Hollik, and G. Weiglein, Eur. Phys. J. C **9**, 343 (1999), arXiv:hep-ph/9812472.

[181] G. Degrassi, S. Heinemeyer, W. Hollik, P. Slavich, and G. Weiglein, Eur. Phys. J. C **28** (2003), arXiv:hep-ph/0212020.

[182] P. Kant, R. V. Harlander, L. Mihaila, and M. Steinhauser, JHEP **1008**, 104 (2010), arXiv:1005.5709 [hep-ph].

[183] E. Bagnaschi *et al.*, JHEP **1406**, 167 (2014), arXiv:1404.0327 [hep-ph].

[184] G. Degrassi, S. D. Vita, and P. Slavich, Eur. Phys. J. C **75**, 61 (2015), arXiv:1410.3432 [hep-ph].

[185] A. Djouadi, M. Drees, P. Fileviez Perez, and M. Muhlleitner, Phys. Rev. **D65**, 075016 (2002), arXiv:hep-ph/0109283 [hep-ph].

[186] R. E. Shrock and M. Suzuki, Phys. Lett. **110B**, 250 (1982).

[187] L. F. Li, Y. Liu, and L. Wolfenstein, Phys. Lett. **159B**, 45 (1985).

[188] K. Griest and H. E. Haber, Phys. Rev. D **37**, 719 (1988).

[189] I. Low, P. Schwaller, G. Shaughnessy, and C. E. M. Wagner, Phys. Rev. D **85**, 015009 (2012), arXiv:1110.4405 [hep-ph].

[190] G. Belanger, B. Dumont, U. Ellwanger, J. F. Gunion, and S. Kraml, Phys. Lett. B **723**, 340 (2013), arXiv:1302.5694 [hep-ph].

[191] M. C. Bento, O. Bertolami, and R. Rosenfeld, Phys. Lett. B **518**, 276 (2001), arXiv:hep-ph/0103340.

[192] R. K. Barman *et al.*, Phys. Rev. D **95**, 095018 (2017), arXiv:1703.03838 [hep-ph].

[193] V. A. Beylin, V. I. Kuksa, R. S. Pasechnik, and G. M. Vereshkov, Eur. Phys. J. C **56**, 395 (2008), arXiv:hep-ph/0702148.

[194] H. Baer, A. Mustafayev, and X. Tata, Phys. Rev. D **90**, 115007 (2014), arXiv:1409.7058 [hep-ph].

[195] A. Biekötter, F. Keilbach, R. Moutafis, T. Plehn, and J. Thompson, SciPost Phys. **4**, 35 (2018), arXiv:1712.03973 [hep-ph].

[196] D. Choudhury and D. P. Roy, Phys. Lett. B **322** (1994), arXiv:hep-ph/9312347.

[197] R. M. Godbole, M. Guchait, K. Mazumdar, S. Moretti, and D. P. Roy, Phys. Lett. B **571**, 184 (2003), arXiv:hep-ph/0304137.

[198] H. Davoudiasl, T. Han, and H. E. Logan, Phys. Rev. D **71**, 115007 (2005), arXiv:hep-ph/0412269.

[199] H. Okawa, J. Kunkle, and E. Lipeles, arXiv:1309.7925 [hep-ex].

[200] D. Goncalves, F. Krauss, S. Kuttimalai, and P. Maierhöfer, Phys. Rev. D **94**, 053014 (2016), arXiv:1605.08039 [hep-ph].

[201] O. J. P. Eboli and D. Zeppenfeld, Phys. Lett. B **495**, 147 (2000), arXiv:hep-ph/0009158.

[202] ATLAS Collaboration, M. Aaboud *et al.*, JHEP **1609**, 175 (2016), arXiv:1608.00872 [hep-ex].

[203] CMS Collaboration, C. Collaboration, CMS-PAS-SUS-17-010 .

[204] M. Blanke, S. Kast, J. Thompson, S. Westhoff, and J. Zurita, in preparation .

[205] CMS, A. M. Sirunyan *et al.*, JHEP **11**, 029 (2017), arXiv:1706.09933 [hep-ex].

[206] M. S. Madhavacheril, N. Sehgal, and T. R. Slatyer, Phys. Rev. **D89**, 103508 (2014), arXiv:1310.3815 [astro-ph.CO].

[207] G. Steigman, Phys. Rev. **D91**, 083538 (2015), arXiv:1502.01884 [astro-ph.CO].

Erklärung:

Ich versichere, dass ich diese Arbeit selbstständig verfasst habe und keine anderen als die angegebenen Quellen und Hilfsmittel benutzt habe.

Heidelberg, den 19. Juli 2018 ....